EXPLORING THE INVISIBLE UNIVERSE BY MODEL BUILDING: NEUTRINOS AND OTHER DARK MATTERS

A Dissertation

by

SUMIT GHOSH

Submitted to the Graduate and Professional School of
Texas A&M University
in partial fulfillment of the requirements for the degree of

DOCTOR OF PHILOSOPHY

Chair of Committee,	Bhaskar Dutta
Committee Members,	Louis E. Strigari
	Stephen A. Fulling
	Teruki Kamon
Head of Department,	Grigory Rogachev

August 2021

Major Subject: Physics

ABSTRACT

The Standard Model (SM) of particle physics is a very successful, mathematically consistent and experimentally proven theory of the known elementary particles. However it is challenged by a variety of theoretical and experimental puzzles. Two well-established theoretical puzzles are the tiny neutrino masses generations and explaining the observed astronomical dark matter content of the Universe. Besides that there are a few anomalous experimental results that cannot be explained by the SM alone. These are the hints that we need some new physics beyond the SM. In this dissertation, we introduce new physics ideas in the form of a model at the MeV to TeV scale, by extending the SM by adding new particles and/or new gauge symmetry and study different puzzles of the SM. Since the new physics scale is below TeV, we can probe the models with the current data coming from various experiments.

DEDICATION

To my mother, my father.

ACKNOWLEDGMENTS

First and foremost, I would like to express my sincere gratitude to my advisor and the chair of the committee, Prof. Bhaskar Dutta for continuous support throughout my Ph.D. studies and research, for his patience, motivation, enthusiasm, and his immense wisdom. His unconditional guidance helped me to complete my research work as a graduate student and to finish the thesis. I could not have imagined having a better advisor for my Ph.D.

I would like to thank the rest of my thesis committee members: Prof. Stephen Fulling, Prof. Teruki Kamon, and Prof Louis Strigari for their encouragement and insightful comments.

Besides my advisor, the other two persons who helped me throughout my Ph.D. studies and research are Prof Tianjun Li and Prof Jason Kumar. I am extremely grateful to them and glad to have them as my mentor and collaborators during my Ph.D. research.

I would like to express my deep and sincere gratitude to all my collaborators: Prof. Ilia Gogoladze, Mohammad Abdullah, Prof. Peisi Huang, Prof. James Dent, Jayden Newstead, Prof Nicole Bell, Prof. Ian Shoemaker, Adrian Thompson, and Ankur Verma for their help.

I am thankful to all of my group mates: Tathagata Ghosh, Esteban Jiminez, Steven Clarke, Shu Liao, Adrian Thompson, and Ankur Verma for their useful discussions about physics and life as a graduate student. Besides all of them, I am highly grateful to the great teachers at the Department of Physics, Texas A&M University: Prof Christopher Pope, Prof Teruki Kamon, Prof Louis Strigari from whom I have learned a lot about my field of research. I would like to express my gratitude to two of my undergraduate teacher: Prof Amitava Raychaudhury and Prof. Anindya Datta, to help to shape my career and for their constant encouragement to pursue Ph.D.

I am grateful to the Mitchell Institute for Fundamental Physics and Astronomy, Department of Physics and Astronomy, Texas A&M University for providing such a great atmosphere for research and learnings, to all the staffs of the department for their immense help throughout the last five years regarding all official needs, specially Raechel E. Superville and Sherree Kessler. The research was supported in part by the DOE Grant No. DE-SC0010813. I would like to thank the

Texas A&M University Office of Graduate and Professional Studies to allow me to use this LaTeX thesis template.

Last but not least, I would like to thank my family and my friends for their love, support, understandings, and carings.

CONTRIBUTORS AND FUNDING SOURCES

Contributors

This work was supported by a dissertation committee consisting of Professor Bhaskar Dutta [advisor], Louis E. Strigari, and Teruki Kamon of the Department of Physics and Astronomy and Professor Stephen A. Fulling of the Department of Mathematics.

The research work conducted for the dissertation was completed by the student working with different collaborations.

Funding Sources

Graduate study was supported in part by the DOE Grant No. DE-SC0010813 and in part by Department of Physics and Astronomy, Texas A&M University, through Teaching Assistantship.

NOMENCLATURE

SM	Standard Model
FCNC	Flavor Changing neutral Current
DM	Dark Matter
BBN	Big Bang Nucleosynthesis
CMB	Cosmic Microwave Background

TABLE OF CONTENTS

Page

LIST OF FIGURES

FIGURE Page

LIST OF TABLES

TABLE Page

1. INTRODUCTION

There is more mass throughout the Universe than what we are capable of seeing. The study of the Gravitational effects such as galaxy rotation curve shows strong evidence of the presence of an unobserved mass in the galaxy [28]. On the other hand, galaxy cluster collisions such as the "bullet cluster" event [29] does not just confirm the presence of an extra mass in the galaxy, but they also show evidence that these invisible masses have almost no interaction with the visible masses. Only five percent of the Universe is visible or luminous mass. Therefore, there must be more matter, which is not visible, causing an additional gravitational effect in the Universe. The immediate question is, how many kinds of invisible matter are there in the Universe and what fraction of the energy budget of the Universe is the invisible matter, what is the nature of these matters, and what is their role in the formation of the galaxy, galaxy clusters and in general the evolution of the Universe. We find that these invisible matters constitute 25% of the Universe with relic abundance $\Omega_{DM} = 0.265$. Traditionally we call them Dark Matter. In this thesis we focus on the origin of these dark matters within a model and how they interact with the visible sector of the Universe, assuming the particle nature of dark matter. Explaining this dark matter content of the Universe is one of the well-established puzzles of Elementary Particle Physics.

While it is clear that, dark matter can not be made up of any known particle from the Standard Model (SM), there is a possible candidate for dark matter that could have the right behavior. At a first glance, the neutrinos of the SM behave just like a viable dark matter candidate with no electromagnetic interactions, they have only weak interactions with visible matter, and they also form cosmic neutrino background after neutrino decoupling at ~ 2.5 MeV. The relic density of massive neutrinos is given by $\Omega_\nu = (\sum_j m_j)/94h^2$ eV, where h is a dimensionless parameter of order one, $h = 0.673 \pm 0.012$. The measurement of the invisible decay width of the Z boson rules out more than three SM neutrinos [30], hence $j = 3$. Therefore 3-4 eV mass per neutrino would give correct dark matter relic density.

Unfortunately, there are problems with having light neutrinos that are that massive. The first

problem is that, if neutrinos are dark matter, they would be hot dark matter. And the hot dark matter would have washed out the matter density perturbation by free streaming, affecting the large-scale structure formation of the Universe. The second problem is with the cosmological data, which put a bound on the sum of the neutrino mass, $\sum_j m_j = 0.12$ eV (BOSS Lyα + Planck [31, 32]). Therefore only 1% dark matter can be in the form of light neutrinos. So what constitutes the other 99% of the invisible Universe is still a mystery. A most promising possibility is the particle dark matter such as sterile neutrinos, weakly interacting massive particles, etc, which comes as a form of a new unknown particle that must satisfy all the current particle physics and cosmological data.

Another interesting unsolved problem of elementary particle physics is the tiny mass of the neutrinos which was confirmed from the observation of neutrino oscillations [33, 34]. SM can not explain this tiny mass. Though the absolute values of the three species of neutrinos have not been measured the mass square differences have been determined by solar and atmospheric neutrino experiments. The global fit of neutrino oscillation data gives [35], $\Delta m^2_{sol} = m_2^2 - m_1^2 \simeq 7.4 \times 10^{-5}$ eV^2 and $\Delta m^2_{atm} = m_3^2 - m_1^2 = 2.5 \times 10^{-3}$ eV^2. Therefore at least two neutrinos have non-zero masses. Assuming the lightest neutrino to be massless, we get $m_{\nu_j} = (0.00, 0.008, 0.05)$ eV. They are consistent with the cosmological data [32]. We need new physics ideas to explain these tiny neutrino masses and mixings.

The main goal of this thesis would be to address the two most important shortcomings of the SM: the origin of the neutrino mass and mixings and explaining the observed dark matter content of the Universe. The central theme of the thesis is to construct models at the MeV to TeV scale, by extending the SM by adding new particles and/or new gauge symmetry in a bottom-up approach and understand the puzzles of the SM. We also test the new physics models using the currently available data and future projections from the upcoming experiments. We have used these models to explain the recently found/confirmed anomalous experimental signals and predicted new signals for the current/upcoming experiments.

This thesis is written based on the following published and unpublished research articles, organized in a chronological order,

1. B. Dutta, S. Ghosh, I. Gogoladze and T. Li, " **Three-loop neutrino masses via new massive gauge bosons from E_6 GUT**", Phys. Rev. D **98**, no. 5, 055028 (2018), arXiv:1805.01866 [hep-ph].

2. B. Dutta, S. Ghosh and J. Kumar, "**A sub-GeV dark matter model**", Phys. Rev. D **100**, 075028 (2019), arXiv:1905.02692 [hep-ph].

3. M. Abdullah, B. Dutta, S. Ghosh and T. Li, "$(g-2)_{\mu,e}$ **and the ANITA anomalous events in a three-loop neutrino mass model**", Phys. Rev. D **100**, no. 11, 115006 (2019), arXiv:1907.08109 [hep-ph].

4. B. Dutta, S. Ghosh and J. Kumar, "**Contributions to ΔN_{eff} from the dark photon of $U(1)_{T3R}$**", Phys. Rev. D **102** (2020) 1, 015013, arXiv:2002.01137 [hep-ph].

5. B. Dutta, S. Ghosh and T. Li, "**Explaining $(g-2)_{\mu,e}$, KOTO anomaly and MiniBooNE excess in an extended Higgs model with sterile neutrinos**", Phys. Rev. D **102** (2020) 5, 055017, arXiv:2006.01319 [hep-ph]

6. B. Dutta, S. Ghosh and J. Kumar, "**Opportunities for probing $U(1)_{T3R}$ with light mediators**", Phys. Rev. D **102** (2020) 7, 075041, arXiv:2007.16191.

7. B. Dutta, S. Ghosh, P. Huang and J. Kumar, "**Explaining $g_\mu - 2$ and $R_{K^{(*)}}$ using the light mediators of $U(1)_{T3R}$**", arXiv:2105.07655.

The thesis is divided into three main chapters. In each chapter, we introduce a new physics model by extending the SM and describe the related phenomenology. In Chapter. 2, we introduce a low energy model, which is a complete model of neutrino mass and mixings and dark matter.

It involves a light scalar mediator which can explain a few of the recent anomalies. This chapter is based on article No. 5 from the above list. In Chapter. 3, we introduce a sub-GeV dark matter model, allowed by current data, which can deplete correct relic density and has interesting direct detection prospects. This chapter is based on articles No. 2, 4, 6, and 7. In the last chapter, Chapter. 4, We describe a three-loop radiative neutrino mass model, accessible at the LHC, which is based on the article No. 1 and 3.

2. EXPLAINING $(g-2)\mu, e$, THE KOTO ANOMALY AND THE MINIBOONE EXCESS IN AN EXTENDED HIGGS MODEL WITH STERILE NEUTRINOS*

The SM of particle physics is far from being a complete model, since it can not explain the origin of tiny masses of neutrinos, their mixing [33, 34], and the observed abundance of dark matter particles [32]. Besides the neutrino mass and dark matter problem, there are a few more recent anomalous experimental results such as the muon and electron anomalous magnetic moment [36, 37, 38, 39], anomalous events at the KOTO experiment [40, 41, 42], and the observation of excess electron-like events at MiniBooNE experiments [43, 44]. They are the indications that we need new physics beyond SM to correctly describe the nature. In this chapter, we want to build a complete model for neutrino mass and mixing with correct dark matter relic density that can explain the above-mentioned experimental anomalies. We build the model by extending the SM by adding three right-handed neutrinos and extending the scalar sector by adding one additional scalar doublet and one scalar singlet. We produce a phenomenologically interesting physical scalar spectrum with one short-lived, light scalar with mass ~ 100 MeV, which plays an important role to connect the anomalies. Correct neutrino masses and mixing can be generated using a low-scale type-I seesaw mechanism. The lightest physical sterile neutrino with mass $\sim \mathcal{O}(10)$ keV, is a viable dark matter candidate that can produce the correct relic abundance. We have shown that the tree-level flavor changing interactions of the light scalar together with the sterile neutrinos can explain all three anomalies simultaneously, satisfying related constraints from the current experimental data.

The rest of the chapter is organized as follows: In Sec. 2.1 we discuss the details of the model by introducing necessary parameters and interaction terms. The origin of neutrino mass and mixing is presented in Sec. 2.2. In Sec. 2.3, we discuss the possibility of the lightest sterile neutrino as a viable dark matter candidate in our model. We generate a phenomenologically interesting physical scalar spectrum in Sec. 2.4. In Sec. 2.5, we study the anomalous magnetic moments

*this chapter is reprinted from **"Explaining $(g-2)_{\mu,e}$, KOTO anomaly and MiniBooNE excess in an extended Higgs model with sterile neutrinos"** by B. Dutta, S. Ghosh and T. Li, Phys. Rev. D **102** (2020) 5, 055017 published by the American Physical Society under the terms of the Creative Commons Attribution 4.0 International license.

of the electron and muon and allowed parameter space related to this. In Sec. 2.6, we discuss the allowed parameter space associated with the KOTO anomaly and the relevant constraints. In Sec. 2.7, we discuss the recent MiniBooNE observation and how to accommodate it in our model. We summarize our analysis in Sec. 2.8 by showing a few benchmark points (BP) which explain all the anomalies after satisfying all other experimental data. We provide additional information in the Appendix. A and Appendix. B.

2.1 Model

The SM has the simplest possible scalar sector with just one scalar doublet [45, 46, 47, 48, 49]. Two-Higgs-doublet model (2HDM) [50, 51] and singlet/triplet extensions of 2HDM are good example of the extension of the SM scalar sector backed by strong motivations [52, 53, 54, 55, 56, 57, 58, 59, 60, 61, 62, 63, 64, 65, 66, 67]. In this chapter, we consider a simple extension of the CP-conserving 2HDM by adding one complex scalar singlet. In addition to the extended scalar sector, we add three right-handed sterile neutrinos n'_{R_i} with $i = 1, 2, 3$ to explain the observed neutrino masses and mixing. The definition of the electric charge is same as the SM i.e. $Q \equiv T_3 + Y$. The electroweak charges of the scalars are,

$$\phi_1 \sim (2, 1/2), \quad \phi_2 \sim (2, 1/2), \quad \phi_S \sim (1, 0)\ , \tag{2.1}$$

For the purpose of our study, we assume that the scalar sector respect the CP symmetry but in general it can be CP-violating. Note that, we do not impose any discrete symmetry to the scalar

sector. The most general renormalizable and CP-conserving scalar potential can be written as,

$$
\begin{aligned}
V &= m_1^2\phi_1^\dagger\phi_1 + m_2^2\phi_2^\dagger\phi_2 + m_{12}^2(\phi_1^\dagger\phi_2 + \phi_2^\dagger\phi_1) + m_S^2\phi_S^\dagger\phi_S - m_{S'}^2(\phi_S^2 + \phi_S^{\dagger 2}) \\
&+ m_{1S}(\phi_1^\dagger\phi_1\phi_S + \phi_1^\dagger\phi_1\phi_S^\dagger) + m_{2S}(\phi_2^\dagger\phi_2\phi_S + \phi_2^\dagger\phi_2\phi_S^\dagger) + \frac{\lambda_1}{2}(\phi_1^\dagger\phi_1)^2 + \frac{\lambda_2}{2}(\phi_2^\dagger\phi_2)^2 \\
&+ \frac{\lambda_S}{2}(\phi_S^\dagger\phi_S)^2 + \lambda_3(\phi_1^\dagger\phi_1)(\phi_2^\dagger\phi_2) + \lambda_4(\phi_1^\dagger\phi_2)(\phi_2^\dagger\phi_1) + \lambda_5\left[(\phi_1^\dagger\phi_2)^2 + (\phi_2^\dagger\phi_1)^2\right] \\
&+ \lambda_6\left[(\phi_1^\dagger\phi_1)(\phi_1^\dagger\phi_2) + (\phi_1^\dagger\phi_1)(\phi_2^\dagger\phi_1)\right] + \lambda_7\left[(\phi_2^\dagger\phi_2)(\phi_1^\dagger\phi_2) + (\phi_2^\dagger\phi_2)(\phi_2^\dagger\phi_1)\right] \\
&+ \lambda_{1S}(\phi_1^\dagger\phi_1)(\phi_S^\dagger\phi_S) + \lambda_{2S}(\phi_2^\dagger\phi_2)(\phi_S^\dagger\phi_S) + \lambda_{12S}\left[(\phi_1^\dagger\phi_2)(\phi_S^\dagger\phi_S) + (\phi_2^\dagger\phi_1)(\phi_S^\dagger\phi_S)\right] \\
&+ m_{12S}(\phi_1^\dagger\phi_2\phi_S + \phi_S^\dagger\phi_2^\dagger\phi_1)\ . \qquad (2.2)
\end{aligned}
$$

We work in a basis, similar to the so called Higgs basis [68, 69, 70, 71, 72], where only one of the doublet will obtain vev, $\langle\phi_1\rangle = v/\sqrt{2}$. The ralated basis tranformation rules are defined in Appendix. A. Therefore the doublet ϕ_1 completely controls the spontaneous breaking of the electroweak gauge symmetry and the mass generations of the fermions and gauge bosons. While the other doublet and the singlet play role in the Yukawa interactions. After the spontaneous symmetry breaking, the scalar fields can be written as,

$$
\begin{aligned}
\phi_1 &\sim \begin{pmatrix} G^+ \\ \frac{1}{\sqrt{2}}(v + \rho_1 + iG_0) \end{pmatrix}, \phi_2 \sim \begin{pmatrix} {\phi_2}^+ \\ \frac{1}{\sqrt{2}}(\rho_2 + i\eta_2) \end{pmatrix}, \\
\phi_S &\sim \frac{1}{\sqrt{2}}(\rho_S + i\eta_S)\ . \qquad (2.3)
\end{aligned}
$$

We get the following conditions from the extremization of Eq. 4.3,

$$
\begin{aligned}
m_1^2 + \frac{\lambda_1 v^2}{2} &= 0\ , \qquad (2.4) \\
m_{12}^2 + \frac{\lambda_6 v^2}{2} &= 0\ . \qquad (2.5)
\end{aligned}
$$

Eq. 2.5 implies that the field ϕ_2 does not obtain vev. We get further conditions from the minimiza-

tions,

$$\begin{aligned} \lambda_1 \quad &> 0, \quad m_1^2 < 0, \quad \lambda_5 > 0, \quad \lambda_6 > 0, \\ m_{12}^2 \quad &< 0, \quad m_{12S} > 0, \quad m_{1S} = 0 \, . \end{aligned} \tag{2.6}$$

The last condition makes sure that ϕ_S does not get vev.

Therefore there are altogether 17 free parameters in the scalar sector including the vev v. The total number of scalar degrees of freedom is 10. Three of them get eaten to give mass to the gauge bosons, $W^\pm$ and Z while the other 7 dof correspond to physical Higgs.$G^\pm$ and G_0 become the Goldstone bosons in the Higgs basis. $\phi_2^\pm$ gives two charged physical Higgs $h^\pm$. CP-even states ρ_1, ρ_2 and ρ_S mix to give three neutral physical scalars h, h_1 and h_2. We denote the SM Higgs boson as h. The CP-odd states η_2 and η_S mix and gives two neutral physical pseudoscalar s_1 and s_2.

Analyzing the scalar potential, we find that the physical charged scalar mass squared is given as,

$$m_{h^\pm}^2 = m_2^2 + \frac{\lambda_3 v^2}{2} \, . \tag{2.7}$$

The three CP-even neutral scalars ρ_1, ρ_2 and ρ_S mix in the following way,

$$V_{mass}^{\rho} = \frac{1}{2} \begin{pmatrix} \rho_1 & \rho_2 & \rho_S \end{pmatrix} \left(M_\rho^2\right)_{3\times 3} \begin{pmatrix} \rho_1 \\ \rho_2 \\ \rho_S \end{pmatrix} \, , \tag{2.8}$$

where the 3×3 mass square matrix M_ρ^2 is defined as,

$$M_\rho^2 = \begin{pmatrix} \lambda_1 v^2 & \lambda_6 v^2 & 0 \\ \lambda_6 v^2 & m_2^2 + \frac{\lambda_{345}^+ v^2}{2} & \frac{m_{12S} v}{\sqrt{2}} \\ 0 & \frac{m_{12S} v}{\sqrt{2}} & m_S^2 - 2m_{S'}^2 + \frac{\lambda_8 v^2}{2} \end{pmatrix} \, . \tag{2.9}$$

we have used Eq. 2.5 to simplify terms in the above mass squared matrix and defined $\lambda_{345}^+ \equiv$

$\lambda_3+\lambda_4+\lambda_5$. We get three physical scalars from the above mixing, h, h_1 and h_2 with mass squared $m_h^2, m_{h_1}^2$ and $m_{h_2}^2$, respectively. The fields in the mass basis, h, h_1 and h_2 are related to those in the interaction basis, ρ_1, ρ_2 and ρ_S through a 3×3 rotation matrix $U_{R3\times 3}(\theta_i)$. U_R can be parametrized with three Euler angles θ_1, θ_2 and θ_3 in the following way,

$$U_R \;=\; \begin{pmatrix} c_{11} & c_{12} & c_{13} \\ c_{21} & c_{22} & c_{23} \\ c_{31} & c_{32} & c_{33} \end{pmatrix} , \tag{2.10}$$

where $\rho_i = U_{Rij}h_j$. The quantities c_{ij} are functions of $\cos\theta_k$ and $\sin\theta_k$ ($k = 1,2,3$). The interaction states can be expressed in terms of the physical states as

$$\begin{aligned} \rho_1 &= c_{11}h_2 + c_{12}h + c_{13}h_1 \,, \\ \rho_2 &= c_{21}h_2 + c_{22}h + c_{23}h_1 \,, \\ \rho_S &= c_{31}h_2 + c_{32}h + c_{33}h_1 \,. \end{aligned} \tag{2.11}$$

The two CP-odd neutral scalars η_2-η_S mix as

$$V^{\eta}_{mass} = \frac{1}{2}\begin{pmatrix}\eta_2 & \eta_S\end{pmatrix}\left(M^2_\eta\right)_{2\times 2}\begin{pmatrix}\eta_2 \\ \eta_S\end{pmatrix} , \tag{2.12}$$

where the 2×2 mass square matrix M^2_η is given by

$$M^2_\eta = \begin{pmatrix} m_2^2 + \frac{\lambda^-_{345}v^2}{2} & -\frac{m_{12S}v}{\sqrt{2}} \\ -\frac{m_{12S}v}{\sqrt{2}} & m_S^2 + 2m_{S'}^2 + \frac{\lambda_8 v^2}{2} \end{pmatrix} , \tag{2.13}$$

where we have defined $\lambda^-_{345} \equiv \lambda_3+\lambda_4-\lambda_5$. From the above mixing, we get two physical neutral

pseudoscalar which can be expressed in terms of the interaction states as,

$$\begin{pmatrix} s_1 \\ s_2 \end{pmatrix} = \begin{pmatrix} \cos\alpha & -\sin\alpha \\ \sin\alpha & \cos\alpha \end{pmatrix} \begin{pmatrix} \eta_2 \\ \eta_S \end{pmatrix} , \tag{2.14}$$

where the mixing angle is given by

$$\tan 2\alpha = \frac{m_{12S} v/\sqrt{2}}{m_{11}^2 - m_{22}^2} \tag{2.15}$$

The corresponding mass squared are given as,

$$m_{s_1}^2 = \frac{1}{2}(m_{11}^2 + m_{22}^2) - \frac{1}{2}\sqrt{(m_{11}^2 - m_{22}^2)^2 + \frac{m_{12S}^2 v^2}{2}} \tag{2.16}$$

and

$$m_{s_2}^2 = \frac{1}{2}(m_{11}^2 + m_{22}^2) + \frac{1}{2}\sqrt{(m_{11}^2 - m_{22}^2)^2 + \frac{m_{12S}^2 v^2}{2}} , \tag{2.17}$$

respectively, where

$$m_{11}^2 = \frac{1}{2}\left(m_2^2 + \frac{\lambda_3 v^2}{2} + \frac{\lambda_4 v^2}{2} - \frac{\lambda_5 v^2}{2}\right) \tag{2.18}$$

and

$$m_{22}^2 = \frac{1}{2}\left(m_S^2 + 2m_{S'}^2 + \frac{\lambda_8 v^2}{2}\right) . \tag{2.19}$$

The Yukawa sector of our model is very interesting in the Higgs basis. Both scalar doublets interact with all the fermions in the interaction states. On the otherhand, the saclar singlet only interacts with the right handed neutrinos. The doublet ϕ_1 controls the masses of the fermions while the other doublet ϕ_2 couples to the fermions in an unconstrained way and do not need to obey the flavor symmetry. Therefore the neutral component of ϕ_2 interacting with the fermions can gives rise to tree-level flavor-changing neutral current (FCNC). The mixing in the scalar sector ensures that the singlet scalar can interact with the fermions in the mass basis. We start with the

complete Yukawa sector Lagrangian in the interaction basis,

$$\begin{aligned}
-\mathcal{L} \;=\; & \bar{q}'_{L_i}(y'_{1d})_{ij}d'_{R_j}\phi_1 + \bar{q}'_{L_i}(y'_{1u})_{ij}u'_{R_j}\tilde{\phi}_1 + \bar{l}'_{L_i}(y'_{1e})_{ij}e'_{R_j}\phi_1 + \bar{l}'_{L_i}(y'_{1n})_{ij}n'_{R_j}\tilde{\phi}_1 \\
& + \bar{q}'_{L_i}(y'_{2d})_{ij}d'_{R_j}\phi_2 + \bar{q}'_{L_i}(y'_{2u})_{ij}u'_{R_j}\tilde{\phi}_2 + \bar{l}'_{L_i}(y'_{2e})_{ij}e'_{R_j}\phi_2 + \bar{l}'_{L_i}(y'_{2n})_{ij}n'_{R_j}\tilde{\phi}_2 \\
& + \bar{n}'^{c}_{R_i}(y'_{sn})_{ij}n'_{R_j}\phi_S + \frac{1}{2}\bar{n}'^{c}_{R_i}M'_{ij}n'_{R_j} + H.c.\,, \qquad (2.20)
\end{aligned}$$

where $i, j = 1, 2, 3$ are the family indices. The fermions in the interaction basis are denoted by the primed fermions. Note that, in general all the Yukawa matrices defined are 3×3 complex matrices.

In general, the 3×3 Yukawa matrices, y'_{ij} and the Majorana mass matrix M'_{ij} can be diagonalized using biunitary transformations as follows,

$$U^{\dagger}_{d_L}y'_{1d}U_{d_R} = y_{1d}, \quad \text{where} \quad (y_{1d})_{ij} = (y_{1d})_{ii}\delta_{ij}\,, \qquad (2.21)$$

$$U^{\dagger}_{u_L}y'_{1u}U_{u_R} = y_{1u}, \quad \text{where} \quad (y_{1u})_{ij} = (y_{1u})_{ii}\delta_{ij}\,, \qquad (2.22)$$

$$U^{\dagger}_{e_L}y'_{1e}U_{e_R} = y_{1e}, \quad \text{where} \quad (y_{1e})_{ij} = (y_{1e})_{ii}\delta_{ij}\,, \qquad (2.23)$$

$$U^{\dagger}_{\nu_L}y'_{1n}U_{n_R} = y_{1n}, \quad \text{where} \quad (y_{1n})_{ij} = (y_{1n})_{ii}\delta_{ij}\,, \qquad (2.24)$$

$$U^{\dagger}_{n_R}M'U_{n_R} = M, \quad \text{where} \quad M_{ij} = M_{ii}\delta_{ij}\,, \qquad (2.25)$$

where U_{d_L}, U_{d_R}, U_{u_L}, U_{u_R}, U_{e_L}, U_{e_R}, U_{ν_L} and U_{n_R} are eight appropriate 3×3 unitary matrices which can be used to define the physical states of the fermions in the following way,

$$d_{L_i} = (U^{\dagger}_{d_L})_{ij}d'_{L_j}, \qquad d_{R_i} = (U^{\dagger}_{d_R})_{ij}d'_{R_j}\,, \qquad (2.26)$$

$$u_{L_i} = (U^{\dagger}_{u_L})_{ij}u'_{L_j}, \qquad u_{R_i} = (U^{\dagger}_{u_R})_{ij}u'_{R_j}\,, \qquad (2.27)$$

$$e_{L_i} = (U^{\dagger}_{e_L})_{ij}e'_{L_j}, \qquad e_{R_i} = (U^{\dagger}_{e_R})_{ij}e'_{R_j}\,, \qquad (2.28)$$

$$\nu_{L_i} = (U^{\dagger}_{\nu_L})_{ij}\nu'_{L_j}, \qquad n_{R_i} = (U^{\dagger}_{n_R})_{ij}n'_{R_j}\,. \qquad (2.29)$$

In addition to the above eight matrces we also define the following matrices,

$$
\begin{aligned}
(y_{2d})_{ij} &= (U^{\dagger}_{d_L})_{ik}(y'_{2d})_{kl}(U_{d_R})_{lj} \ , && (2.30)\\
(y_{2u})_{ij} &= (U^{\dagger}_{u_L})_{ik}(y'_{2u})_{kl}(U_{u_R})_{lj} \ , && (2.31)\\
(y_{2e})_{ij} &= (U^{\dagger}_{e_L})_{ik}(y'_{2e})_{kl}(U_{e_R})_{lj} \ , && (2.32)\\
(y_{2n})_{ij} &= (U^{\dagger}_{\nu_L})_{ik}(y'_{2n})_{kl}(U_{n_R})_{lj} \ , && (2.33)\\
(y_{sn})_{ij} &= (U^{\dagger}_{n_R})_{ik}(y'_{sn})_{kl}(U_{n_R})_{lj} \ . && (2.34)
\end{aligned}
$$

Using the relations defined in Eq. 2.21-2.34 and the definition of the physical scalar states, the Yukawa sector Lagrangian can be rewritten as follows

$$
\begin{aligned}
-\mathcal{L} &= (m_f)_i \bar{f}_i f_i + (m_{\nu_d})_i(\bar{\nu}_{L_i} n_{R_i} + \bar{n}_{R_i}\nu_{L_i}) + \frac{1}{2} M_i(\bar{n}^c_{R_i} n_{R_i} + \bar{n}_{R_i} n^c_{R_i}) \\
&+ \bar{\nu}_{L_i}(U^{\dagger}_{PMNS})_{ik}(y_{2e})_{kj} e_{R_j} h^+ + \bar{e}_{R_i}(y_{2e})_{ik}(U_{PMNS})_{kj}\nu_{L_j} h^- \\
&- \bar{e}_{L_i}(U_{PMNS})_{ik}(y_{2n})_{kj} n_{R_j} h^- - \bar{n}_{R_i}(y_{2n})_{ik}(U^{\dagger}_{PMNS})_{kj} e_{L_j} h^+ \\
&+ \bar{u}_i[(U_{CKM})_{ik}(y_{2d})_{kj} P_R - (y_{2u})_{ik}(U_{CKM})_{kj} P_L] d_j h^+ \\
&+ \bar{d}_i[(y_{2d})_{ik}(U^{\dagger}_{CKM})_{kj} P_L - (U^{\dagger}_{CKM})_{ik}(y_{2u})_{kj} P_R] u_j h^- \\
&+ \bar{f}_i (y_{f\phi})_{ij} f_j \phi + (y_{n\phi})_{ij}(\bar{\nu}_{L_i} n_{R_j} + \bar{n}_{R_i}\nu_{L_j})\phi \\
&+ (y_{nn\phi})_{ij}(\bar{n}^c_{R_i} n_{R_j} + \bar{n}_{R_i} n^c_{R_j})\phi \ , \qquad (2.35)
\end{aligned}
$$

where we have used the compact notation: $f = d, u, e$; $\phi = h, h_1, h_2, s_1, s_2$ and $(m_f)_i = (y_{1f})_i v/\sqrt{2}$. The Dirac mass matrix of neutrinos is defined as $(m_{\nu_d})_i = (y_{1n})_{ii} v/\sqrt{2}$ while the Majorana mass matrix is $M_i = M_{ii}\delta_{ij}$. The definitions of the Cabibbo-Kobayashi-Maskawa (CKM) and Pontecorvo-Maki-Nakagawa-Sakata (PMNS) matrices are given by

$$
\begin{aligned}
U_{CKM} &= U^{\dagger}_{u_L} U_{d_L} \ , && (2.36)\\
U_{PMNS} &= U^{\dagger}_{e_L} U_{\nu_L} \ . && (2.37)
\end{aligned}
$$

respectively.

The scalar-charged fermion couplings $y_{f\phi}$ are defined as

$$\begin{aligned}
(y_{fh_2})_{ij} &= \frac{(m_f)_i}{v} c_{11}\delta_{ij} + \frac{(y_{2f})_{ij}}{\sqrt{2}} c_{21} \ , \\
(y_{fh})_{ij} &= \frac{(m_f)_i}{v} c_{12}\delta_{ij} + \frac{(y_{2f})_{ij}}{\sqrt{2}} c_{22} \ , \\
(y_{fh_1})_{ij} &= \frac{(m_f)_i}{v} c_{13}\delta_{ij} + \frac{(y_{2f})_{ij}}{\sqrt{2}} c_{23} \ , \\
(y_{fs_1})_{ij} &= i\frac{(y_{2f})_{ij}}{\sqrt{2}} \cos\alpha \ , \\
(y_{fs_2})_{ij} &= i\frac{(y_{2f})_{ij}}{\sqrt{2}} \sin\alpha \ .
\end{aligned} \tag{2.38}$$

The couplings of active-sterile neutrino states with the scalars, $y_{n\phi}$ are defined as

$$\begin{aligned}
(y_{nh_2})_{ij} &= \frac{(m_{\nu_D})_i}{v} c_{11}\delta_{ij} + \frac{(y_{2n})_{ij}}{\sqrt{2}} c_{21} \ , \\
(y_{nh})_{ij} &= \frac{(m_{\nu_D})_i}{v} c_{12}\delta_{ij} + \frac{(y_{2n})_{ij}}{\sqrt{2}} c_{22} \ , \\
(y_{nh_1})_{ij} &= \frac{(m_{\nu_D})_i}{v} c_{13}\delta_{ij} + \frac{(y_{2n})_{ij}}{\sqrt{2}} c_{23} \ , \\
(y_{ns_1})_{ij} &= i\frac{(y_{2n})_{ij}}{\sqrt{2}} \cos\alpha \ , \\
(y_{ns_2})_{ij} &= i\frac{(y_{2n})_{ij}}{\sqrt{2}} \sin\alpha \ .
\end{aligned} \tag{2.39}$$

And the couplings between two sterile neutrinos and the scalars, $y_{nn\phi}$ are defined as

$$\begin{aligned}
(y_{nnh_2})_{ij} &= \frac{(y_{sn})_{ij}}{\sqrt{2}} c_{31} \ , \\
(y_{nnh})_{ij} &= \frac{(y_{sn})_{ij}}{\sqrt{2}} c_{32} \ , \\
(y_{nnh_1})_{ij} &= \frac{(y_{sn})_{ij}}{\sqrt{2}} c_{33} \ , \\
(y_{nns_1})_{ij} &= -i\frac{(y_{sn})_{ij}}{\sqrt{2}} \sin\alpha \ , \\
(y_{nns_2})_{ij} &= i\frac{(y_{sn})_{ij}}{\sqrt{2}} \cos\alpha \ .
\end{aligned} \tag{2.40}$$

The above discussions show the general framework of the model without assuming any particular parameter space in mind. In the next three sections we will develop a particular phenomenologically interesting parameter space which satisfy all the current constraints.

2.2 Neutrino Masses and Mixings

This section describe the mixing of active and sterile neutrino states and the generation of tiny neutrino masses consistent with the global analysis of neutrino data. The three right handed neutrino states generically mix with the three SM left handed neutrino states and give rise to six physical neutrino eigenstates. We rely on the type-I see-saw mechanism [73, 74, 75, 76] to produce the light mass states, where they get suppressed by the scale of the heavy right handed states. The masses of the neutrinos can be obtained from the following Lagrangian,

$$\begin{aligned} -\mathcal{L}_{\text{neutrino}} &= (m_{\nu_d})_i(\bar{\nu}_{L_i} n_{R_i} + \bar{n}_{R_i}\nu_{L_i}) + \frac{1}{2}M_i(\bar{n}^c_{R_i} n_{R_i} + \bar{n}_{R_i} n^c_{R_i}) \\ &= \frac{1}{2}\left(\bar{\nu}^C_{L_i}\ \bar{\eta}_{R_i}\right)\begin{pmatrix} 0 & (m^T_{\nu_d})_i \\ (m_{\nu_d})_i & M_i \end{pmatrix}\begin{pmatrix} \nu_{L_i} \\ n^C_{R_i} \end{pmatrix} + \text{H.c.}\,. \end{aligned} \tag{2.41}$$

We define the 6×6 Dirac-Majorana mass matrix of neutrinos as,

$$M_i^{D+M} = \begin{pmatrix} 0 & (m^T_{\nu_d})_i \\ \\ (m_{\nu_d})_i & M_i \end{pmatrix}\,. \tag{2.42}$$

The mass matrix, M_i^{D+M} can be diagonalized by blocks [77, 78], up to corrections at the order of $M_i^{-1}(m_{\nu_d})_i$, under the assumption that all the eigenvalues of M_i are much larger than the eigen-

values of $(m_{\nu_d})_i$ as follows,

$$\mathcal{W}^T M_i^{D+M} \mathcal{W} \simeq \begin{pmatrix} (M_{\text{light}})_i & 0 \\ 0 & (M_{\text{heavy}})_i \end{pmatrix} , \tag{2.43}$$

where the 6×6 diagonalizing matrix $\mathcal{W}$ is given by

$$\mathcal{W} \simeq \begin{pmatrix} 1 - \frac{1}{2} R R^\dagger & R^\dagger \\ -R & 1 - \frac{1}{2} R^\dagger R \end{pmatrix} \tag{2.44}$$

with $R = M_i^{-1}(m_{\nu_d})_i$. The 3×3 light and heavy neutrino mass matrices produced in the process are given by

$$m_{\nu_i} = (M_{\text{light}})_i = -(m_{\nu_d}^T)_i M_i^{-1} (m_{\nu_d})_i , \tag{2.45}$$

$$m_{n_i} = (M_{\text{heavy}})_i = M_i . \tag{2.46}$$

respectively.

The physical states v_i and n_i are the light active and heavy sterile neutrinos respectively. A more detail treatment of low scale type-I seesaw can be found in Ref. [79]. The absolute masses of the light active states are not known from the oscillation data as the neutrino oscillation is only sensitive to the mass squared differences, $m_{\nu_i}^2 - m_{\nu_j}^2$. The mass squared differences depend on the hierarchical order of the light neutrino masses. For our study, we consider the normal hierarchy scenario, where $m_{\nu_1} \ll m_{\nu_2} < m_{\nu_3}$. In this scenario, the two mass squared differences are $\Delta m_{21}^2 = (7.05 - 8.24) \times 10^{-5}$ eV^2 and $\Delta m_{31}^2 = (2.334 - 2.524) \times 10^{-3}$ eV^2 based on the global analysis of the oscillation data [35]. It is easy to see that, there are at least two non-zero eigenstates. Assuming the lightest neutrino to be massless, we get $m_{\nu_i} \simeq (0, 8.66 \times 10^{-3}, 0.05)$ eV. The mixing

angle between the active-sterile states can be parametrized as $\theta_{ij} = M_i^{-1}(m_{\nu_d})_i(U_{nR}^{\dagger})_{ij}$. We also define $\theta^2 \equiv \sum_{ij} |\theta_{ij}|^2$. We consider two interesting benchmark scenarios that can generate tiny neutrino masses estimated above along with $m_{n_{2,3}} \sim \mathcal{O}(100)$ MeV range, and $m_{n_1} \sim \mathcal{O}(10)$ keV. We also estimate the mixing parameter.

BP	M_i (MeV)	$(m_{\nu_d})_i$ (GeV)	θ^2
BP1	$(0.002, 420, 10)$	$(0, 1.9 \times 10^{-6}, 1.58 \times 10^{-4})$	6×10^{-9}
BP2	$(0.007, 380, 640)$	$(0, 1.81 \times 10^{-6}, 5.62 \times 10^{-6})$	10^{-11}

Table 2.1: We consider two different benchmark scenarios which can generate 3 light and 3 heavy neutrino states in the normal hierarchy case.

2.3 Dark Matter

In Sec. 2.2, we found that the lightest of the three sterile neutrino state, n_1 can get mass $m_{n_1} \simeq \mathcal{O}(1-10)$ keV. These particles can be the dark matter candidates in our model under certain conditions. Let us investigate the scenario where this can be a viable dark matter candidates. These $\mathcal{O}(1-10)$ keV particles can be produced in the early Universe at high temperature but they can never be in thermal equilibrium due to their very weak interactions with the SM particles. Though the interaction strength is weak, these neutral particles can decay to the lighter SM particles as the decay is not protected by any symmetry. But they can have lifetime longer than the age of the Universe, which is controlled by the active-sterile mixing parameter defined in Sec. 2.2. On the otherhand, the decay of the sterile neutrinos can put bounds on the mixing parameter. The dominant decay channel is $n_1 \to 3\nu$ through active-sterile mixing the weak interactions of ν. Another possible decay channel could be $n_1 \to \nu(h_1^* \to \gamma\gamma)$, where the off-shell h_1 decays to 2γ final state through a muon loop. But the choice of $(m_{\nu_d})_1 = 0$ forbids this channel as $(y_{nh_1})_{11}$ is directly proportional to $(m_{\nu_d})_1$. The expression of the decay width of n_1 decaying into 3ν is given

by [80, 81]

$$\begin{aligned}\Gamma_{n_1} &= \frac{G_F^2 m_{n_1}^5 \theta^2}{96\pi^3} \\ &\simeq \frac{\theta^2}{1.5\times 10^{14}\ \text{sec}}\left(\frac{m_{n_1}}{10\ \text{keV}}\right)^5 .\end{aligned} \tag{2.47}$$

The lifetime of n_1 is given by $\tau_{n_1} = 1/\Gamma_{n_1}$. As the decay of n_1 is not protected by any symmetry, the only way it can be viable dark matter candidates is that it is long-lived enough. To satisfy that condition we need $\tau_{n_1} \gg t_U$, where $t_U = 4.4 \times 10^{17}$ sec [32] is the age of the Universe. This in turn gives a bound on the mixing parameter,

$$\theta^2 \ll 3.4\times 10^{-4}\left(\frac{10\ \text{keV}}{m_{n_1}}\right)^5 . \tag{2.48}$$

In the following, we consider the possible production mechanism of such particles in the early Universe. As they were not in the thermal equilibrium with the SM particles due to their weak interaction strength, there must be some other model dependent mechanism. We consider two benchmark scenarios with two different possible production mechanism.

1. BP1: $m_{n_1} = 2$ keV: The production mechanism considered here is the non-resonant Dodelson-Widrow mechanism [82], where the sterile neutrinos mix with the active neutrinos and produced at high temperature through the mixing angle suppressed weak interactions. This mixing generically arises in the type-I see-saw scenarios and we have estimated the mixing angle to be $\theta^2 \simeq 6\times 10^{-9}$ for the 2 keV n_1 as shown in Table. **??**.For a given thermal history of the Universe, the dark matter relic density is uniquely determined by m_{n_1} and θ^2 as follows [83]

$$\Omega_{n_1} h^2 \sim 0.1\left(\frac{\theta^2}{3\times 10^{-9}}\right)\left(\frac{m_{n_1}}{3\text{keV}}\right)^{1.8} , \tag{2.49}$$

   where $h = .72 \pm 0.08$ [32]. This also gives $\theta^2 \simeq 6\times 10^{-9}$ for the 2 keV n_1. This benchmark is safe from the structure formation bounds and X-ray search bounds [84].

2. BP2: $m_{n_1} = 7$ keV: We use the Shi-Fuller mechanism [85] to produce n_1. This bench-

mark point gives $\theta^2 \simeq 10^{-11}$ which is favored by X-ray searches [84]. In this mechanism lepton asymmetry of the model plays vital role. It produces large enhancement due to the Mikheyev-Smirnov-Wolfenstein (MSW) effect [86, 87]. The dark matter relic density is controlled by the lepton asymmetry and the mass and is given by,

$$\Omega_{n_1} h^2 \sim 0.1 \left(\frac{m_{n_1}}{1\text{keV}}\right) \left(\frac{\Delta L}{0.02}\right) , \tag{2.50}$$

where ΔL is the lepton asymmetry. We need $\Delta L \sim 3 \times 10^{-3}$ to get the correct relic density. We can introduce lepton asymmetry in our model by considering CP-violation in the lepton sector. The decay of 7 keV n_1 can be the source of the recently observed 3.5 keV line in the X-ray spectra of the galaxies [88, 89, 90] with $\theta^2 \simeq 10^{-11}$ [84].

For simplicity, we will consider only CP-conserving real Yukawa sector and $m_{n_1} \sim \mathcal{O}(1 - 10)$ keV for our studies, though a complete study can include the CP-violating lepton sector with more freedom in the mixing parameter.

2.4 Light Scalar

We obtain an interesting physical scalar spectrum in this section, which has phenomenological significance. Specifically, we want to produce one light physical scalar with mass $\mathcal{O}(100 - 200)$ MeV. This light scalar when interacts with the SM fermions can produce tree-level FCNC, which will be usefull for the rest of the analysis. The rest of the physical scalars are heavy enough to satisfy the LHC constraints. We summarize the values of the free parameters of the scalar potential in Table. 2.2 along with a specific benchmark points. The mass parameters $O(100)$ GeV and couplings $\lambda_i \sim 0.01 - 0.1$ can give the desired light physical scalar with mass ~ 100 MeV.

The physical scalar masses and the possible final states in the detectors are summarized in Table. 2.3. Note that, the SM Higgs h can decays to a pair of the light scalar h_1 through $h \to h_1 h_1$, where h_1 mostly decays to dark matter pair. Therefore this decay can contribute to the invisible decay branching channel of the SM Higgs. For the given choice of parameters, we get the hh_1h_1 coupling is 0.42 with Br($h \to$ invisible) $= 0.01$. This is consistent with the LHC bounds which

Parameters	Descriptions and Values	Benchmark Values
m_1^2, m_2^2, m_{12}^2 $m_S^2, m_{S'}^2$	$\sim [\mathcal{O}(100)\text{ GeV}]^2$, $m_1^2 < 0, m_{12}^2 < 0$	$m_1^2 = -(88.7)^2\text{ GeV}^2$ $m_2^2 = (497)^2\text{ GeV}^2$ $m_{12}^2 = -(55)^2\text{ GeV}^2$ $m_S^2 = (277.7)^2\text{ GeV}^2$ $m_{S'}^2 = (199.8)^2\text{ GeV}^2$
m_{1S}, m_{2S} m_{12S}	$\sim \mathcal{O}(100)$ GeV, $m_{1S} = 0, m_{12S} > 0$	$m_{1S} = 0$ $m_{2S} = 50$ GeV $m_{12S} = 50$ GeV
$\lambda_1, \lambda_2, \lambda_3, \lambda_4$ $\lambda_5, \lambda_6, \lambda_7$ λ_S, λ_{12S}	$\sim \mathcal{O}(0.1)$, $\lambda_1, \lambda_5, \lambda_6 > 0$	$\lambda_1 = 0.26$ $\lambda_2, \lambda_3, \lambda_4, \lambda_5, \lambda_6, \lambda_7$ $\lambda_S, \lambda_{12S} = 0.1$
$\lambda_{1S}, \lambda_{2S}$	$\sim \mathcal{O}(0.01)$	$\lambda_{1S} = \lambda_{2S} = 0.01$

Table 2.2: The descriptions of the free parameters of the scalar sector defined in Eq. 4.3. We choose the given range of values to generate a light scalar with mass ~ 100 MeV and other heavy scalars consistent with the LHC bounds. We show one specific BP for the purpose. The value of v is 246 GeV.

gives Br($h \to$ invisible) < 0.24 at 95% Confidence Level (C.L.) [91, 92].

For the rest of the analysis, we assume that the light scalar h_1 is lighter than the muon and promptly decays mainly to $\bar{n}_1 n_1$ pair with relatively small branching fraction to e^+e^- pair as well. The partial decay widths are given as,

$$\Gamma(h_1 \to \bar{n}_1 n_1) = (y_{nnh_1})_{11}^2 \times \frac{m_{h_1}}{16\pi}\left(1 - \frac{4m_{n_1}^2}{m_{h_1}^2}\right)^{3/2} , \tag{2.51}$$

$$\Gamma(h_1 \to e^+e^-) = (y_{eh_1})_{11}^2 \times \frac{m_{h_1}}{8\pi}\left(1 - \frac{4m_e^2}{m_{h_1}^2}\right)^{3/2} . \tag{2.52}$$

with a negligible branching fraction to di photon final states. Therefore the total decay width can be written as, $\Gamma_{h_1} = \Gamma(h_1 \to \bar{n}_1 n_1) + \Gamma(h_1 \to e^+e^-)$, and the lifetime is $\tau_{h_1} = 1/\Gamma_{h_1}$. For the purpose of our study we set the couplings, $(y_{nnh_1})_{11} = 7 \times 10^{-5}$ and $(y_{eh_1})_{11} = 10^{-5}$. Therefore

Particles	Mass values for the benchmark of Table. 2.2	Possible final states
Charged scalars : $h^{\pm}$ $m_{h^{\pm}} \sim \mathcal{O}(500)$ GeV	$m_{h^{\pm}} = 500$ GeV	$h^+ \to \bar{d}_i u_j$, $e_i^+ +$MET
Neutral scalars : h, h_1, h_2 $m_{h_1} \sim \mathcal{O}(.1)$ GeV $m_{h_2} \sim \mathcal{O}(500)$ GeV	$m_h = 125.5$ GeV, $m_{h_1} = 0.15$ GeV $m_{h_2} = 500$ GeV	$h, h_2 \to \bar{f}_i f_j$, $\gamma\gamma, h_1 h_1$ $h_1 \to e^+ e^-$, $\bar{n}_1 n_1$
Neutral pseudoscalars : s_1, s_2 $m_{s_i} \sim \mathcal{O}(500)$ GeV	$m_{s_1} = 500$ GeV, $m_{s_2} = 400$ GeV	$s_{1,2} \to \bar{e}_i e_j$, $\bar{d}_i d_j$

Table 2.3: The descriptions of the physical scalar mass spectrum and the possible final states in the detectors for the BP defined in Table 2.2.

the lifetime of h_1 for $m_{n_1} = \mathcal{O}(1-10)$ keV and m_{h_1} in the range $100 - 200$ MeV, is given as $\tau_{h_1} \simeq 7 \times 10^{-14}$ sec. The branching fractions are,

$$\begin{aligned} \text{Br}(h_1 \to \bar{n}_1 n_1) &\simeq 0.95 \,, \\ \text{Br}(h_1 \to e^+ e^-) &\simeq 0.05 \,. \end{aligned} \tag{2.53}$$

In the following, we discuss different bounds relevant for the $\mathcal{O}(100)$ MeV scalar.

1. Fixed target/ beam dump experiments: These experiments can put bounds in the $(m_{h_1}, (y_{eh_1})_{11})$ and $(m_{h_1}, (y_{eh_1})_{22})$ parameter space. We show them in Fig. 2.2 and Fig. 2.3 along with future projection from the NA64 [25] experiments. In these experiments, e-bremsstrahlung can give rise to the h_1 production. It then decays to either $\bar{n}_1 n_1$ or $e^+ e^-$ pair when $m_{h_1} < 2m_\mu$. NA64 [25] experiment is sensitive to the invisible final states while experiments like E137 [93, 94, 10, 95] and Orsay [95] are sensitive to $e^+ e^-$ final states.

2. Kaon decay: Rare Kaon decays produced by the h_1 mediated process and tree-level FCNC

can put bounds on the $(m_{h_1}, (y_{dh_1})_{21})$ parameter space. LSND [96] can also put bounds on this parameter space [97].

3. B-meson decay: Due to the presence of the tree-level FCNC in the quark sector, rare B decay process like $B \to K\mu^+\mu^-$ can occur via h_1 mdeiated diagram and can put bounds from the LHCb results [98]. We assume that the coupling that give rise to this process to be $(y_{dh_1})_{32} \sim 0$ without affecting any of the results of our analysis. Due to this assumption, the decay is highly suppressed and we can neglect the LHCb bounds.

4. Supernova cooling, ΔN_{eff}, BBN: The astrophysical and the cosmological bounds are very weak [99, 2] for the mass range of interest and therefore we do not show them here.

2.5 Anomalous Magnetic Moment of Muon and Electron

There is a 3.7σ tension between the theoretical predictions [100, 101, 102, 103] and the experimental results [36, 37] of the anomalous magnetic moment of the muon, given as,

$$\Delta a_\mu = a_\mu^{exp} - a_\mu^{th} = (2.74 \pm .73) \times 10^{-9}. \tag{2.54}$$

Theoretical efforts are underway to improve the precision of the SM calculations [104, 105, 106, 107, 108] by various methods such as by computing the hadronic light-by-light contribution with all errors under control by using lattice QCD. Recently one such result [109] was found to be consistent with the previous predictions, hinting towards a new physics explanation of the discrepancy. On the other hand, the ongoing experiment at Fermilab [110, 111] and one planned at J-PARC [112] are aiming to reduce the uncertainty further.

Recently this was compounded with a 2.4σ tension between the experiment [39, 38] and theory [113] values of the anomalous magnetic moment of electron, given by,

$$\Delta a_e = a_e^{exp} - a_e^{th} = (-8.7 \pm 3.6) \times 10^{-13}. \tag{2.55}$$

The fact that, the deviations are in the opposite direction and $\Delta a_e / \Delta a_\mu$ does not follow the

lepton mass scaling, $m_e^2/m_\mu^2 \sim 2.25 \times 10^{-5}$ indicates that a new physics solution is needed to explain them simultaneously. Few such solutions can be found in [114, 115, 116, 117, 118, 119, 120, 121, 122, 123, 124, 125, 126, 127, 128, 129, 130].

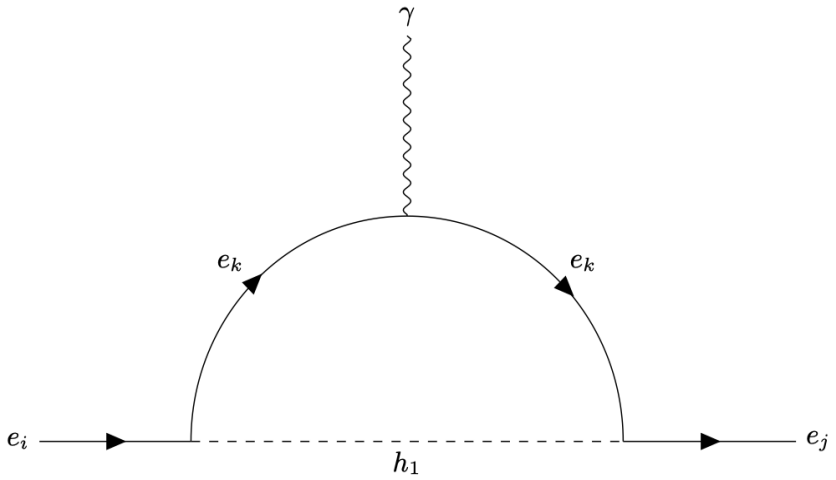

Figure 2.1: We adopt a notation to denote a diagram as $e_i e_j, e_k$ where e_i, e_j are the leptons in the outer legs and e_k runs inside the loop. Similar diagrams with heavier scalars are also possible which are further suppressed by the large masses of the scalar particles.

We rely on the tree-level lepton flavor violating couplings of the light scalar h_1 to solve the puzzle. The one-loop diagrams mediated by h_1 with different leptons inside the loop, that contribute to the calculations are shown in Fig. 2.1 . In general, there can be 6 different realizations of each process with three leptons inside the loop and different chirality of e_i and e_j. We assume an asymmetric Yukawa matrix, $(y_{eh_1})_{ij}$ and get that $\bar{e}_{iL} e_{jR} h_1$ and $\bar{e}_{iR} e_{jL} h_1$ couplings are different. We utilize this to get the opposite sign for Δa_μ and Δa_e. We further assume that some of the elements of $(y_{eh_1})_{ij}$ are zero, for simplicity.

The one loop diagrams with muon inside the loop will contribute most to a_μ. The contribution

can be written as, [131]

$$\Delta a_{\mu\mu,\mu} = (y_{eh_1})^2_{22} \ \frac{m_\mu^2}{4\pi^2} \ \int_0^1 dx \frac{2x^2 - x^3}{x^2 m_\mu^2 + (1-x) m_{h_1}^2} \ . \tag{2.56}$$

The related parameter space plot in $(m_{h_1}, (y_{eh_1})_{22})$ plane is shown in Fig. 2.2. Here, we show the allowed parameter space as well as the relevant future bounds. This parameter space is allowed by all the muon experiment as $m_{h_1} < 2m_\mu$.

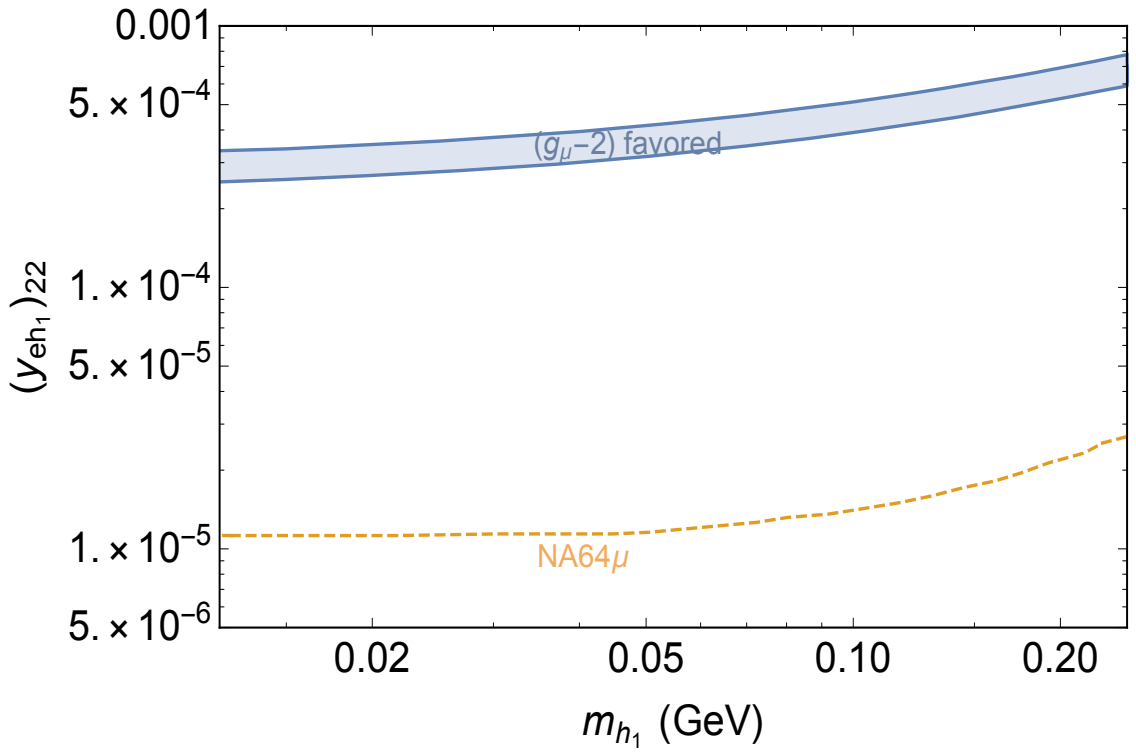

Figure 2.2: The allowed region in the parameter space favored by Δa_μ is shown as blue shaded region. The relevant region of parameter space also satisfy the constraints from all muon experiment.

The electron magnetic moment case is not as straightforward as the muon case. Both tau and electron-induced loop diagrams are non-vanishing and the corresponding contributions to the

electron anomalous magnetic moment are [131]

$$\Delta a_{ee,\tau} = (y_{eh_1})_{13}\,(y_{eh_1})_{31}\,\frac{m_e^2}{4\pi^2} \times \int_0^1 dx \frac{x^2 - x^3 + \frac{m_\tau}{m_e}x^2}{x^2 m_e^2 + x(m_\tau^2 - m_e^2) + (1-x)m_{h_1}^2}\,, \tag{2.57}$$

$$\Delta a_{ee,e} = (y_{eh_1})_{11}^2\,\frac{m_e^2}{4\pi^2}\int_0^1 dx \frac{2x^2 - x^3}{x^2 m_e^2 + (1-x)m_{h_1}^2}\,. \tag{2.58}$$

It is interesting to note that $\Delta a_{ee,e}$ always gives positive contributions while $\Delta a_{ee,\tau}$ can be negative if one of the couplings is negative because of the chiral nature of the couplings. Therefore we require that $\Delta a_{ee,\tau}$ gives the dominating contribution, and $\Delta a_{ee,\tau} + \Delta a_{ee,e}$ explains the deviation. We show various bounds in the $(m_{h_1}, (y_{eh_1})_{11})$ plane in Fig. 2.3.

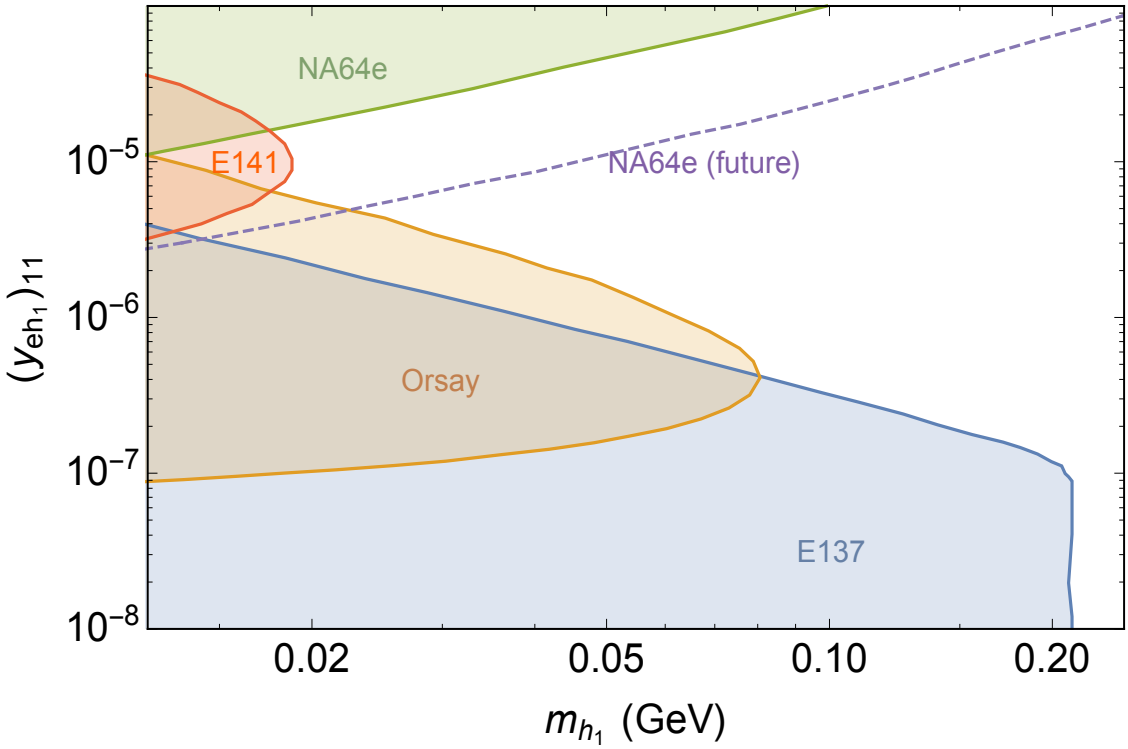

Figure 2.3: The excluded regions are shown as the shaded regions and the dotted lines denote the future bounds.

Here we show one benchmark scenario that gives correct values and signs for both Δa_μ and Δa_e. The light scalar mass is taken to be $m_{h_1} = 140$ MeV, and the Yukawa matrix $(y_{eh_1})_{ij}$ is given by

$$(y_{eh_1})_{ij} \simeq \begin{pmatrix} 10^{-5} & 0 & -6.8 \times 10^{-4} \\ 0 & 5.13 \times 10^{-4} & 10^{-7} \\ 3.5 \times 10^{-4} & 0 & 0 \end{pmatrix} . \tag{2.59}$$

Note that, these values do not vary much for the mass range $m_{h_1} = \mathcal{O}(100 - 200)$ MeV.

The Yukawa matrix presented in Eq. 2.59 can introduces flavor violating decays in the lepton sector, mediating through the light scalar h_1 such as: $\mu \to e\gamma$ with τ inside the loop, $\tau \to e\gamma$ with e inside the loop and $\tau \to \mu\gamma$ with μ inside the loop. The analytical expression of the branching fractions of these decay channels is given in Eq. B.1 of Appendix. B. We show the values of these branching ratios for our benchmark and the corresponding experimental bounds [132, 133] in Table 2.4. We get that the branching ratios are safe from the experimental bounds. Note that, the values do not change significantly over the mass range $m_{h_1} = \mathcal{O}(100 - 200)$ MeV.

Descriptions	Values for $m_{h_1} = 140$ MeV	Experimental bounds
Br($\mu \to e\gamma$)	5.75×10^{-14}	$< 4.2 \times 10^{-13}$
Br($\tau \to e\gamma$)	1.15×10^{-11}	$< 1.1 \times 10^{-7}$
Br($\tau \to \mu\gamma$)	1.92×10^{-15}	$< 4.5 \times 10^{-8}$

Table 2.4: We summarize the values of different lepton flavor violating processes for the Yukawa matrix of Eq. 2.59. We also show corresponding experimental bounds.

2.6 KOTO Anomaly

Rare Kaon decay processes such as $K_L^0 \to \pi^0\nu\bar{\nu}$ and $K^+ \to \pi^+\nu\bar{\nu}$ are good candidates to search for in order to probe the physics beyond SM [42, 134, 135, 136, 137, 138, 139, 140]. In

SM, these processes are loop suppressed [141, 142] and the predictions are [42]

$$\text{Br}(K_L^0 \to \pi^0 \nu\bar{\nu})_{\text{SM}} = (3.00 \pm 0.30) \times 10^{-11} \tag{2.60}$$

$$\text{Br}(K^+ \to \pi^+ \nu\bar{\nu})_{\text{SM}} = (9.11 \pm 0.72) \times 10^{-11} \tag{2.61}$$

Therefore observation of such events in an experiment would require new physics ideas to explain them. The KOTO experiment [143, 144] at J-PARC [145] and NA62 experiment [146] at CERN are dedicated to study these processes and searching for new signals. In a recent run in the KOTO experiment, four candidate events were suspected as new signals over the SM prediction of 0.10 ± 0.02 [40, 41], which were observed in the signal region of $K_L^0 \to \pi^0 \nu\bar{\nu}$. One of the event was suspected as a background coming from the SM upstream activity. The other three events can be considered as signals as they are not consistent with the currently known background and are consistent with

$$\text{Br}(K_L^0 \to \pi^0 \nu\bar{\nu})_{\text{KOTO19}} < 2.1^{+2.0(4.1)}_{-1.1(-1.7)} \times 10^{-9} \tag{2.62}$$

at 68(90)% C.L., including statistical uncertainties, given, single event sensitivity as 6.9×10^{-10} [40, 41]. The photons and invisible final states were interpreted as $\nu\bar{\nu}$ in their study. The central value is almost two orders of magnitude larger than the SM prediction and is in agreement with their previous bounds [147]

$$\text{Br}(K_L^0 \to \pi^0 \nu\bar{\nu})_{\text{KOTO18}} < 3.0 \times 10^{-9} \,. \tag{2.63}$$

The KOTO experiment did not see any excess events for the charged Kaon decay while NA62 puts a bound on such processes [148]

$$\text{Br}(K^+ \to \pi^+ \nu\bar{\nu})_{\text{NA62}} < 2.44 \times 10^{-10} \tag{2.64}$$

at 95% C.L., which is consistent with the SM prediction of Eq. 2.61.

One need to satisfy the Grossman-Nir (GN) bound [149] for the neutral and charged kaon

decays, which depends on the isospin symmetry and kaon lifetimes. The bound is given as,

$$\mathrm{Br}\left(K_L^0 \to \pi^0 \nu\bar{\nu}\right) \leq 4.3 \times \mathrm{Br}\left(K^+ \to \pi^+ \nu\bar{\nu}\right) \ , \tag{2.65}$$

To explain the anomalous events found by KOTO, the new physics explanation should satisfies this bound.

We utilize the tree-level FCNC in the quark sector mediated by h_1 to generate the coupling, $(y_{dh_1})_{21}$ necessary for Kaon decay to pion. This gives rise to the tree-level $s \to d$ transition through h_1. The neutral/charged Kaon decays to a neutral/charged pion and a h_1, which then promptly decays to a pair of dark matter or an electron pair. The dark matter final states, $\mathrm{Br}(K_L^0 \to \pi^0 n_1 \bar{n}_1)$ can mimic the invisible search and give the desired branching fraction. There is a kinematic cut in the mass range $\sim m_\pi \pm 25$ MeV [148, 150, 151, 152] for the $\mathrm{Br}(K^+ \to \pi^+ + \text{invisible})$ bound. We utilize this fact and choose the mass m_{h_1} in that range to evade the GN bound.

The decay width of K_L^0 decaying into a neutral pion and an on-shell h_1 is

$$\begin{aligned} \Gamma(K_L^0 \to \pi^0 h_1) \ &= \ \frac{[\mathrm{Re}(y_{dh_1})_{21}]^2}{16\pi m_{K_L^0}} \left(\frac{m_{K^0}^2 - m_{\pi^0}^2}{m_s - m_d}\right)^2 \\ & \qquad f^2(m_{h_1}^2) \times \ \lambda^{1/2}\left(1, \frac{m_{\pi^0}^2}{m_{K_L^0}^2}, \frac{m_{h_1}^2}{m_{K_L^0}^2}\right) \ , \end{aligned} \tag{2.66}$$

where $\lambda(x,y,z) = x^2 + y^2 + z^2 - 2xy - 2yz - 2zx$ is the triangle function, and the function $f(q^2)$ for the vector form factor is given as [153]

$$f(q^2) \ = \ f_+(0)\left(1 + \frac{\lambda_0}{m_\pi^2} q^2\right) \tag{2.67}$$

with $f_+(0) = 0.97$ and $\lambda_0 = 1.8 \times 10^{-2}$.

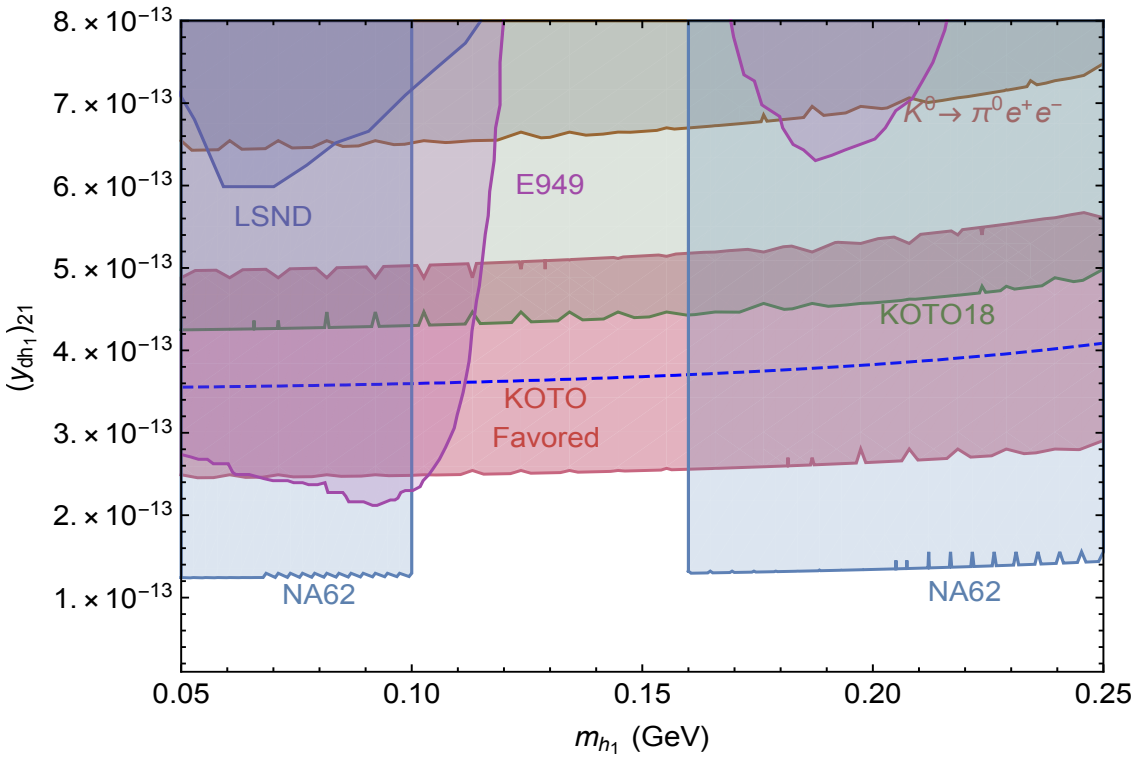

Figure 2.4: The parameter space favored by the KOTO anomaly in our model is shown as the pink shaded region and the contour corresponding to the central value of the KOTO anomaly is the blue dashed line. The green contour corresponds to the KOTO18 excluded region. Contour line corresponding to the $K_L^0 \to \pi^0 e^+ e^-$ decay is shown in brown. The excluded region by NA62, E949 and LSND are also shown.

The decay width of K_L^+ decaying into a charged pion and an on-shell h_1 is

$$\Gamma(K^\pm \to \pi^\pm h_1) = \frac{|(y_{dh_1})_{21}|^2}{16\pi m_{K^\pm}} \left(\frac{m_{K^\pm}^2 - m_{\pi^\pm}^2}{m_s - m_d}\right)^2 f^2(m_{h_1}^2) \times \lambda^{1/2}\left(1, \frac{m_{\pi^\pm}^2}{m_{K^\pm}^2}, \frac{m_{h_1}^2}{m_{K^\pm}^2}\right) . \quad (2.68)$$

The light scalar, h_1 produced in the decay of the kaon is short-lived with typical lifetime $\tau_{h_1} \simeq 10^{-13}$ sec, can travels $\gamma c \tau_{h_1} \simeq 10^{-4}$ m before it decays, assuming it's energy to be $E_{h_1} \simeq 1.5$ GeV. Therefore h_1 decays inside the detector as the length of the KOTO detector is 3 m . It can promptly

decay into $n_1\bar{n}_1$ or e^+e^- pair with branching fractions of 0.95 and 0.05, respectively. So we get

$$\begin{aligned} \text{Br}(K_L^0 \to \pi^0 n_1 \bar{n}_1) &= \frac{\Gamma(K_L^0 \to \pi^0 h_1) \times \text{Br}(h_1 \to n_1 \bar{n}_1)}{\Gamma_{K_L^0}}, \\ \text{Br}(K_L^0 \to \pi^0 e^+ e^-) &= \frac{\Gamma(K_L^0 \to \pi^0 h_1) \times \text{Br}(h_1 \to e^+ e^-)}{\Gamma_{K_L^0}}, \end{aligned} \tag{2.69}$$

where $\Gamma_{K_L^0} = \Gamma^{\text{SM}}_{K_L^0} + \Gamma(K_L^0 \to \pi^0 n_1 \bar{n}_1) + \Gamma(K_L^0 \to \pi^0 e^+ e^-)$ with $\Gamma^{\text{SM}}_{K_L^0} = (1.29 \pm 0.01) \times 10^{-17}$ GeV. We get similar expressions for the $K^\pm$ decays. Fig. 2.4 shows the favored parameter space in $(m_{h_1}, (y_{dh_1})_{21})$ plane for KOTO anomalous events. We also show the other relevant constraints.

Note that, the non-zero coupling $(y_{dh_1})_{21}$ can gives rise to the tree-level $K^0 - \bar{K}^0$ mixing mediated through h_1. The contribution of this mixing to the $K_L - K_S$ mass difference can be expressed as,

$$\Delta m_K = -\frac{2(y_{dh_1})_{21}^2}{m_{h_1}^2} \frac{f_K^2 m_K^2}{12 m_K} \left[1 - \frac{m_K^2}{(m_s + m_d)^2}\right] , \tag{2.70}$$

where, $\Delta m_K^{\text{exp}} = 3.52 \times 10^{-15}$ GeV [37]; $f_K \simeq 1.23 m_\pi$ is the kaon decay constant [37]. One needs $(y_{dh_1})_{21} < 10^{-8}$ to avoid this constraint for the mass range $m_{h_1} = \mathcal{O}(100 - 200)$ MeV, which is obviously satisfied in our discussions above.

2.7 MiniBooNE Excess

MiniBooNE experiemnt recently, in 2018, has reported a 4.7σ excess of $\nu_e + \bar{\nu}_e$ like events over the estimated background in the energy range $200 < E_\nu^{QE} < 1250$ MeV [43]. This was the result of 15 years of data taking. The total excess events was found to be 460.5 ± 99.0 corresponding to 12.84×10^{20} protons on target in neutrino mode and 11.27×10^{20} protons on target in antineutrino mode. A year after from the announcement, the result was updated with 638 ± 132.8 electron-like events (4.8σ) as the reported number of excess events corresponding to 18.75×10^{20} protons on target in neutrino mode and 11.27×10^{20} protons on target in antineutrino mode [44]. Both of these are in tension with the simple two-neutrino oscillation mechanism within the standard three

neutrino scenario of SM.

Several explanation of these excess events can be found in the literature within the context of dark neutrino mass models using heavy sterile neutrinos and dark gauge bosons [154, 155, 156, 157, 158, 159] and dark sector models with dark scalars [160]. In all such scenarios, it was considered that the light neutrinos upscatter to a heavy neutrino after coherent scattering off the nucleus and subsequent decay of the heavy neutrino into a pair of electrons. The neutrino energy can be reconstructed using the energy and angular distribution of the mediator coming from the sterile neutrino decay [161]. Note that, the MiniBooNE detector can not distinguish the electron pair.

Fig. 2.5 shows the Feynman diagram that gives rise to the excess events at the MiniBooNE detector. Here, the heavy sterile neutrino n_2 can be produced from the upscattering process: $\nu_2 A \to n_2 A$ mediated through the light scalar h_1, which is enhanced by $\sim A^2$ as it is a coherent scattering. The heavy sterile neutrino, n_2 then decays into n_1 and an on-shell h_1, which subsequently decays into a pair of e^+e^- with $\text{Br}(h_1) \to e^+e^- \simeq 5\%$. We estimate the path length they travel before decay as $l_{n_2} \leq 10^{-4}$ m and $l_{h_1} \simeq 10^{-4}$ m, taking the typical energies as, $E_{n_2}, E_{h_1} \sim 1$ GeV. Note that, there is an advantage for the scalar mediator models in comparison to the vector gauge boson mediated explanations. The parameter space requied for the explanation in the dark gauge boson models are constrained by CHARM-II data [162], since the scattering cross-section get enhanced for large neutrino energy. On the other hand, the scattering cross section are much smaller for large neutrino energy in the scalar models [160].

The total number events that will be observed by the MiniBooNE detector, given both the heavy neutrino n_2 and the light scalar h_1 decay promptly, can be written as,

$$N_{\text{event}} \;=\; f_{\text{exp}} \int_{E_{\nu_{\text{min}}}}^{E_{\nu_{\text{max}}}} dE_\nu \Phi(E_\nu) \int_{E_{R_{\text{min}}}}^{E_{R_{\text{max}}}} dE_R \times \frac{d\sigma(E_R, E_\nu)}{dE_R} \times \text{Br}(h_1 \to e^+e^-)\,, \quad (2.71)$$

where f_{exp} is a factor which depends on the details of the experiment, including the numbers of protons on target, exposure, effective area of the detector; E_R is the recoil energy of the target

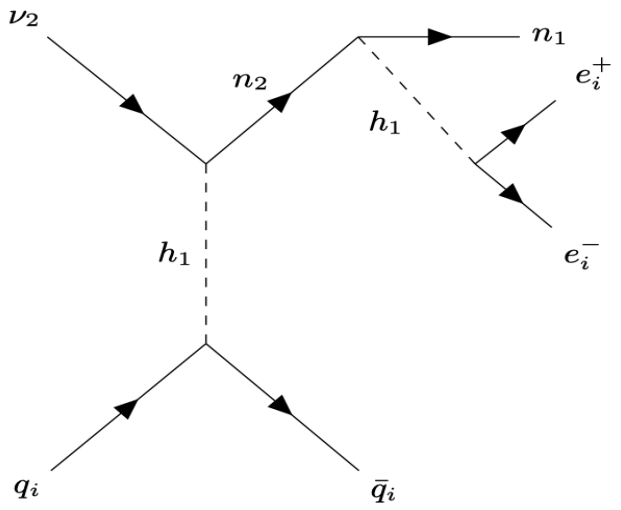

Figure 2.5: The Feynman diagram for the upscattering process $\nu A \to nA$. This diagram contributes to the cross section which will give rise to the MiniBooNE excess events in our model.

nuclei; E_ν is the energy of the incoming neutrino ; and $\Phi(E_\nu)$ is the incoming neutrino flux from the Booster Neutrino Beam (BNB) line at Fermilab [163]. Therefore, one can define a model dependent quantity as, $f_{\text{model}} = N_{\text{event}}/f_{\text{exp}}$. The differential scattering cross section is given as follows,

$$\frac{d\sigma}{dE_R} = [Zf_p + (A-Z)f_n]^2 \frac{(y_{nh_1})_{22}^2}{16\pi E_\nu^2} \frac{(m_{n_2}^2 + 2m_A E_R)(2m_A + E_R)}{(m_{h_1}^2 + 2m_A E_R)^2} F^2(E_R)\,, \quad (2.72)$$

where m_A is the mass of the target nucleus; Z and $A-Z$ are the proton and neutron numbers of the target nucleus; $F(E_R)$ is the nuclear form factor [164, 165]; the factors $f_{p,n}$ are defined as [166]

$$\frac{f_{p,n}}{m_N} = \sum_{q=u,d,s} f_{T_q}^{(p,n)} \frac{f_q}{m_q} + \frac{2}{27}\left(1 - \sum_{q=u,d,s} f_{T_q}^{(p,n)}\right) \sum_{q=c,b,t} \frac{f_q}{m_q}. \quad (2.73)$$

We take, $f_{(u,d)} = (y_{(u,d)h_1})_{11}$ and $f_{s,c,b,t} = 0$. The constants $f_{T_u}^{(p)}$, $f_{T_d}^{(p)}$, $f_{T_u}^{(n)}$ and $f_{T_d}^{(n)}$ are taken to have the values 0.020, 0.041, 0.0189, and 0.0451, respectively [167, 168, 169, 170, 171].

In Fig. 2.6 we show the allowed range of n_2 masses for $m_{h_1} = \mathcal{O}(100 - 200)$ MeV to generate the MiniBooNE events given the couplings : $(y_{nh_1})_{22} = 6.1 \times 10^{-2}$, $(y_{uh_1})_{11} = 5.0 \times 10^{-6}$ and

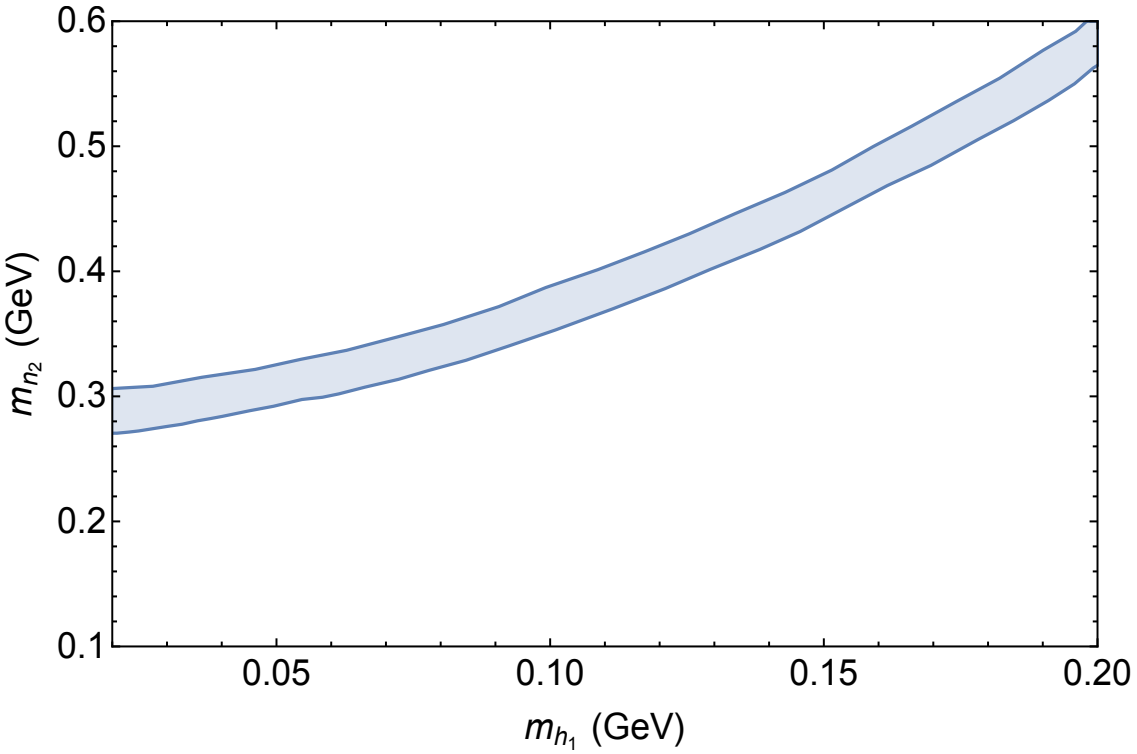

Figure 2.6: The allowed parameter space in the (m_{h_1}, m_{n_2}) plane which gives the desired numbers of total events is shown as the blue shaded region.

$(y_{dh_1})_{11} = 5.0 \times 10^{-6}$. Note that the masses of n_2 is consistent with the neutrino mass generation and mixings, as shown in Table. 2.1.

In Fig. 2.7, we show the total cross section versus the incoming neutrino energy for the benchmark values: $m_{n_2} = 420$ MeV and $m_{h_1} = 140$ MeV. Note that, the cross-section is small at, $E_{\nu_\mu} = 20$ GeV [172] the energy scale of the CHARM-II experiment [173, 174, 175], therefore gives no excess events [160]. If the decay length of the heavy sterile neutrino n_2 has decay length $l_{n_2} \leq 10^{-4}$ m, then the scalar mediated process does not produce any excess events [176] in T2K ND280 [177, 178, 179, 180, 181, 182] and MINERνA [183, 184, 185, 186] experiments. The model-dependent parameter f_{model}, is consistent with other dark gauge bosons [155, 162] or dark scalar models [160].

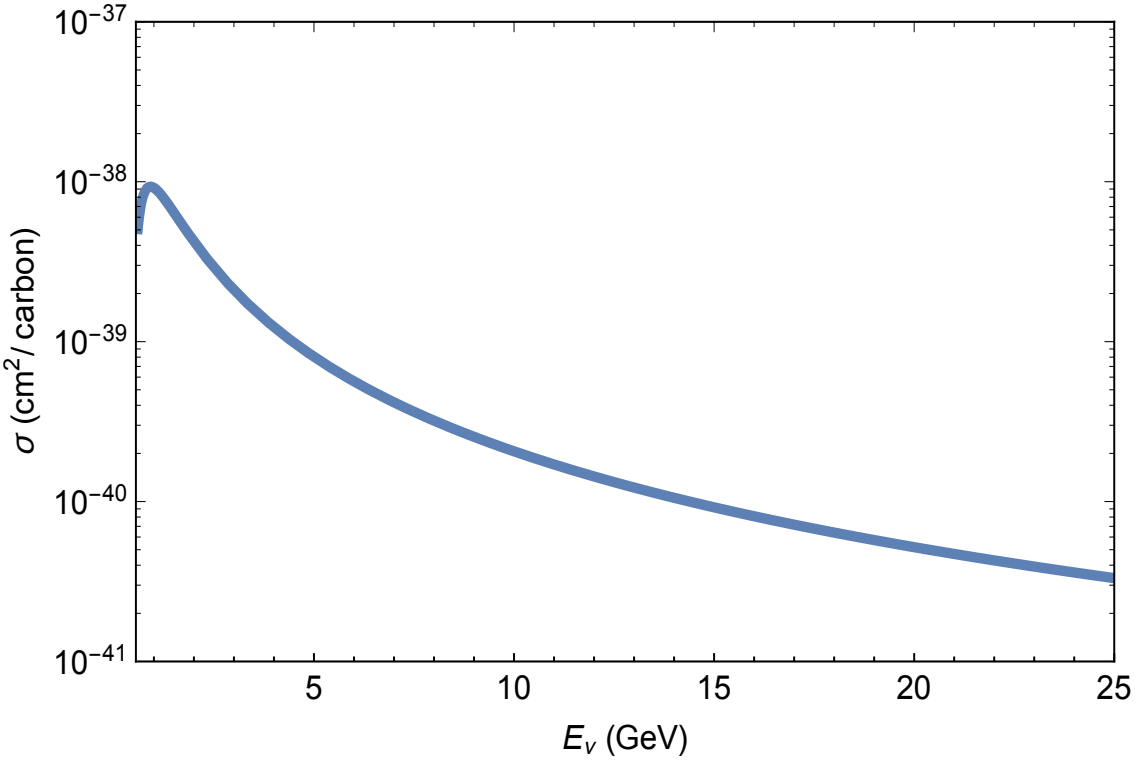

Figure 2.7: The solid blue line shows the corss-section of the upscattering process as a function of the incoming neutrino energy. We have used the following BP: $m_{n_2} = 420$ MeV, $m_{h_1} = 140$ MeV, $(y_{nh_1})_{22} = 6.1 \times 10^{-2}$, $(y_{uh_1})_{11} = 5.0 \times 10^{-6}$, and $(y_{dh_1})_{11} = 5.0 \times 10^{-6}$.

2.8 Discussions

The main focus of this chapter was to present a complete model that can address the issues of neutrino mass and mixings, and the observed dark matter relic density. We also addressed few recent anomalous experimental results using the framework of this model. And we found a parameter space, which is allowed by all the current data, can explain all the anomalies simultaneously.

To justify our claim, we choose three benchmark points in the allowed region of the parameter space and show that they produce the correct observables. The becnhmark points are summarized in Table. 2.5. For all the benchmark scenarios the following couplings were taken to be fixed: $(y_{nnh_1})_{11} = 7 \times 10^{-5}$, $(y_{eh_1})_{11} = 1 \times 10^{-5}$, $(y_{nh_1})_{22} = 6.1 \times 10^{-2}$, $(y_{uh_1})_{11} = 5.0 \times 10^{-6}$, and $(y_{dh_1})_{11} = 5.0 \times 10^{-6}$. The observables calculated based on these benchmark values are summarized in Table. 2.6.

Parameters	BP1	BP2	BP3
m_{h_1}(MeV)	130	140	150
m_{n_1}(keV)	2	3	2
m_{n_2}(MeV)	435	420	440
$(y_{eh_1})_{22}$	5×10^{-4}	4.75×10^{-4}	5.5×10^{-4}
$(y_{eh_1})_{13}$	-3.5×10^{-4}	-6×10^{-4}	-6.8×10^{-4}
$(y_{eh_1})_{31}$	6.8×10^{-4}	4×10^{-4}	3.5×10^{-4}
$(y_{dh_1})_{21}$	3×10^{-13}	3.5×10^{-13}	4×10^{-13}

Table 2.5: Three BPs are shown, for which we calculate the different observables quantities, and can account for three anomalies.

Observables	BP1	BP2	BP3
$\Omega_{n_1}h^2$	0.1	0.1	0.1
$\Delta a_\mu \times 10^{-9}$	2.67	2.27	2.86
$\Delta a_e \times 10^{-13}$	-8.43	-8.50	-8.43
$Br(K_L^0 \to \pi^0 n_1 \bar{n}_1) \times 10^{-9}$	1.42	1.91	2.47
$Br(K_L^0 \to \pi^0 e^+ e^-) \times 10^{-11}$	5.81	7.82	1.01
N_{event} $(\nu + \bar{\nu})$	671	644	497

Table 2.6: The observables corresponding to the three BPs.

Therefore the light scalar model studied here appears to be very effective in describing neutrino mass and mixing, explaining the dark matter content of the Universe and explaining recent experimental anomalies. As the experiments gather more data, this model would be probed further.

3. A SUB-GEV DARK MATTER MODEL: $U(1)_{T3R}$ EXTENSION OF SM*

Weakly interacting massive particles (WIMP) were speculated as to the most promising candidate for particle dark matter [28]. But experimental searches, so far, have failed to find any evidence of WIMP. As a result, there is a recent interest in sub-GeV dark matter candidates. The sub-GeV dark matters are very interesting as they can evade the current direct detection constraints and can get the correct relic density (see, for example, [187, 188]) by evading the Planck bound [32]. If we look at the two lightest flavor sectors of SM, the associated mass scale is $\mathcal{O}(100)$ MeV. Therefore, following the idea of the WIMP miracle, if one connects the new physics of the dark sector to the light flavor sector of the SM, the dark matter that arises from that new physics will also lie at that scale. The new physics can also address the Yukawa hierarchy in the light flavor sector. We build a model by connecting the dark sector to the light flavor sector of SM through dark photon/Higgs interactions for right-handed SM fermions by adding a new gauge group $U(1)_{T3R}$ to the SM gauge symmetry. Only the right-handed SM particles are charged under the new gauge symmetry. We also introduce a pair of left and right-handed fermion charged under the new symmetry and SM singlet. The Yukawa sector needs dark Higgs insertion, which gets vacuum expectation value ($V = 10$ GeV) and breaks the symmetry down to parity under which only the new set of fermions are charged and are possible dark matter candidates. The masses of all the particles scale as V and all of them are sub-GeV. One of the most important features of the model is that it has two light mediators: one light scalar and one light gauge boson. The model satisfies all the current direct detection constraints and can give the correct relic abundance satisfying the Planck bounds. Because $U(1)_{T3R}$ couples to chiral fermions, it gets qualitatively new constraints compared to the other well studied $U(1)$ gauge symmetry models. The parameter space is tightly constrained but can satisfy all the current constraints. A variety of upcoming experiments can probe the open parameter space.

*this chapter is reprinted from "**A sub-GeV dark matter model**" by B. Dutta, S. Ghosh and J. Kumar, Phys. Rev. D **100**, 075028 (2019); "**Contributions to ΔN_{eff} from the dark photon of $U(1)_{T3R}$**" by B. Dutta, S. Ghosh and J. Kumar, Phys. Rev. D **102** (2020) 1, 015013; "**Opportunities for probing $U(1)_{T3R}$ with light mediators**" by B. Dutta, S. Ghosh and J. Kumar, Phys. Rev. D **102** (2020) 7, 075041 published by the American Physical Society under the terms of the Creative Commons Attribution 4.0 International license.

The model can also satisfy the recently found new constraints of the anomalous magnetic moment of the muon [189] and can explain the recent value of B-anomalies processes [190].

The rest of the chapter is organized as follows: In Sec. 3.1, we describe the details of the model including all possible interaction terms and the UV completion of the model. We describe various bounds that can put constraints on the parameter space of our model in Sec. 3.2. The direct detection prospects of our model are described in Sec. 3.3. In Sec. 3.4, we talk about ways in which we can obtain the correct thermal relic density of the dark matter particles. The recent results of the flavor violating process, $R_{K^{(*)}}$ are explained in Sec. 3.5. We conclude in Sec. 3.6.

3.1 Model

In this section we describe the setup of our model in detail. The low energy gauge symmetry of our model is given by $SU(3)_C \times SU(2)_L \times U(1)_Y \times U(1)_{T_{3R}}$. The new gauge group $U(1)_{T_{3R}}$ is not connected to electric charge, defined as $Q{=}T_{3L}{+}Y$. This gauge group was first used in the context of left-righ symmetric model [191, 192, 193]. In this scenario, only the right-handed Standard Model (SM) fermions (including a new right-handed neutrino) are charged under the $U(1)_{T_{3R}}$ gauge group and all other SM fields have their usual charges under the SM gauge groups. We add three more new matter fields, a scalar ϕ, and a left and right-handed fermion pair η_L and η_R, which are SM singlets and only charged under $U(1)_{T_{3R}}$.

For simplicity, we assume that only one charged lepton, one up-type quark, one down-type quark, and one neutrino (all right-handed) are charged under $U(1)_{T_{3R}}$ gauge group. This is necessary to cancel all the gauge and gravitational anomalies, though they need not all be in the same generation. We further assume that the up-type quark state is a linear combination of all up-type mass eigenstates while the charged lepton and down-type quark states are mass eigenstates. This was shown technicaly natural in Ref. [99]. We get tight constraints from cosmological observations [1] and atomic parity violation experiments [194], if we take electron as the charged lepton. Therefore we take the right handed muon as the lepton charged under $U(1)_{T_{3R}}$. We also assume that the right-handed u- and d-quarks are charged under $U(1)_{T3R}$ to avoid tight constraints from the Kaon decay process if we take the second generation right handed quarks. We summarize all

fields with non-trivial charges under $U(1)_{T3R}$ in Table 3.1.

field	u_R	d_R	μ_R	ν_R	η_L	η_R	ϕ
q_{T3R}	-2	2	2	-2	1	-1	2

Table 3.1: The charges of the fields which transform under $U(1)_{T3R}$. For the fermionic fields, we list the charges of the left-handed component of the Weyl spinor.

The non-renormalizable low energy interaction Lagrangian of the model can be written as,

$$\begin{aligned}\mathcal{L} &= -\frac{\lambda_u}{\Lambda}\tilde{H}\phi^*\bar{Q}_L u_R - \frac{\lambda_d}{\Lambda}H\phi\bar{Q}_L d_R - \frac{\lambda_\nu}{\Lambda}\tilde{H}\phi^*\bar{L}_L\nu_R - \frac{\lambda_\mu}{\Lambda}H\phi\bar{L}_L\mu_R - m_D\bar{\eta}_R\eta_L \\ &\quad -\frac{1}{2}\lambda_L\phi\bar{\eta}_L^c\eta_L - \frac{1}{2}\lambda_R\phi^*\bar{\eta}_R^c\eta_R - \mu_\phi^2\phi^*\phi - \lambda_\phi(\phi^*\phi)^2 + H.c., \end{aligned} \tag{3.1}$$

where Q_L and L_L are the left-handed SM quark and lepton doublet, respectively; H is the SM Higgs doublet; and $\tilde{H}{=}i\tau_2 H^*$.

The scalar field ϕ obtains a vev, $V{=}(-\mu_\phi^2/2\lambda_\phi)^{1/2}$ and breaks the $U(1)_{T3R}$ down to a Z_2 symmetry. In this process we also get a physical scalar ϕ', which we call a dark Higgs, which comes from the expansion, $\phi = V + \phi'/\sqrt{2}$. All of the SM fields and ϕ' are even under the Z_2 symmetry while only $\eta_{L,R}$ are odd. The mass matrix of η has both Dirac and Majorana mass terms. We assume that the Dirac mass, m_D to be very small compared to the Majorana mass, m_M. We further assume that, $\lambda_L = \lambda_R \equiv \lambda_M$. Therefore, the Majorana masses for the left-handed and the right-handed fields are equal, with $m_M = \lambda_L V = \lambda_R V = (\lambda_M V)$. This gives us two physical Majorana fermions η_1 and η_2, with masses $m_1 = m_M - m_D$ and $m_2 = m_M + m_D$ respectively.

The states are expressed as,

$$\begin{aligned}\eta_1 &= \frac{1}{\sqrt{2}}\begin{pmatrix}\eta_L - \eta_R^c\\ \eta_L^c - \eta_R\end{pmatrix},\\ \eta_2 &= \frac{1}{\sqrt{2}}\begin{pmatrix}\eta_L + \eta_R^c\\ \eta_L^c + \eta_R\end{pmatrix},\end{aligned} \tag{3.2}$$

Note that, the mass spliting between them is $\delta = 2m_D$, which is very small as $m_D \ll m_M$. The small m_D also make sure that the couplings of ϕ' to $\eta_{1,2}$ are proportional to the mass $m_{1,2}$. The lighter one of the two, η_1 is the dark matter candidate in our model.

The low energy effective Lagrangian, below the SM scale for the physical fermions is given as follows,

$$\begin{aligned}\mathcal{L} &= -m_u\bar{u}_L u_R - m_d\bar{d}_L d_R - m_{\nu D}\bar{\nu}_L\nu_R - m_\mu\bar{\mu}_L\mu_R - \frac{1}{2}m_1\bar{\eta}_1\eta_1 - \frac{1}{2}m_2\bar{\eta}_2\eta_2\\ &\quad -\frac{m_u}{V\sqrt{2}}\bar{u}_L u_R\phi' - \frac{m_d}{V\sqrt{2}}\bar{d}_L d_R\phi' - \frac{m_{\nu D}}{V\sqrt{2}}\bar{\nu}_L\nu_R\phi' - \frac{m_\mu}{V\sqrt{2}}\bar{\mu}_L\mu_R\phi'\\ &\quad -\frac{1}{2\sqrt{2}}\frac{m_1}{V}\bar{\eta}_1\eta_1\phi' - \frac{1}{2\sqrt{2}}\frac{m_2}{V}\bar{\eta}_2\eta_2\phi' + H.c.,\end{aligned} \tag{3.3}$$

The neutrino mass matrix for $\nu_{L,R}$ contains a Dirac mass term, m_{ν_D}, which is proportional to V, and contains a Majorana mass for ν_R which is proportional to V^2/Λ, where Λ is some high-energy scale. We expect the Majorana mass to be less than V. The diagonalization of the squared mass matrix gives two mass eigenstates, ν_A and ν_S. We will assume small mixing between them such that the active neutrino ν_A is mostly ν_L, with only a small mixing of ν_R.

The new gauge sector interactions can be explored by defining the covariant derivative as,

$$D_\mu I = \partial_\mu I + i\frac{g}{2}\tau_a W_{\mu a} + ig' Y B_\mu + i\frac{g_{T_{3R}}}{2}Q_{T_{3R}}A'_\mu. \tag{3.4}$$

where g, g' and g_{T3R} are the coupling constant corresponding to the $SU(2)_L$, $U(1)_Y$ and $U(1)_{T3R}$ groups respectively. W_μ, B_μ and A'_μ are the gauge bosons of the $SU(2)_L$, $U(1)_Y$ and $U(1)_{T3R}$

groups respectively. The mass of the dark photon, A', comes from $|D_\mu\phi|^2$ as $m^2_{A'} = 2g^2_{T3R}V^2$. The interactions of the gauge boson A' with the fermions and dark Higgs are then given by,

$$\begin{aligned}\mathcal{L}_{\text{gauge}} &= \frac{m_{A'}}{4\sqrt{2}V}A'_\mu(\bar{\eta}_1\gamma^\mu\eta_2 - \bar{\eta}_2\gamma^\mu\eta_1) + \frac{m^2_{A'}}{V\sqrt{2}}\phi' A'_\mu A'^\mu + \frac{m^2_{A'}}{4V^2}\phi'\phi' A'_\mu A'^\mu \\ &\quad -\frac{m_{A'}}{2\sqrt{2}V}j^\mu_{A'}A'_\mu. \end{aligned} \tag{3.5}$$

where the interaction current for the SM fermions is defined as, $j^\mu_{A'} = \sum_f Q^f_{T_{3R}}\bar{f}\gamma^\mu\left(\frac{1+\gamma_5}{2}\right)f$. Note that the η fields have only off-diagonal vector interaction with A'.

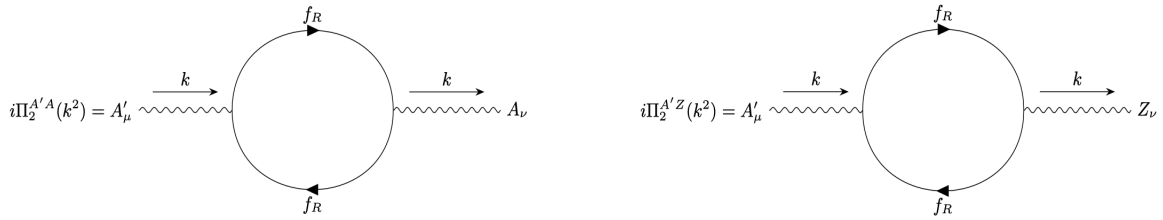

(a) **(b)**

Figure 3.1: The one loop diagrams that give rise to the kinetic mixing parameters.

In addition to the interactions given in Eq. 3.5, the A' has vector couplings to all other SM fermions, with couplings given as , ϵe, where ϵ is a kinetic mixing parameter. The kinetic mixing can arise from one loop diagrams shown in Fig. 3.1, where the right handed fermions charged under $U(1)_{T3R}$ run inside the loop.

Note that, all the SM fermion masses, dark matter masses, the dark photon and the dark Higgs masses are proportional to the symmetry breaking scale V and therefore their masses should be less than V. A suitable choice to consider is, $V = \mathcal{O}(1)$ GeV, which would naturally give rise to sub GeV masses for all the particles with $\mathcal{O}(1)$ couplings, but would be ruled out by the current data. A more suitable choice is $V = 10$ GeV, leading to couplings which are moderately smaller than $\mathcal{O}(1)$.

3.1.1 A' decays

The tree-level coupling strength of the dark photon to the right handed SM fermions are given as,

$$g_{T3R} = \frac{m_{A'}}{\sqrt{2}V}. \tag{3.6}$$

where the symmetry breaking scale V can be treated as a free parameter. We show the relation between g_{T3R} and $m_{A'}$ for various choices of V in Fig. 3.2. The dark photon has vector coupling to the other SM fermions with coupling strenght given by ϵe, where $\epsilon = g_{T3R}\sqrt{\alpha_{em}/4\pi^3}$. We consider the kintic mixing paramter, ϵ as a free parameter in our study.

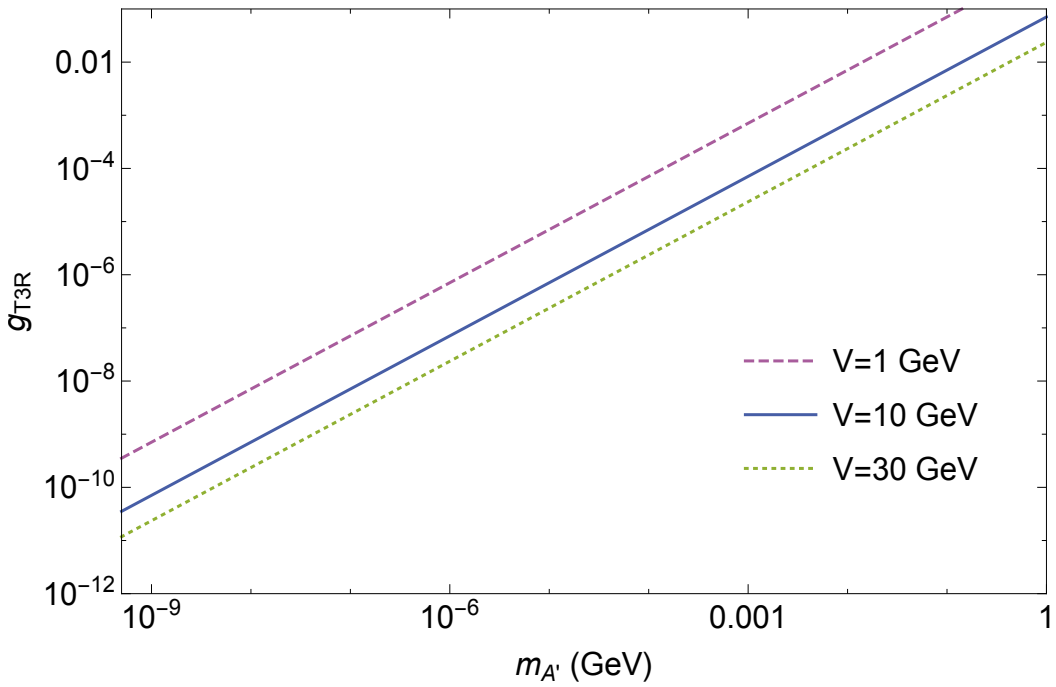

Figure 3.2: The relation between the coupling constant g_{T3R} of $U(1)_{T3R}$ and the gauge boson mass $m_{A'}$ is shown for three different values of $V = 1, 10, 30$ GeV. For phenomenological study we choose the value $V = 10$ GeV in rest of the chapter.

To avoid the bounds from BaBar [6, 7], we take $m_{A'} \leq 2m_\mu$, therefore the possible final

states of A' decays are $\eta_{1,2}\eta_{2,1}$, $\nu\nu$, and e^+e^-, of which only the last one is visible. If $m_{A'} < 2m_e$, then there is no visible decay channel as the decay $A' \to \gamma\gamma$ is forbidden by the Landau-Yang theorem [195, 196]. In thta case, if either the $\eta_1\eta_2$ or $\nu_S\nu_S$ final states are kinematically allowed, then those tree-level decays will dominate the branching fraction. But if neither of them are kinematically allowed, then the possible final states are $\nu_S\nu_A$, $\nu_A\nu_A$ but they are suppressed by the neutrino mixing angle. The expressions for the related decay widths are,

$$\begin{aligned}
\Gamma^{A'}_{\eta_1\eta_2} &= \frac{m^3_{A'}}{96\pi V^2}\left(1-\frac{4m^2_\eta}{m^2_{A'}}\right)^{1/2}\left(1+\frac{2m^2_\eta}{m^2_{A'}}\right), \\
\Gamma^{A'}_{\nu_S\nu_S} &= \frac{m^3_{A'}}{12\pi V^2}\left(1-\frac{4m^2_{\nu_S}}{m^2_{A'}}\right)^{3/2}, \\
\Gamma^{A'}_{e^+e^-} &= \frac{\epsilon^2\alpha_{em}m_{A'}}{3}\left(1-\frac{4m^2_e}{m^2_{A'}}\right)^{1/2}\left(1+\frac{2m^2_e}{m^2_{A'}}\right).
\end{aligned} \tag{3.7}$$

3.1.2 ϕ' decays

The ϕ' can decay to visible final states such as $\mu^+\mu^-$ and $\gamma\gamma$, which is via one loop, and the invisible mode such as $\eta\eta$, $\nu\nu$, $A'A'$. Note that, decays to ν_S or A' can also produce visible energy, if those states in eventually decay to SM particles. If $m_{\phi'} > 2m_\pi$ then tree-level decays to hadronic states are also possible, but the corresponding branching fraction is negligible compared to $\mu^+\mu^-$, because the coupling to first-generation quarks is so small. Also, if $m_{\phi'} > 2m_{A'}$, then ϕ' can decay promptly to A' and if this decay channel is dominant, then ϕ' production in a beam experiment is

essentially same as A' production. The related expressions for the decay widths are given by,

$$\begin{aligned}
\Gamma^{\phi'}_{A'A'} &= \frac{m^3_{\phi'}}{128\pi V^2}\left(1-\frac{4m^2_{A'}}{m^2_{\phi'}}\right)^{1/2}\left(1+12\frac{m^4_{A'}}{m^4_{\phi'}}-4\frac{m^2_{A'}}{m^2_{\phi'}}\right), \\
\Gamma^{\phi'}_{\mu^+\mu^-} &= \frac{m^2_{\mu}m_{\phi'}}{16\pi V^2}\left(1-\frac{4m^2_{\mu}}{m^2_{\phi'}}\right)^{3/2}, \\
\Gamma^{\phi'}_{\eta_i\eta_i} &= \frac{m^2_{\eta_i}m_{\phi'}}{32\pi V^2}\left(1-\frac{4m^2_{\eta_i}}{m^2_{\phi'}}\right)^{3/2}, \\
\Gamma^{\phi'}_{\nu_S\nu_A} &= \frac{m^2_{\nu_D}m_{\phi'}}{16\pi V^2}\left(1-\frac{m^2_{\nu_S}}{m^2_{\phi'}}\right)^{2}, \\
\Gamma^{\phi'}_{\gamma\gamma} &= \frac{\alpha^2_{em}m^4_{\mu}}{8\pi^3 m_{\phi'}V^2}\left[1+\left(1+\frac{4m^2_{\mu}}{m^2_{\phi'}}\right)\left(\sin^{-1}\frac{m_{\phi'}}{2m_{\mu}}\right)^2\right]^2,
\end{aligned} \tag{3.8}$$

where the decay width $\Gamma^{\phi'}_{\gamma\gamma}$ is calculated under the assumption that $m_{\phi'} < 2m_{\mu}$, otherwise, this decay is negligible compared to the $\mu^+\mu^-$ channel. ϕ' will always decay very promptly.

3.1.3 ν_S decays

If the mass of the sterile neutrino is greater than $2m_{\mu}$ then it will decay rapidly via the process $\nu_S \to \mu^+\mu^-\nu_A$, at tree level. On the other hand, if $m_{\nu_S} < 2m_{\mu}$, the sterile neutrino ν_S can decay via the process $\nu_S \to \nu_A\gamma\gamma$, with a rate

$$\Gamma_{\nu_S} \propto \alpha^2_{em}\frac{m^7_{\nu_S}m^2_{\nu_D}}{m^4_{\phi'}V^4}. \tag{3.9}$$

We estimate the lifetime as $\tau_{\nu_S} \sim \mathcal{O}(10^{13})$ sec for $V = 10$ GeV, $m_{\phi'} \sim 100$ MeV, $m_{\nu_S} = 10$ MeV, $m_{\nu_D} = 10^{-3}$ MeV. Therefore they can be considered as stable particles for the Laboratory experiments. Another possible decay channel is $\nu_S \to \nu_A\gamma$, through a transition dipole interaction, but this process arises at two loop level and is therefore highly suppressed.

3.1.4 Longitudinal polarization of A'

As $U(1)_{T3R}$ has chiral couplings to the fermions, the tree level production cross section of the longitudinal mode of A' can be enhanced. Therefore we can get qualitatively new constraints for $U(1)_{T3R}$ compared to other well studied $U(1)$ gauge groups such as such as $U(1)_{B-L}$, $U(1)_{L_i-L_j}$, $U(1)_X$ [197, 198, 199, 200, 201]. Note that the enhancement entirely comes from the axial part of the chiral interactions. The pure vector part of the interactions vanishes identically for the longitudinal mode, by Ward identity. Therefore the A' production cross section is only enhanced if the A' is produced at tree-level. If A' is produced through kinetic mixing, then the contribution from longitudinal polarization will again vanish identically due to the Ward Identity as this is pure vector interaction.

The longitudinal polarization vector is proportional to $E_{A'}/g_{T3R}V$ and this yields an enhancement to the matrix element for the production of the longitudinal mode at high-boost. The matrix element for such processes is similar to that for production of the Goldstone boson of $U(1)_{T3R}$ symmetry-breaking, with a coupling to fermions which goes as $m_f/\sqrt{2}V$, according to the Goldstone Equivalence theorem. For small $m_{A'}$ limit, the coupling of a SM fermion to the longitudinal polarization mode is enhanced with respect to the transverse polarization modes by a factor $m_f/m_{A'}$. But note that, this enhancement is restricted by perturbative unitarity, so can not be arbitrarily large. Our scenario is perturbative as we have $m_f < V = 10$ GeV.

As the production cross section of the longitudinal mode of A' can be approximated as the production corss section of a pseudo scalar with couplings proportional to $m_f/\sqrt{2}V$, one can see that the most dramatic effect will be on production of the A' through a coupling to muons as the coupling to $u-/d-$quarks is suppressed by close to two orders of magnitude, compared to the coupling to muons. Therefore the enhancement in the production will affect the cosmological production (via $\mu^+\mu^- \to \gamma A'$), production in supernovae (which have non-negligible muon content), and from future experiments involving the invisible decays of light A' coupling directly to muons, such as NA64μ and LDMX-M[3].

3.1.5 UV completion

All the fermion mass terms were generated from a non-renormalizable low energy effective lagrangian defined below the scale of electroweak symmetry breaking, of the form $(1/\Lambda)H\phi\bar{f}f$ due to the $U(1)_{T3R}$ assignments. Therefore there should be some UV completion of the model. One such possibility is the universal seesaw mechanism [202, 203, 204, 205, 206, 207, 208, 209]. We add a set of heavy fermions $\chi_{u,d,\mu,\nu}$ which are singlets under $SU(2)_L$ and $U(1)_{T3R}$, and have same quantum numbers under $SU(3)_C$ and $U(1)_Y$ as u, d, μ and ν, respectively. They mix with the fermions charged under $U(1)_{T3R}$, generating the mass terms and couplings of the light fermions through a high-scale seesaw mechanism. We summarize all the particles in Table. 3.2.

Particle	$SU(3)_C \times SU(2)_L \times U(1)_Y \times U(1)_{T3R}$
χ_{uL}	$(3, 1, 2/3, 0)$
χ_{dL}	$(3, 1, -1/3, 0)$
$\chi_{\mu L}$	$(1, 1, -1, 0)$
$\chi_{\nu L}$	$(1, 1, 0, 0)$
χ^c_{uR}	$(3, 1, -2/3, 0)$
χ^c_{dR}	$(3, 1, 1/3, 0)$
$\chi^c_{\mu R}$	$(1, 1, 1, 0)$
$\chi^c_{\nu R}$	$(1, 1, 0, 0)$
q_L	$(3, 2, 1/6, 0)$
u^c_R	$(3, 1, -2/3, -2)$
d^c_R	$(3, 1, 1/3, 2)$
l_L	$(1, 2, -1/2, 0)$
μ^c_R	$(1, 1, 1, 2)$
ν^c_R	$(1, 1, 0, -2)$
η_L	$(1, 1, 0, 1)$
η^c_R	$(1, 1, 0, -1)$
H	$(1, 2, 1/2, 0)$
ϕ	$(1, 1, 0, 2)$

Table 3.2: The charges of the fields under the gauge groups of the model. For the fermionic fields, we have shown the charges of the left-handed component of each Weyl spinor.

The renormalizable Lagrangian of the UV complete model at high scale can be written as,

$$\begin{aligned}
-\mathcal{L}_{\rm Y} &= \lambda_{Lu}\bar{q}'_L\chi'_{uR}\tilde{H} + \lambda_{Ld}\bar{q}'_L\chi'_{dR}H + \lambda_{L\nu}\bar{l}'_L\chi'_{\nu R}\tilde{H} + \lambda_{Ll}\bar{l}'_L\chi'_{\mu R}H \\
&+\lambda_{Ru}\bar{\chi}'_{uL}u'_R\phi^* + \lambda_{Rd}\bar{\chi}'_{dL}d'_R\phi + \lambda_{R\nu}\bar{\chi}'_{\nu L}\nu'_R\phi^* + \lambda_{Rl}\bar{\chi}'_{\mu L}\mu'_R\phi \\
&+m_{\chi_u}\bar{\chi}'_{uL}\chi_{uR} + m_{\chi_d}\bar{\chi}'_{dL}\chi_{dR} + m_{\chi_\nu}\bar{\chi}'_{\nu L}\chi_{\nu R} + m_{\chi_\mu}\bar{\chi}'_{\mu L}\chi_{\mu R} \\
&+m_D\bar{\eta}_R\eta_L + \frac{1}{2}\lambda_{\eta L}\bar{\eta}^c_L\eta_L\phi + \frac{1}{2}\lambda_{\eta R}\bar{\eta}^c_R\eta_R\phi^* + H.c.\,, \qquad (3.10)
\end{aligned}$$

the fermionic mass matrix in the flavor basis is given by,

$$M_f = \begin{pmatrix} 0 & \frac{\lambda_{Lf}v}{\sqrt{2}} \\ \lambda_{Rf}V & m_{\chi'_f} \end{pmatrix}. \qquad (3.11)$$

We diagonalize the above mass matrix using the seesaw mechanism, which gives two mass eigenstates, the lightest one is the SM fermion while the heavier one is the physical vector-like fermion. The mass term for the SM fermion is given by,

$$m_f = \frac{\lambda_{Lf}\lambda_{Rf}vV}{\sqrt{2}m_{\chi'_f}}, \qquad (3.12)$$

and the physical vector-like fermion mass is

$$m_{\chi_f} \simeq m_{\chi'_f}. \qquad (3.13)$$

The physical mass eigenstates can be expressed in terms of the flavor state as follows,

$$\begin{pmatrix} f_{L,R} \\ \chi_{f_{L,R}} \end{pmatrix} = \begin{pmatrix} \cos\theta_{f_{L,R}} & \sin\theta_{f_{L,R}} \\ -\sin\theta_{f_{L,R}} & \cos\theta_{f_{L,R}} \end{pmatrix} \begin{pmatrix} f'_{L,R} \\ \chi_{f'_{L,R}} \end{pmatrix}, \qquad (3.14)$$

where $\theta_{f_{L,R}}$ are the mixing angles. In the high-scale seesaw limit, $m_{\chi_f} \gg \lambda_{Lf} v/2$ we get,

$$\theta_{f_L} \simeq \tan^{-1}\left[\frac{\lambda_{Lf} v}{\sqrt{2} m_{\chi_f}}\right], \tag{3.15}$$

and if $m_{\chi_f} \gg \lambda_{Rf} V$ then,

$$\theta_{f_R} \simeq \tan^{-1}\left[\frac{\lambda_{Rf} V}{m_{\chi_f}}\right]. \tag{3.16}$$

Note also that the neutrino mass matrix is more complicated 3×3 matrix since they can also get Majorana maases as both ν'_R and χ'_ν are uncharged under the unbroken SM gauge groups.

3.2 Constraints

In this section, we discuss various constraints for our model. The parameter space of our model is tightly constrained by the current experimental bounds. But we have enough open parameter space. Some of these open parameter space can be probed by future/upcoming experiments. Still there is a small allowed region which even these upcoming experiments can not probe. We briefly discuss our strategies for using the new datasets to probe the scenario. We broadly divide the constraints in few categories and discuss them separately.

3.2.1 Corrections to $g-2$

There is a long standing 3.7σ tension between the theoretical predictions [210, 211, 212, 213, 100, 101, 102, 214, 215, 103, 216, 217, 218, 219, 220, 221, 222, 223, 224, 109, 225, 226] and the experimental results [36]. Recent data from Fermilab [189] combined with the BNL data [36] increased the tension to to 4.2 σ level. This is given by,

$$\Delta a_\mu = a_\mu^{\text{exp}} - a_\mu^{\text{th}} = (2.52 \pm 0.59) \times 10^{-9} \tag{3.17}$$

The muon anomalous magnetic moment receives corrections from one loop diagrams in which either ϕ' or A' run in the loop as shown in Fig. 3.3. The correction to $a_\mu = (g_\mu - 2)/2$ due to

one-loop diagrams involving A' and ϕ' is given by [131]

$$\Delta a_\mu = \frac{m_\mu^4}{16\pi^2 V^2}\int_0^1 dx \frac{(1-x)^2(1+x)}{(1-x)^2 m_\mu^2 + x m_{\phi'}^2} + \frac{m_\mu^2}{32\pi^2 V^2}\int_0^1 dx \frac{2x(1-x)(x-2)m_{A'}^2 - 2x^3 m_\mu^2}{x^2 m_\mu^2 + (1-x)m_{A'}^2}. \tag{3.18}$$

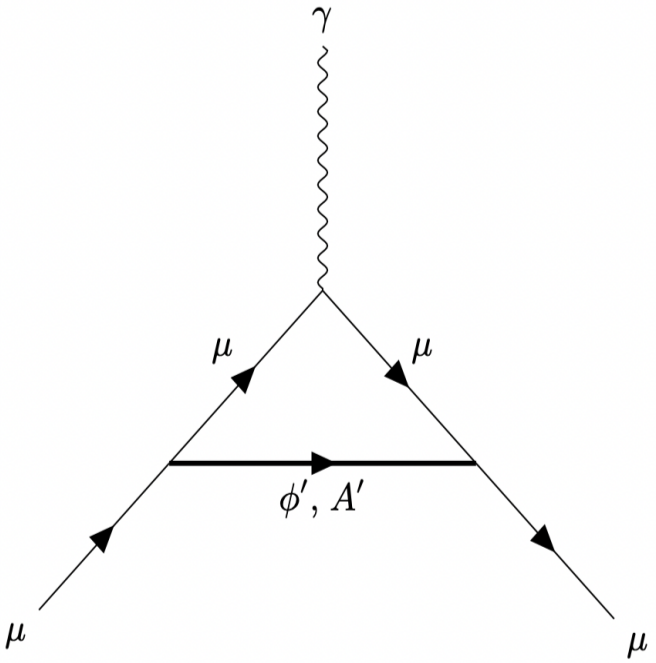

Figure 3.3: One-loop Feynman diagrams mediated through ϕ'/A' that contribute to g_μ-2.

Note that, the contribution to $g_\mu - 2$ from ϕ' mediated diagram is always positive, while the contribution from A' mediated diagram is always negative, as the A' has both vector and axial couplings to the muon. These contributions must cancel each other to within $\mathcal{O}(1\%)$ in order for the total correction to $g_\mu - 2$ to be consistent with experimental result. There is a region of parameter space where we can achieve this cancellation. The contributions from the A' mediated is almost constant while ϕ' mediated diagram depends on the ϕ' mass. We find a narrow band in the $m_{\phi'}$ parameter between 70-80 MeV, where this cancellation happens. We show this region of parameter space in Fig. 3.6 along with other bounds.

3.2.2 Cosmological and Astrophysical Constraints

We summarize the various constraints on our model arising from the cosmological and astrophysical observations. As mentioned in the previous , due to the chiral nature of A' couplings, the tree level production cross section of the longitudinal mode of A' gets an enhancement. This affect the cosmological production of A' in the early Universe. On can not go to the arbitrarily small coupling limit to avoid the constraints arising from the cosmological observations. This leads to tight constraints from CMB measurements [32]. If we assume that the Universe reheats to a temperature ≥ 100 MeV, then region of parameter space given by $m_{A'} < 1$ MeV for $V \sim \mathcal{O}(10)$ GeV are ruled out, as they would lead to a number of effective neutrinos (N_{eff}) [1] which is inconsistent with CMB measurements [32]. Note that, this bound can be circumvented if the Universe reheats to a lower temperature.

Bounds on supernovae cooling [4, 5] can also restrict the parameter space. This is also impacted by the enhancement in the tree level production cross section of the longitudinal mode of A'. The temperature of supernovae is large enough that a non-negligible population of muons is produced, and they couple to ϕ' and A' at tree level, which decay to invisible final states, then there will be an anomalous rate of supernova cooling which is ruled out by observations of SN1987A. These supernova cooling bounds would also rule out $m_{\phi'} \leq 200$ MeV if the decays $\phi' \to \eta\eta, \nu_S\nu_S$ are kinematically allowed. White dwarf (WD) cooling constraints can be neglected if $m_\eta, m_{\nu_s} \geq 0.1$ MeV, as in this case they will be in equilibrium with the plasmons inside the WD and can not escape. The other possible final states e^+e^- and $\nu_A\nu_A$ are either not allowed kinematically or mixing angle suppressed [227]. We also show related bounds from solar cooling [2, 3] and cooling of stars in Globular clusters [2].

We show all the bounds arising from the above cosmological and astrophysical observations in Fig. 3.4 on the $(m_{A'}, m_{\phi'})$ parameter space, in the case where A' and ϕ' decay invisibly. Note that, all the astrophysical bounds can be evaded by assuming dark photon to be chameleon-type field with its mass depending on the environmental matter density [228, 229, 230, 2].

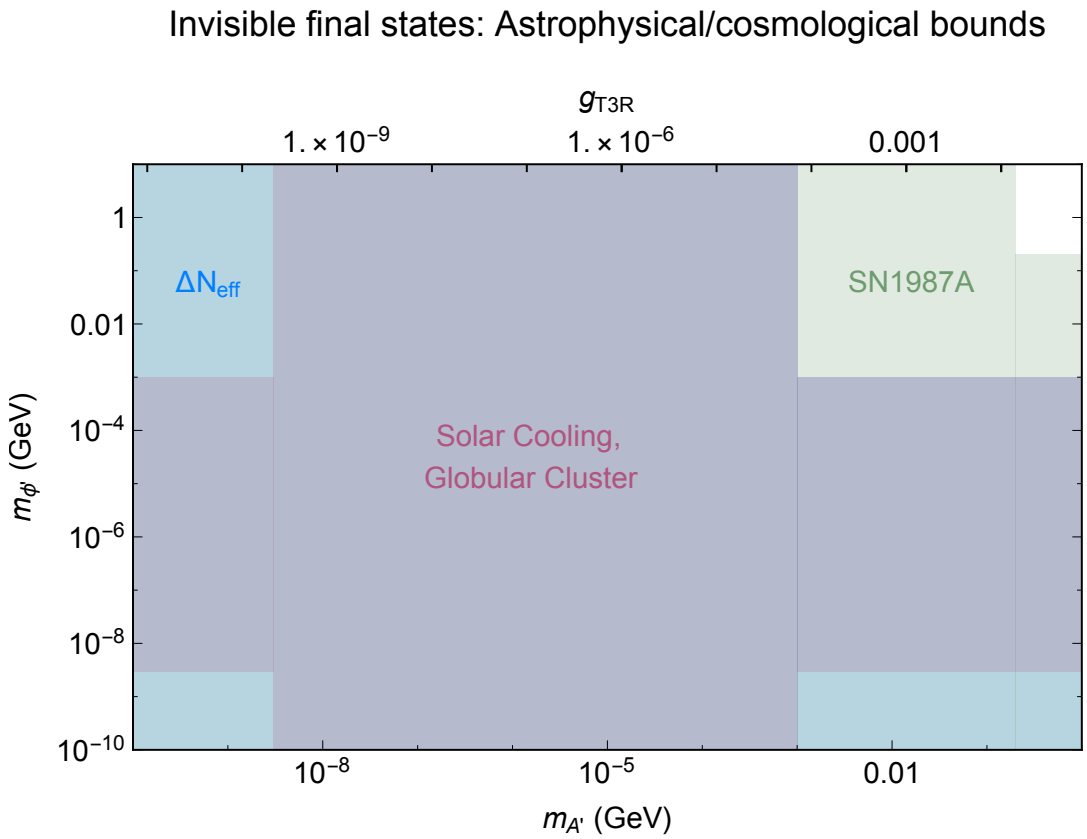

Figure 3.4: Bounds from cosmological and astrophysical observables, where we assume that the A' and ϕ' decay to invisible states: constraints on ΔN_{eff} (green region) [1], on excess cooling of stars [2, 3] and globular clusters (gray region) [2], and excess cooling of supernovae (light green region) [4, 5].

3.2.3 Visible Decays at Displaced Detectors

One important strategy to probe the new light mediators is to produce them at a proton collider, fixed-target, or beam dump experiment and searching for visible decays of this mediator at a distant detector. The light mediators have to be long-lived enough and decay to visible final states to be detected by these detectors. The ϕ' of our model, which decays rapidly hence has a short lifetime, can not produce an appreciable number of particles to reach the detector. Therefore they can not be searched for in these displaced detectors. However, if A' dominantly decays e^+e^- through kinetic mixing, then the decay length may be long enough for the decay to occur within the detector.

The dominant production mechanism of A' are p-bremsstrahlung and meson decay, where

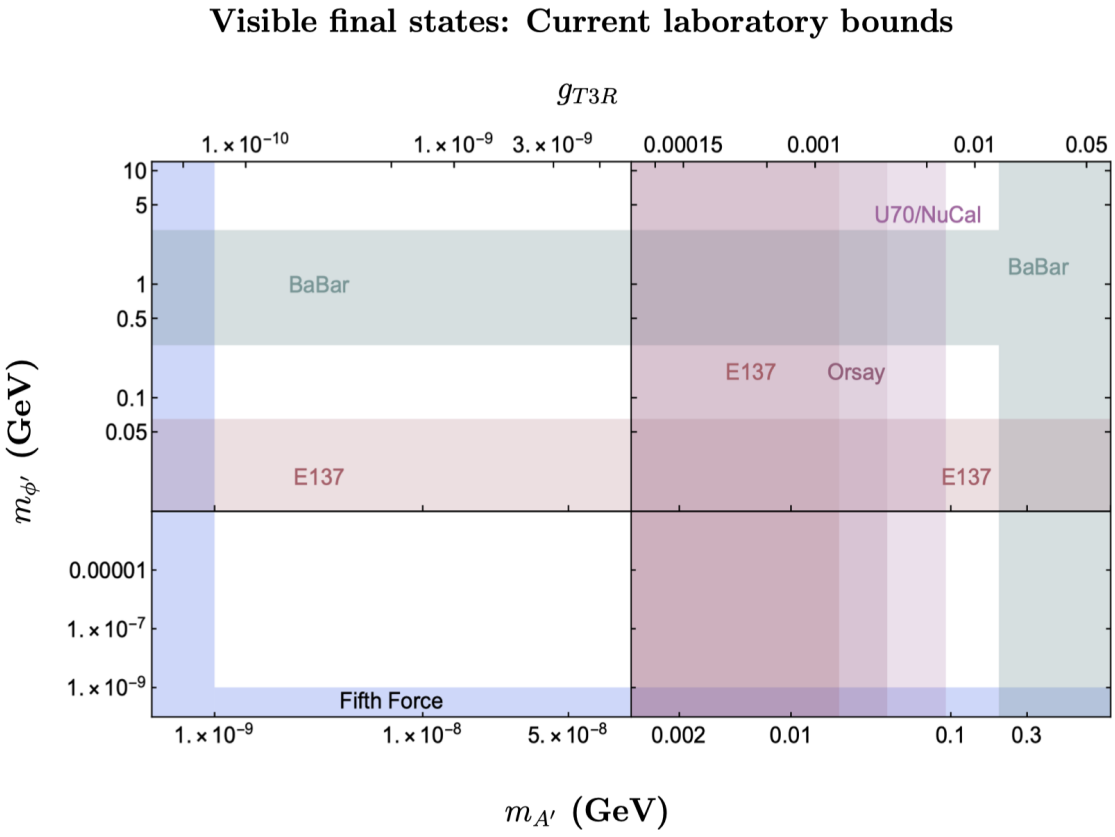

Figure 3.5: Shaded regions represent excluded region of parameter space by current laboratory experiments, assuming that A' and ϕ' decay dominantly to SM particles: BaBar [6, 7, 8], E137 [9, 10, 11], Orsay [12, 8], U70/NuCal [13, 12, 8] and from fifth force experiments [14, 2].

the A' couples at tree-level to u- and d-quarks. Note that, visible decays are only possible for $m_{A'} > 1$ MeV, the enhancement to the production rate of the longitudinal polarization is minimal and can be neglected. Though the production is at tree level, A' decays at one-loop through kinetic mixing. Therefore the allowed parameter space of our model can be estimated by considering the estimated sensitivity of these experiments to models where A' only couples to the SM via kinetic mixing, but with the number of events enhanced by the factor $(\pi/\alpha_{em} f)^2$, to account for the fact that A' production is a tree-level process, where, f is the factor by which the kinetic mixing parameter exceeds that obtained only from one-loop diagrams with SM fermions in the loop.

The sensitivity curve of these experiments have a ceiling, above which the A' decays too rapidly to reach the detectors, and a floor, below which the coupling is too weak for enough A' to be pro-

duced. To get visible decays of A', we must have $m_{A'} > 1$ MeV; taking $V = 10$ GeV, we find that we must have $g_{T3R} \geq 10^{-4}$. We also assume that kinetic mixing is generated at one-loop only by SM fermions (that is, $f = 1$). The parameter space of our model is constrained by the experiments such as, E137 [9, 10, 11], Orsay [12, 8], U70/NuCal [13, 12, 8]. Future/upcoming experiments such as FASER, FASER-2 [231, 232, 233, 234, 15], SHiP [235, 236] and SeaQuest [16, 237] can project bounds on the parameter space. Electron beam dump experiments can also put constraints on our model [238], where one-loop processes can result in the production of either A' (kinetic-mixing) or ϕ' (Primakoff production), with subsequent one-loop decays to SM particles at a displaced detector. In particular, BaBar [6, 7] provides tight constraints on the regions of parameter space where $e^+e^- \to \mu^+\mu^-(A', \phi' \to \mu^+\mu^-)$ is kinematically accessible. We also consider the bounds coming from the fifth force searches experiments, [14]. They can put tight constraints in the regions of parameter space where ϕ' or A' are extremely light.

We show all the constraints on our model in the $(m_{A'}, m_{\phi'})$-plane in Fig. 3.5, coming from the existing experimental data assuming that A', ϕ' predominantly decay to SM particles. In Fig. 3.6, we show the projections on the parameter space from the upcoming experiments in the region of parameter space allowed by all the current experiments.

3.2.4 Visible and Invisible Decays at Nearby Detectors

In this subsection, we consider the bounds coming from the experiments with nearby detectors. If A' predominantly decays to invisible final states, then the Crystal Barrel (CB) [22, 23] detector can give constraints on $m_{A'}$ from the measurements of the branching ration of the process, $\pi^0 \to \gamma A'$. The bounds on this branching ratio from CB is [22, 23],

$$\text{Br}(\pi^0 \to \gamma A') \leq 2.8 \times 10^{-4}, \qquad m_{A'} \leq 65 \text{ MeV}, \tag{3.19}$$

and,

$$\text{Br}(\pi^0 \to \gamma A') \leq 6.0 \times 10^{-5}, \qquad 65 \text{ MeV} \leq m_{A'} \leq 125 \text{ MeV}, \tag{3.20}$$

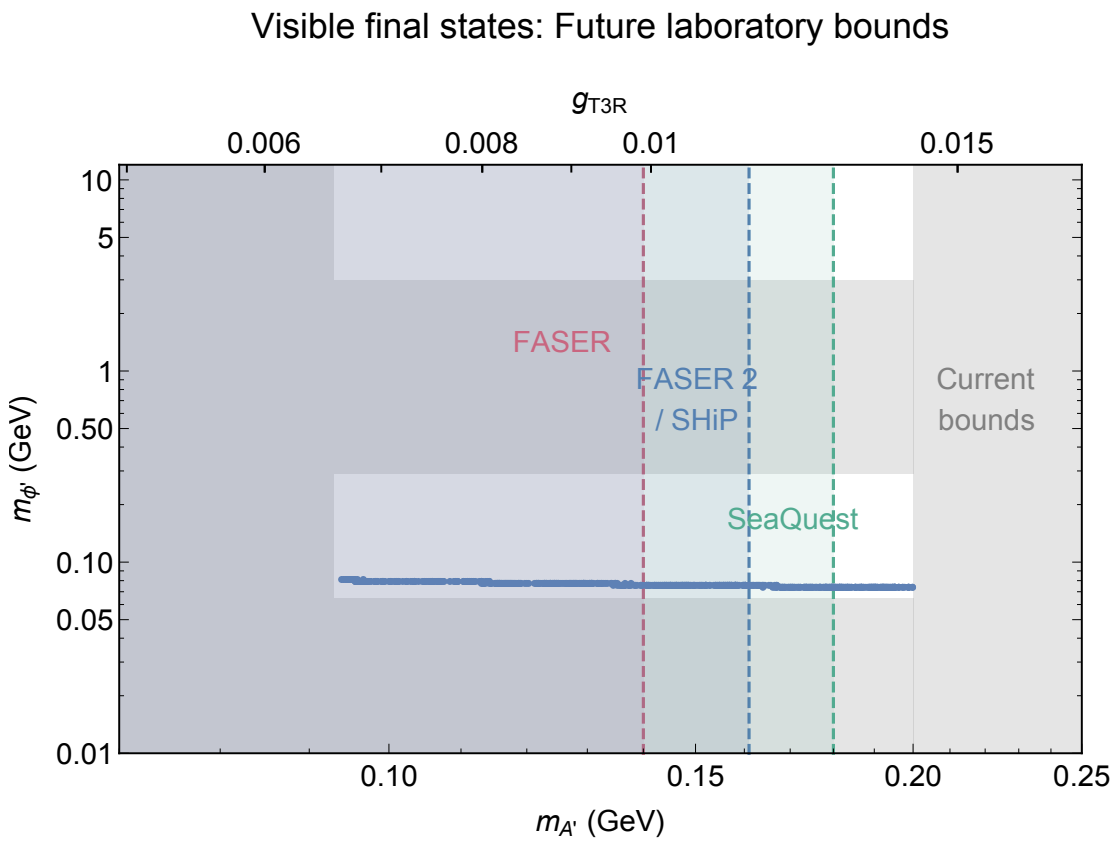

Figure 3.6: Shown are the sensitivities of upcoming laboratory experiments assuming A', ϕ' decay visibly at displaced detectors: FASER [15] (purple region), FASER 2/SHiP [15] (dark green region), and SeaQuest [16] (light green region). The constraints from current laboratory experiments are shown by light gray region, reproduced from Fig. 3.5. The blue band shows the region of parameter space where the $g_\mu - 2$ is consistent with the recent observations.

The expression for this branching fraction for our model is given by

$$\text{Br}(\pi^0 \to \gamma A') = \frac{m_{A'}^2}{4\pi\alpha V^2}\left(1 - \frac{m_{A'}^2}{m_{\pi^0}^2}\right)^3 \tag{3.21}$$

Therefore the region of paramter space, 55 MeV $< m_{A'} < 120$ MeV is ruled out by CB.

The other experiments we considered are the Proposed detectors such as NA64μ [24, 25] and LDMX-M^3 [26, 27] (a proposed muon beam version of LDMX [239]) that can probe this scenario in the case where either A' or ϕ' has a significant decay rate to invisible states. In the NA64μ experiment a muon beam will be collided with a target, and interactions with missing energy will

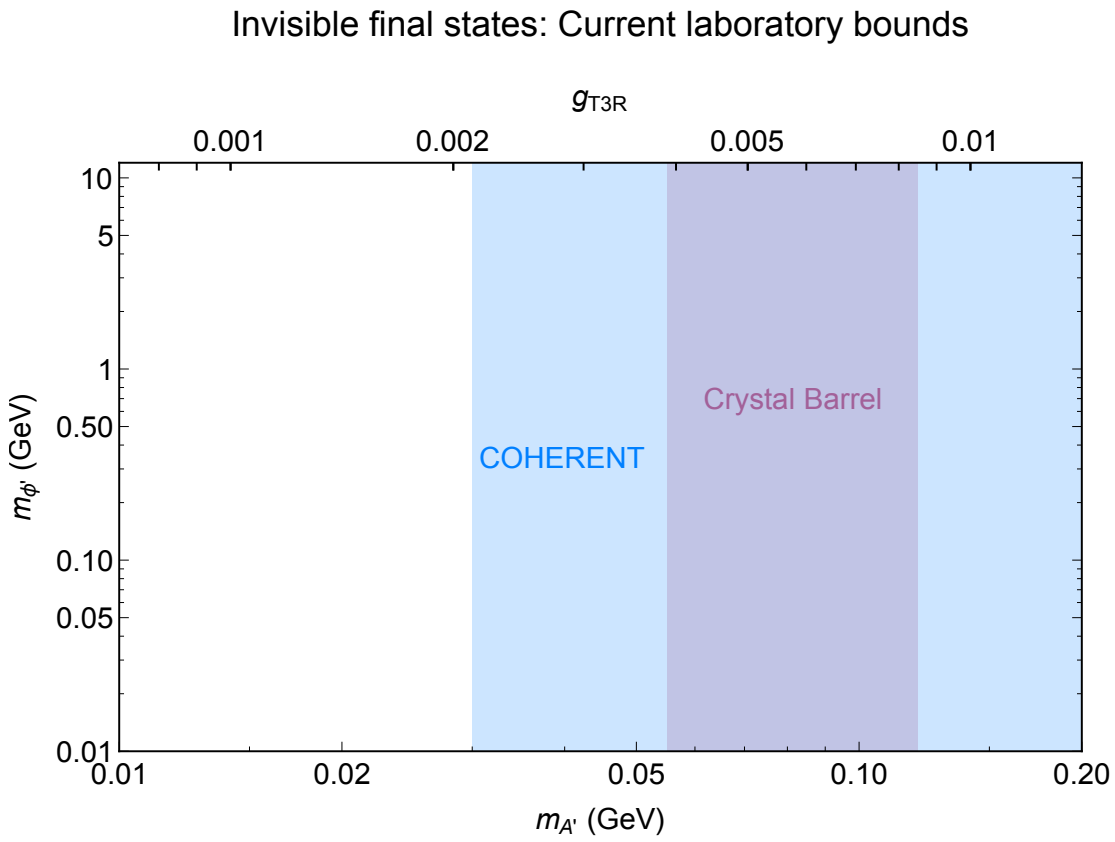

Figure 3.7: Shaded regions represent excluded region of parameter space by current laboratory experiments, assuming that A' and ϕ' decay dominantly to invisible particles: included are bounds from COHERENT [17, 18, 19, 20, 21](light blue) and Crystal Barrels [22, 23] (light purple) experiments.

be searched for. The LDMX-M^3 will also be a similar type experiment. Both of them can probe the $m_{\phi'}$ parameter space if ϕ' decays dominantly to invisible final states. NA64μ can probe muon-scalar couplings $\sim \mathcal{O}(10^{-5})$, largely independent of the scalar mass [24]. The coupling of ϕ' to muons is $\mathcal{O}(10^{-2})$ in our model, implying that this scenario can be probed by NA64μ for any $m_{\phi'}$, provided the branching fraction to invisible states is $Br(invisible) > 10^{-6}$. In a similar way, LDMX-M^3 Phase 1 will probe any $m_{\phi'}$, provided $Br(invisible) > 10^{-4}$, while Phase 2 will have a greater sensitivity than NA64μ [27].

In our model, the decay $\phi' \to \gamma\gamma$ is one-loop suppressed, whereas the decays $\phi' \to \nu_S\nu_A, \eta\eta$ occur at tree-level.Therefore the invisible decays will dominate if kinematically allowed. Even if the decay $\phi' \to \mu^+\mu^-$ is kinematically allowed, the invisible decays will still have a branching

fraction of at least $\mathcal{O}(10^{-4})$, provided $m_{\eta,\nu_S} > 1$ MeV which is enough to be probed at these experiments. The sensitivity to $m_{A'}$ parameter space is roughly similar for both NA64μ and LDMX-M^3. Even arbitrarily light A' can not escape these search as the longitudinal mode couples to muons approximately the same as a pseudoscalar with coupling $\sim \mathcal{O}(10^{-2})$. Therefore, NA64$\mu$ and LDMX-M^3 will be able to probe the entire parameter space, provided $m_{A',\phi'} > 2m_\eta$ or $2\nu_S$. Even if the $\eta\eta$ and $\nu_S\nu_S$ final states are not kinematically allowed for A' decay, and the dominant decay channel is is e^+e^- final states. NA64μ and LDMX-M^3 can still probe if the decay length of the A' is long enough that a significant number of A' leave the detector without decaying. We show the CB constraint in Fig. 3.7 and show the projected bounds of NA64μ and LDMX-M^3 in Fig. 3.8.

3.2.5 Dark Matter and Sterile Neutrino Scattering at Displaced Detectors

In this subsection we consider the neutrino experiments which can be complimentary to the beam dump experiments, as such they probe the appearance of dark matter/sterile neutrinos at the detector. There are a variety of stopped pion based experiments e.g., COHERENT [17, 18, 19, 20, 21], CCM [240, 241], JSNS^2 [242, 243, 244, 245, 246], etc that fall into this category. These experiments produce neutrinos from a proton beam hitting a target, and search for the neutral current scattering of these neutrinos at a distant detector. Among them, the ongoing COHERENT and CCM experiments are CEνNS [247, 248] experiments. A large amount of photons from proton, electron bremsstrahlung and meson decays [249] are produced in these experiments, which can then produce A'. If the decays $A' \to \eta\eta,\ \nu_S\nu_S$ are kinematically allowed, then they will occur promptly and dominate the A' branching fraction and can scatter off the nuclei of the target material, which can then be probed. However, neutrinos coming from pion and muon decays can produce background which can mimic the dark matter/sterile neutrino signlas. However one can extract the dark matter signal from the neutrino background by utilizing the pulsed nature of the beam and the timing and the energy spectra of the recoiling nucleus [250]. This idea was used in details in [249] to get bounds and we can rescale their result for our purpose.

Recently, the COHERENT experiment has observed 6.7σ evidences of CEνNS type events using CsI detector [17] while previously they found a 3.8σ excess using LAr [21] detector. Moreover,

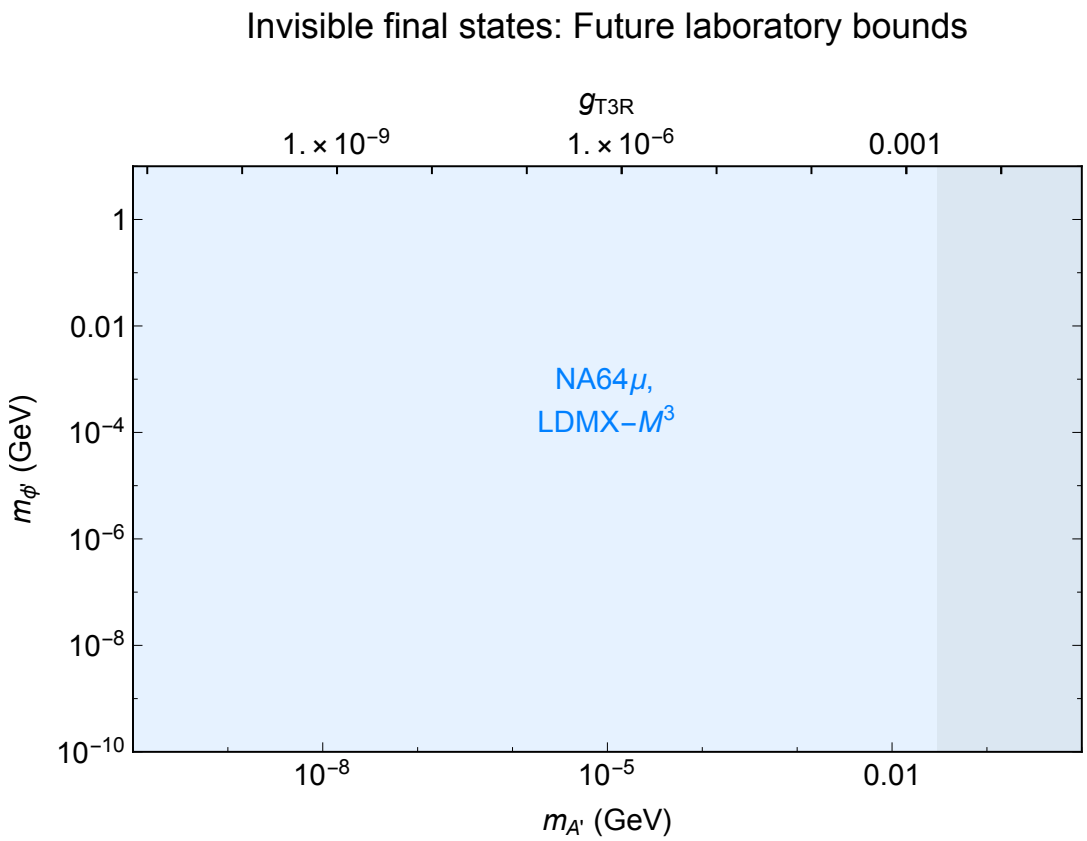

Figure 3.8: Shown are the sensitivities of upcoming laboratory experiments assuming A', ϕ' decay to invisible particles: NA64μ [24, 25], and LDMX-M^3 [26, 27] (light blue region). The constraints from current laboratory experiments are shown by light gray region, reproduced from Fig. 3.7.

the CSI-data shows some excess events at $\sim 2.4-3\sigma$ confidence level for $m_{A'} \leq 100$ MeV assuming the A' decays promptly to dark matter or sterile neutrino (in this model) [250]. We simply rescale the limits found in [249] to get the related bounds on the parameter space of our model. We also find a benchmark which can explain the excess events.

In our scenario, the A' is produced from the tree level couplings to u- or d-quarks. It then decays to $\eta\eta$ or $\nu_S\nu_S$ final states, which scatters off the nuclei of the target material by the process,$\nu_s/\eta_i + N \to \nu_s/\eta_j + N$ mediated by either A' or ϕ', and generate nuclear recoil to be detected by the detector. Therefore the event rate is proportional to g^6_{T3R}, two powers of the coupling of A' to dark matter (from the squared scattering matrix element) and four powers of the coupling of the A' to first generation quarks (two from the squared scattering matrix element, and two from the squared

A' production matrix element). To do the rescalings of the result of [249], we relate our event rate with that of [249] by assuming $m_\eta/m_{A'}, m_{\nu_S}/m_{A'} = 1/3$. If the dark matter/sterile scasttering is mediated by A', we then find that $g_{T3R} \sim 0.002$ can reproduced the COHERENT excess, following [250]. This corresponds to $m_{A'} \sim 30$ MeV for our model and interestingly this value is not ruled out by any other laboratory based experiment. The dark photon mass parameter above 30 MeV is ruled out COHERENT data. Note that, if the dark matter/sterile scattering mediates through ϕ', then we get an additional suppression factor $g_{T3R}^{-4} m_\eta^2 m_{u,d,e}^2/2V^4$. This still rules out $m_{A'} > 30$ MeV. In Fig. 3.8, we show the limits on the A' mass parameter from COHERENT together with bounds from other laboratory based experiments where the final states are dominantly invisible.

3.2.6 Non Standard Interactions for Active Neutrinos

The non-standard interactions of active neutrinos with nuclei mediated by A' and ϕ', assuming the momentum transfer to be small compared to mediators mass, can be expressed as dimension-6 effective operators as,

$$\begin{aligned} \mathcal{O}_{A'} &= \frac{\sin^2\theta}{2V^2}(\bar{\nu}_A\gamma^\mu P_L\nu_A)(\bar{q}\gamma_\mu P_R q), \\ \mathcal{O}_{\phi'} &= \frac{m_q^2\sin\theta}{2V^2 m_{\phi'}^2}(\bar{\nu}_A P_L\nu_A)(\bar{q}P_R q), \end{aligned} \tag{3.22}$$

where θ is the active-sterile neutrino mixing angle. We consider the constraints on these interactions found in [251] by considering all the NSIs from a large set at the same time. Current data bounds the coefficients of these operators to be $\leq \mathcal{O}(10^{-5})$ GeV^{-2} [251]. And the bounds on the mixing angles are,

$$\sin^\theta \leq \mathcal{O}(10^{-5}) \tag{3.23}$$

for $\mathcal{O}_{A'}$ [251]. And for $\mathcal{O}_{\phi'}$ it is [251]

$$\sin\theta \leq \left[\mathcal{O}(10^{-3})\right]\left(\frac{m_{\phi'}}{5\text{MeV}}\right)^2, \tag{3.24}$$

Future experiments such as DUNE [252, 253, 254, 255, 256, 257], Hyper-K [258, 259, 260, 261, 262, 263] etc. can probe values of the mixing angles one order of magnitude smaller.

Type of experiments	Name of the experiment	Production of A'/ϕ'	Final states	Results
Electron beam dump experiments	E137, Orsay	A' : electron bremsstrahlung through kinetic mixing at one-loop, ϕ' : Primakoff production at one-loop.	Both A', ϕ' decay predominantly to visible SM states e^+e^-. ϕ' decay is rapid.	E137 rules out : 1 MeV $\leq m_{A'}$ $\leq$ 20 MeV, 1 MeV$\leq m_{\phi'}$ $\leq$ 65 MeV. Orsay rules out : 1 MeV $\leq m_{A'}$ $\leq$ 40 MeV. U70/NuCal rules out : 1 MeV $\leq m_{A'}$ $\leq$ 93 MeV.
Proton beam dump experiments	U70/NuCal, FASER SHiP, SeaQuest (displaced detector)	p-bremsstrahlung or meson decay at tree level	$A' \to e^+e^-$ through kinetic mixing. $\phi' \to \gamma\gamma$ ϕ' decays rapidly hence cannot be probed.	FASER can probe : 1 MeV $\leq m_{A'}$ $\leq$ 140 MeV. FASER 2/SHiP can probe : 1 MeV $\leq m_{A'}$ $\leq$ 161 MeV. SeaQuest can probe : 1 MeV $\leq m_{A'}$ $\leq$ 180 MeV.
e^+e^- collider experiments	BaBar, Belle-II	$e^+e^- \to \mu^+\mu^- + A'/\phi'$, $e^+e^- \to \gamma A'$	4μ final states, γ + invisible	BaBar rules out for (4μ final states) : 200 MeV $\leq m_{A'}$ $\leq$ 1.3 GeV, 290 MeV $\leq m_{\phi'}$ $\leq$ 3 GeV. Belle-II can probe (γ + invisible): $m_{A'} \geq$ 30 MeV.
$\bar{p}p$ collider experiments	Crystal Barrel	$\bar{p}p \to \pi^0\pi^0\pi^0$, $\pi^0 \to \gamma A'$	invisible states	The parameter space is ruled out for: 55 MeV $< m_{A'}$ $<$ 120 MeV

Type of experiments	Name of the experiment	Production of A'/ϕ'	Final states	Results
Fifth force searches experiments	Precision tests of gravitational Casimir, and van der Waals forces	Relevant for extremely light A'/ϕ'. For $m_{A'} \to 0$ limit, the Longitudinal mode will contribute.	n/a	The parameter space is ruled out for: $m_{A'}/m_{\phi'} \leq 1$ eV.
Astrophysical probes	SN1987A, Cooling of Sun and globular clusters, White dwarfs	$\gamma + \mu \to A' + \mu$, $\mu + p \to \mu + p + A'$, $\mu^+\mu^- \to A'$ at tree level, $e^+e^- \to A'$ through kinetic mixing.	$A' \to \eta\eta, \nu_s\nu_s$ (if decays to $\nu\nu, e^+e^-$ then can not escape), $\phi' \to \eta\eta, \nu\nu$	SN1987A rules out : $m_{A'}, m_{\phi'}$ ≤ 200 MeV. Stellar cooling rules out: $m_{A'}, m_{\phi'}$ ≤ 1 MeV. WD constraints are negligible if m_η, m_{ν_s} ≥ 0.1 MeV.
Cosmological probes	ΔN_{eff} value	$\mu^+\mu^- \to \gamma A'$, production of longitudinal mode get enhanced due to axial vector coupling.	invisible states	If the Universe reheat at a temperature ≥ 100 MeV, $m_{A'}, m_{\phi'} \leq 1$ MeV is ruled out. (Can be evaded if reheat occurs at a lower temperature.)
Muon beam experiments	NA64μ, LDMX-M^3 (nearby detectors)	$\mu-$bremsstrahlung	Can probe when A'/ϕ' has a significant decay rate to invisible states such as $\nu\nu, \eta\eta$	NA64μ, LDMX-M^3 can probe the entire parameter space if $m_{A',\phi'} > 2m_{\eta,\nu_s}$ with Br(invisible)$> 10^{-4}$, even if $A'/\phi' \to \mu^+\mu^-$ is allowed still Br(invisible)$> 10^{-4}$ provided $m_{\eta,\nu_s} > 1$ MeV.

Type of experiments	Name of the experiment	Production of A'/ϕ'	Final states	Results
Neutrino experiments	COHERENT, CCM JSNS^2	p/e- bremsstrahlung, meson decay	$A' \to \nu_s\nu_s/\eta\eta$, $\nu_s/\eta_i + N \to \nu_s/\eta_j + N$ generate nuclear recoil, $\nu_s/\eta_i + e \to \nu_s/\eta_j + e$ generate electron recoil	Can be probed by looking at nuclear/electron recoil. $m_{A'} \sim 30$ MeV can explain the 2.4-3σ excess found by COHERENT, $m_{A'} \geq 30$ MeV is ruled out. CCM and JSNS^2 will improve the sensitivity.

Table 3.3: A summary of the various experiments/probes considered here, their methods for producing and detecting the mediating particles, and the resulting sensitivities.

3.3 Direct Detection

In this section, we discuss about the direct detection prospects of our model and where does it stand based on the current constraints. The direct detection experiments play vital roles in determining the presence of the dark matter in the Universe, where the dark matter particles hit the target material of the detector. In the traditional direct detection experiments, the nuclear recoil energy is detected as the detected energy, which does not work for sub-GeV dark matters as they loose their sensitivity. Several new techniques have been considered to probe the sub-GeV dark matter direct detection. Three such experiment can provide constraints for the sub-GeV dark matter:

1. CRESST-III: constrains the elastic spin-independent dark matter-nucleon scattering cross section to be less than $\sigma_{SI} \sim 10^{-35}$cm^2 for $m \sim 200$ MeV [264].

2. XENON1T: cosmic ray boosted dark matter can deposit enough recoil energy to be detected and can give bounds $\sigma_{SI} \leq \mathcal{O}(10^{-29} - 10^{-30})$ cm^2 or $\sigma_{SI} \geq \mathcal{O}(10^{-28})$ cm^2.

3. CDEX-1B: this experiment utilize the Migdal effect and can give constraints for the mass

range 50-180 MeV, which requires the cross section to be less than $\sigma_{SI} \sim 10^{-32} - 10^{-34}\text{cm}^2$.

We will show that, our model satisfies all of the above constraints. We also show projection of differential event rates for future experiments with very low threshold. Studying the dark matter -electron scattering cross section is another way to detect the low mass dark matter regime. Experiments like XENON10 [265], SuperCDMS [266] and SENSEI [267] can put constraints on the dark matter-electron scattering cross section, but our model satisfies them as well.

The differential event rate for nuclear recoil per unit target mass can be expressed as,

$$\frac{dR}{dE_R} = \frac{N_T \rho_\eta}{m_\eta} \int_{v_{min}}^{v_{esc}} v f(v) \left(\frac{d\sigma}{dE_R}\right) d^3v, \tag{3.25}$$

where N_T is the number of target nuclei per unit mass; $\rho_\eta \simeq 0.3$ GeV cm^{-3} is the local dark matter energy density; v is velocity of the incoming dark matter and $f(v)$ is the corresponding normalized velocity distribution, both in detector frame, and; v_{min} is minimum dark matter velocity required for a scatter to produce recoil energy E_R, and $v_{esc} = 540$ km s^{-1} is the local galactic escape velocity of the dark matter. And $(d\sigma/dE_R)$ is the DM-nucleus differential scattering cross section defined, in general, as

$$\frac{d\sigma}{dE_R} = \frac{m_A}{2\mu_{\eta A}^2 v^2} \sigma_0(\eta A \to \eta A) \frac{m_{\phi',A'}^4}{(2m_A E_R + m_{\phi',A'}^2)^2} F^2(E_R), \tag{3.26}$$

where $\mu_{\eta A} = (m_\eta m_A)/(m_\eta + m_A)$ is the reduced mass of the η-nucleus system; $F(E_R)$ is the nuclear form factor; and σ_0 is the scattering cross section at zero momentum transfer. The velocity-distribution and the nuclear form factor used in the calculations are defined in Appendix. C.

There are two distinct channel to generate spin independent (SI) $\sigma_0(\eta A \to \eta A)$ in our model. They are,

- Elastic SI scattering mediated via ϕ', which is isospin-invariant.
- Inelasatic SI scattering mediated by A', which is isospin-violating [268, 269, 270], since the up and down quarks have opposite charges under $U(1)_{T3R}$

The isospin-invariant dark matter-nucleus scattering cross section at zero momentum transfer can be expressed in terms of the dark matter-nucleon spin-independent scattering cross section at zero momentum transfer (σ_{SI}^{N}) as follows,

$$\sigma_0(\eta A \to \eta A) \;=\; \sigma_{SI}^{N} A^2 \frac{\mu_{\eta A}^2}{\mu_{\eta N}^2}, \tag{3.27}$$

where $\mu_{\eta N} = (m_\eta m_N)/(m_\eta + m_N)$ is the reduced mass of the η-nucleon system. For the case of inelastic scattering mediated by A', the factor A^2 in the above formula will be replaced with $(A - 2Z)^2$ due to it's isopin-violating nature. For the elastic scattering $\eta_j A \to \eta_j A$ mediated by the scalar particle ϕ', the dark matter-nucleon spin-independent scattering cross section at zero momentum transfer (σ_{SI}^{N}) is given as,

$$\sigma_{SI}^{scalar(p,n)} = \frac{\mu_{\eta N}^2 m_\eta^2}{4\pi V^4 m_{\phi'}^4} f_{p,n}^2 \tag{3.28}$$

where [166],

$$\frac{f_{p,n}}{m_N} = \sum_{q=u,d,s} f_{T_q}^{(p,n)} \frac{f_q}{m_q} + \frac{2}{27}\left(1 - \sum_{q=u,d,s} f_{T_q}^{(p,n)}\right) \sum_{q=c,b,t} \frac{f_q}{m_q}. \tag{3.29}$$

where, $f_{u,d} = m_{u,d}$, $f_{s,c,b,t} = 0$; $f_{T_u}^{(p)}$, $f_{T_d}^{(p)}$ and $f_{T_s}^{(p)}$ are 0.019, 0.041 and 0.14, respectively [271]; and $f_{T_u}^{(n)}$, $f_{T_d}^{(n)}$ and $f_{T_s}^{(n)}$ are 0.023, 0.034 and 0.14, respectively [271]. The threshold velocity as a function of the nuclear recoil is,

$$v_{min} = \frac{\sqrt{2 m_A E_R}}{2\mu_{\eta A}}. \tag{3.30}$$

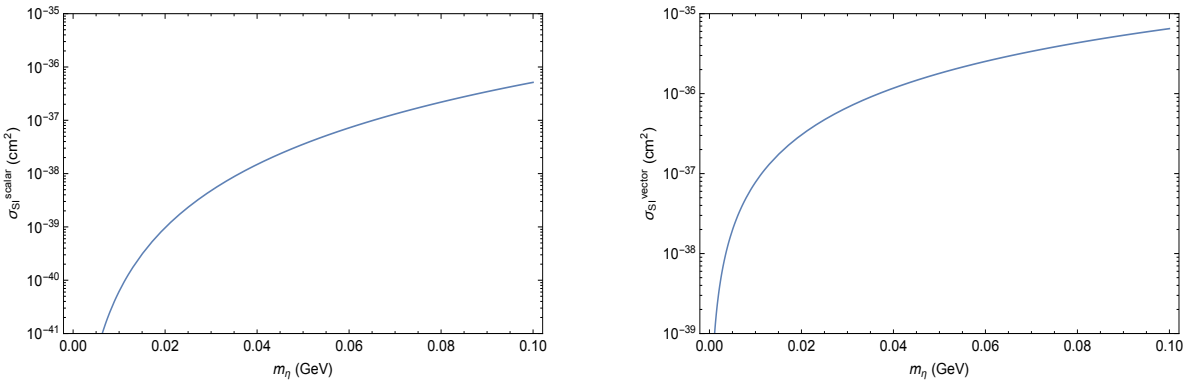

(a) **(b)**

Figure 3.9: Dark matter-nucleon scattering cross section is shown as a function of the dark matter mass for $m_{\phi'} = 200$ MeV, $\delta = 0$ and $V = 10$ GeV.

For the inelastic scattering $\eta_i A \rightarrow \eta_j A$ mediated by the gauge boson A'_μ,the dark matter-nucleon spin-independent scattering cross section at zero momentum transfer (σ_{SI}^N) is given as,

$$\sigma_{SI}^{vector(p,n)} = \frac{\mu_{\eta N}^2}{16\pi V^4}, \tag{3.31}$$

Here, we only consider small δ and keep only the terms which are linear in δ. In this limit, $\mu_{\eta_j N} \simeq \mu_{\eta_i N} = \mu_{\eta N}$ and the threshol velocity is given by,

$$v_{min} = \frac{1}{\sqrt{2 m_A E_R}} \left(\frac{m_A E_R}{\mu_{\eta A}} + \delta \right). \tag{3.32}$$

We show both $\sigma_{SI}^{scalar(p,n)}$ and $\sigma_{SI}^{vector(p,n)}$ in Fig. 3.9, where we set $m_{\phi'} = 200$ MeV, and for the A'-mediated process, we assume $\delta = 0$ (note, σ_{SI}^{vector} does not depend on $m_{A'}$). Both of these scattering cross sections satisfy the constraints posed by XENON1T and CDEX-1B. Note that, the differential scattering cross section in our case will be suppressed by a factor $[1 + (2 m_A E_R)/m_{\phi',A'}^2)]^{-2}$ and the A'-mediated scattering is suppressed by an additional factor of $[1 - (2Z/A)]^2$. On the otherhand, the bounds are derived assuming the dark matter nucleon scattering cross section is equal to the zero momentum transfer cross section. CRESST III does not give any bounds for $m_\eta \leq 100$ MeV. We show the excluded region in the $m_{\phi'}$-m_η parameter

space for the ϕ' mediated elastic scattering corresponding to the XENON1T and CDEX-1B bounds in Fir. 3.13a.

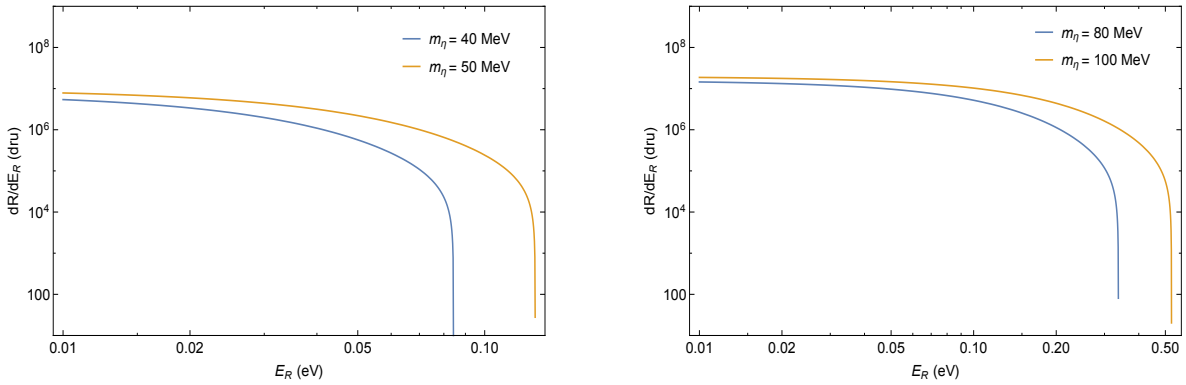

(a) **(b)**

Figure 3.10: Differential event rate for elastic scattering off a Xenon nucleus for different dark matter masses. We used, $m_{\phi'} = 200$ MeV and $V = 10$ GeV. In both panels, the upper limit of recoil energy increases with increasing dark matter masses.

The nuclear recoil spectrum for elastic scattering is shown in Fig. 3.10 and for inelastic scattering is shown in Fig. 3.11 respectively. Here we consider Xenon (A =131 and $Z = 54$) as the target material and express the differential event rate in "differential rate unit" (dru), which is 1 event per keV per kg per day. Note that for the elastic case, the upper limit of E_R increases with the dark matter mass. For the inelastic case, larger values of δ push the nuclear recoil energy, E_R to smaller values in order to satisfy the condition $v_{min} \leq v_{esc}$.

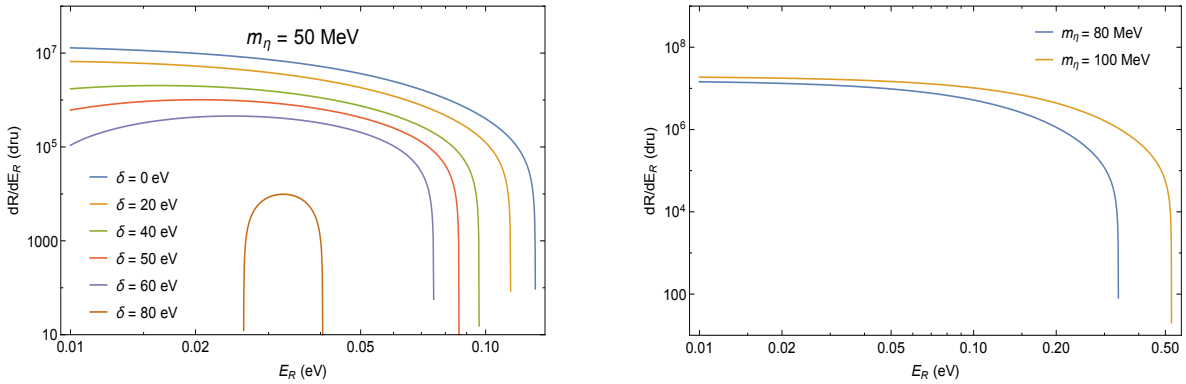

(a) **(b)**

Figure 3.11: Differential event rate for inelastic scattering off a Xenon nucleus for different dark matter masses. We used, $m_{A'} = 55$ MeV and $V = 10$ GeV. Note that the values of maximum recoil energy decrease with the increasing values of δ.

Dark matter-electron scattering also plays important roles to know more about the interactions of dark matter with SM particles. The typical energy of light dark matter with mass $\mathcal{O}(1 - 100)$ MeV is $E \simeq mv^2/2 \simeq 50$ eV$\times(m/100$ MeV$)$ which is not sufficient to deposit enough nuclear recoil to overcome the threshold of the current experiments but is enough for the following processes from dark matter-electron scattering,

- Ionization of electron of orbital electrons in the target atoms.
- Excitation of orbital electrons in the target atoms.

The typical enery required for these processes are $\mathcal{O}(1 - 10)$ eV and dark matter with mass $\mathcal{O}(1-100)$ MeV can produce such signals in the detectors when scatters off the electrons of atoms of the target material. We show the dark matter-electron scattering scross section in Fig. 3.12. For this range of dark matter mass the allowed cross section is $\leq 10^{-38}$ cm^2 [272, 273], comes from experiments like XENON10 [265], SuperCDMS [266] and SENSEI[267]. We also show the exclusion region in Fig. 3.13b.

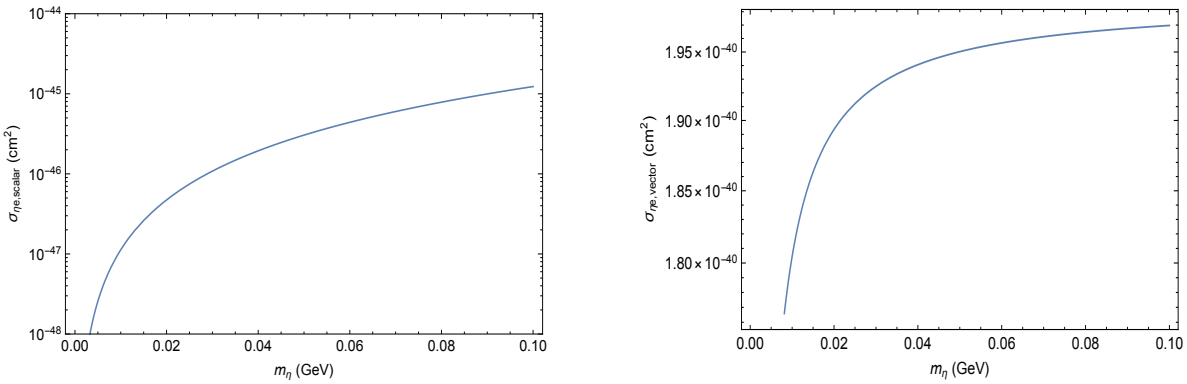

(a) **(b)**

Figure 3.12: Dark matter-electron scattering cross section is shown as a function of the dark matter mass for $m_{\phi'} = 200$ MeV, $\delta = 0$ and $V = 10$ GeV.

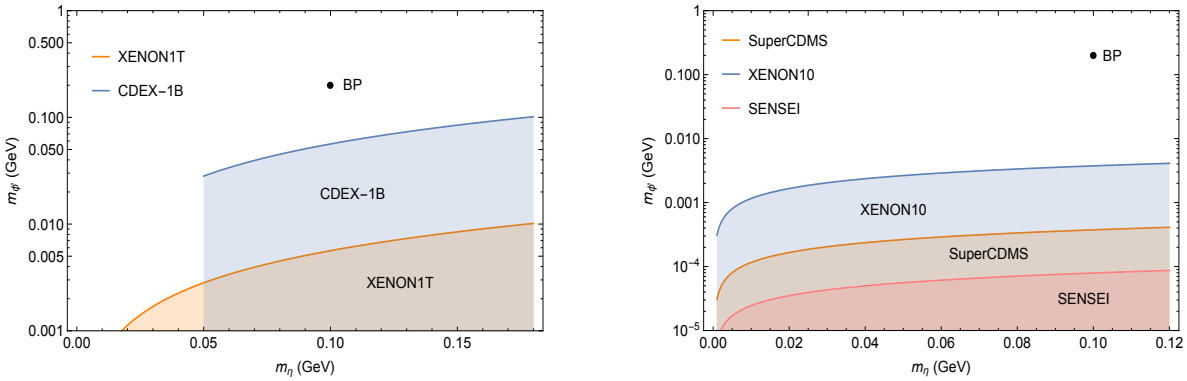

(a) **(b)**

Figure 3.13: Exclusion region shown in the $m_{\phi'}$- m_η parameter space: the left panel is for the dark matter-nucleon cross section bounds and the right panel is for the dark matter-electron cross section constraints. In both panel, we have used: $m_{\phi'} = 200$ MeV, $m_\eta = 100$ MeV and $V = 10$ GeV.

3.4 Relic Density

In this section, we produce the correct relic density of dark matter using the standard theory of thermal relic, where the dark matter abundance is depleted by (co-)annihilation to either Standard Model particles or to other dark sector particles. Correct sub-GeV dark matter relic density can also be obtained in a variety of other non-standard way, e.g. DM production from the decay of a heavy

particle [274], freeze-in [275], modifications to the expansion rate in the early Universe [276] etc. To ensure that, dark matter freezes out before BBN, we assume that $m_\eta > 40$ MeV.

The tightest constraints on dark matter annihilation cross section comes from Planck bounds [32] on the effect of energy injection at the time of the recombination on the CMB. If the s-wave channel, which is dark matter velocity independent dominates the dark matter annihilation and dark matter decay to SM particles, then the produced cross section is large enough to deplete the dark matter abundance ruled out by Planck bounds. One of the following scenario can be used to obtain the correct thermal relic density consistent with these constraints,

- If the dark matter annihilation is p-wave suppressed i.e. velocity dependent, $\langle \sigma v \rangle \propto v^2$. During the freeze out the cross section is suppressed by a factor of 10 as at that time $v = 0.1$ but during the time of recombination, v is very small, thus the cross section is highly suppressed and can evade the Planck bounds

- If the dark matter annihilation produce invisible final states, then there is not extra energy injection during the recombination.

- If dark matter largely co-annihilates at the time of freeze-out, but if the heavier component has decayed away by the time of recombination, then dark matter co-annihilation at the time of recombination will be negligible, and Planck constraints will again be satisfied.

In the following we consider two different channel for obtaining the correct relic density. Note that, A' couplings are suppressed by the mass of the A', while ϕ' couplings are suppressed by the mass of the particle to which it couples.

- ϕ'-resonance: The dominant annihilation is through s-channel ϕ' resosnance, which is p-wave suppressed. The possible final states are $A'A', \bar{\nu}\nu, \bar{\ell}\ell, \pi\pi, \gamma\gamma$, where the ϕ' is nearly on-shell. The resonance condition is needed to enhance the cross section, since the coupling

of ϕ' to the outgoing fermions is suppressed by the mass of the SM fermions.

$$\sigma(\eta_i\eta_i \to \phi' \to X)v_{rel} \sim \frac{m_i^2(E^2-m_i^2)}{4V^2E^2[(4E^2-m_{\phi'}^2)^2+(m_{\phi'}\Gamma_{\phi'})^2]} \times(2m_{\phi'}\Gamma_{\phi'}), \tag{3.33}$$

where $\Gamma_{\phi'}$ is the total decay width of ϕ'.

- A'-mediated: Co-annihilation of dark matter mediated by A' in the early Universe can deplete the dark matter relic abundance correctly if the mass eigenstates η_1 and η_2 have comparable abundances at freeze-out, implying that $\delta/m \leq \mathcal{O}(0.1)$ and that the lifetime of η_2 should be much greater than $\mathcal{O}(1)$ sec. The possible final states are $\nu_A\nu_A$ and e^+e^- (the $\gamma\gamma$ final state is forbidden by the Landau-Yang Theorem [196]). Both of these final states are suppressed, either by a neutrino mixing angle or a kinetic mixing parameter, therefore the co-annihilation via A' will play no role in our benchmark scenario.

We show two benchmark scenario which can deplete the correct thermal relic abundance of dark matter in Table. 3.4. For both them, we considered the ϕ' resonance methods. The corresponding dark matter-nucleon cross section is also mentioned.

$m_{A'}$ (MeV)	$m_{\phi'}$ (MeV)	m_η (MeV)	m_{ν_s}(MeV)	$m_{\nu D}$(MeV)	$\langle\sigma v\rangle$ (cm^3/sec)	σ_{SI}^{scalar}(pb)	σ_{SI}^{vector}(pb)
150	80	40	10	10^{-3}	3×10^{-26}	0.58	1.17
180	76	38	10	10^{-3}	3×10^{-26}	0.58	1.06

Table 3.4: Masses of A', ϕ' and η (DM), and the neutrinos and the corresponding thermal relic abundances are shown . The dark matter-nucleon scattering cross sections for each BP are also shown.

3.5 Explanation of $R_{K^{(*)}}$

In B-physics, there are variety of anomalies in observables based on the process $b \to s\ell^+\ell^-$. Any new physics explanation of these anomalies requires both lepton flavor non-universality and

quark flavor violation. The lepton flavor non-universality arises in our model naturally since the ϕ' and A' couple only to μ at tree-level. On the other hand, when we complete our low energy model with the UV completion described in Sec. 3.1.5, it may introduces flavor violation couplings in the quark sector. Therefore, our model can accommodates the flavor anomalies of the B-physics sector such as [277, 278, 190].

3.5.1 Background

We restrict our analysis only to theoretically clean observables [279] such as R_K, R_{K^*}, and $Br(B_s \to \mu^+\mu^-)$, since they are devoid of hadronic uncertainties. The observables R_K and R_{K^*} are defined as

$$R_K \equiv \frac{Br(B \to K\mu^+\mu^-)}{Br(B \to Ke^+e^-)}\,, \tag{3.34}$$

$$R_{K^*} \equiv \frac{Br(B \to K^*\mu^+\mu^-)}{Br(B \to K^*e^+e^-)}\,. \tag{3.35}$$

Note that, the SM predictions for R_K and R_{K^*} are close to unity [280, 281] due to the lepton flavor universal coupling. But the measurements of these observables are always below the SM predictions [277, 278, 190, 282, 283]. Recently, The LHCb collaboration reported the updated value of the R_K based on the data set of full RUN-1 and Run-2 in the q^2 bin of 1.1 to 6 GeV^2. The analysis now show a 3.1 σ deviation from the SM prediction,

$$R_K = 0.846^{+0.042}_{-0.039}(\text{stat})^{+0.013}_{-0.012}(\text{syst}), \tag{3.36}$$

On the other hand the R_{K^*} measurements [277, 278] disagree with the SM predictions at the 2.4 σ and 2.5 σ respectively for the q^2 bin of $(2m_\mu)^2$ to 1.1 GeV^2 and 1.1 to 6 GeV^2 respectively,

$$R_{K^*} = \begin{cases} 0.660^{+0.11}_{-0.07} \pm 0.03 \;\; (2m_\mu)^2 < q^2 < 1.1 \text{ GeV}^2\,, \\ 0.685^{+0.11}_{-0.07} \pm 0.05 \;\; 1.1 \text{ GeV}^2 < q^2 < 6 \text{ GeV}^2\,, \end{cases} \tag{3.37}$$

For simplicity, we restrict ourselves to the central bin of R_{K^*} measurement, since it is extremely challenging to explain the result of both bins at the same time using the effective operators, and we will wait for more data to confirm the energy dependency [284, 285]. Another clean observables, the branching fraction of $b \to s\,\ell^+\,\ell^-$ transitions, was also reported by LHCb collaboration using the full data set [286],

$$Br(B_s \to \mu^+\mu^-) = 3.09^{+0.46}_{-0.43}(\text{stat})^{+0.15}_{-0.11}(\text{sysm}) \times 10^{-9}. \tag{3.38}$$

ATLAS [287] and CMS [288] also give value of this observable. All of these results favor a decay rate smaller than the SM predictions [289, 279].

3.5.2 Theroretical Calculations

The lepton flavor non-universality from the low energy effective model and the flavor violating couplings originating from the UV completion in our model can generate the process, $b \to s\ell^+\ell^-$. In the UV complete model, the Z and A' couplings to fermions in the flavor eigenstate basis are diagonal matrices which need not be proportional to the identity while, these coupling matrices can become non-diagonal in the mass eigenstate basis, yielding vertices of the form $\bar{b}\gamma^\mu P_{L,R} s(Z, A')_\mu$. One can get contribution to universal quark flavor-changing processes ($b \to s\ell^+\ell^-$) form $\bar{b}\gamma^\mu P_{L,R} s Z_\mu$, while terms of the form $\bar{b}\gamma^\mu P_{L,R} s A'_\mu$ can contribute to lepton non-universal quark flavor-changing processes ($b \to s\mu^+\mu^-$). Note that, such flavor changing interaction vertices are not allowed for photon due to gauge invariance.

In Sec. 3.1.5, we describe the minimal UV completion. Note that, one could add additional generations of these heavy particles, or even a single additional particle, without generating anomalies. We consider an additional χ'_a, neutral under $U(1)_{T3R}$, which mixes with b and s through Lagrangian terms of form $\lambda'_{b,s} H \bar{Q}^{b,s}_L P_R \chi'_a + m'_{b,s} \bar{\chi}'_a P_R q^{b,s}_R + h.c.$ (we assume negligible mixing with the first generation). Note that $(\chi'_a)_R$ has same Z coupling as $(b, s)_R$, therefore the Z-coupling to these right-handed quarks is the identity in every basis. On the other hand, $(\chi'_a)_L$ has a Z coupling which differs from $(b, s)_L$, therefore we would find a vertex of the form $\bar{b}\gamma^\mu P_L s Z_\mu$ at tree-level as

shown in Fig. 3.14a. A coupling of the form $\bar{b}\gamma^\mu P_L s A'_\mu$ is also induced at one-loop through $Z - A'$ kinetic mixing, but this term will generally be small if we consider small kinetic mixing.

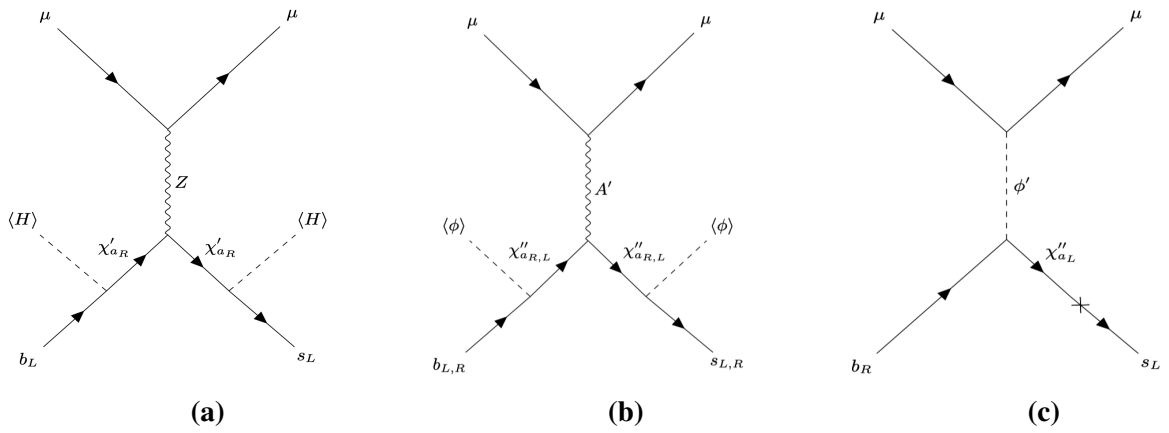

Figure 3.14: Feynman diagrams that contribute to the B-anomalies.

We add another vector-like fermion, χ''_a, charged under $U(1)_{T3R}$ charge $Q_{T3R} = 2$. It has the same SM quantum numbers as $(b, s)_R$ but with and therefore it can mix with b, s (we assuming negligible mixing with d) through a Lagrangian term of the form $\lambda''_{b,s}\phi\bar{\chi}''_a P_R q_{b,s}$. We get a tree-level contribution to the coupling $\bar{b}\gamma^\mu P_{L,R} s A'_\mu$ as shown in Fig. 3.14b, since χ''_a is charged under $U(1)_{T3R}$ while b, s are not. Similarly, since $(\chi''_a)_L$ has a different Z coupling than $(b, s)_L$, this term will yield a tree-level contribution to the coupling $\bar{b}\gamma^\mu P_L s Z_\mu$ while there is no similar contribution to $\bar{b}\gamma^\mu P_R s Z_\mu$, since $(b, s, \chi''_a)_R$ all have identical coupling to the Z boson. A vertex of the form $\lambda''_{b,s}\phi'\bar{q}_{L(s,b)} q_{R(b,s)} \sin\theta'_{(s,b)L}$ is also possible, since χ''_a is charged under $U(1)_{T3R}$. we show the corresponding diagram in Fig. 3.14c.

The effect of these interactions can be approximated with effective operators which couple a (b, s) quark bilinear to a muon bilinear, since the energy transfer is much larger than the mediator. The various effective operators that contribute to the $b \to s\ell^+\ell^-$ process can be written as,

$$\begin{aligned}\mathcal{O}_U^Z &= \frac{e^2}{3m_Z^2}\tan^2\theta_W\left(\sin\theta_{sL}\sin\theta_{bL}+\sin\theta'_{sL}\sin\theta'_{bL}\right)\left(\bar{b}\gamma^\mu P_L s\right)\\ &\quad\times\left(\bar{\mu}\gamma_\mu\left[P_R+\left(1-\frac{1}{2\sin^2\theta_W}\right)P_L\right]\mu\right)\left(\bar{b}\gamma^5 s\right)\left(\bar{\mu}\gamma^5\mu\right) \qquad (3.39)\end{aligned}$$

$$\begin{aligned}\mathcal{O}_{NU}^{A'} &= \frac{1}{\Lambda^2}\sin\theta'_{s(L,R)}\sin\theta'_{b(L,R)}\left(\frac{m_{A'}}{\sqrt{2}V}\right)^2\left(\bar{b}\gamma^\mu P_{L,R}s\right)\left(\bar{\mu}\gamma_\mu P_R\mu\right)\\ &\quad+\frac{1}{\Lambda^2}\sin\theta'_{s(R)}\sin\theta'_{b(R)}\left(\frac{m_\mu m_b}{2V^2}\right)\left(\bar{b}\gamma^5 s\right)\left(\bar{\mu}\gamma^5\mu\right)\\ &\quad-\frac{1}{\Lambda^2}\sin\theta'_{s(L)}\sin\theta'_{b(L)}\left(\frac{m_\mu m_s}{2V^2}\right)\left(\bar{b}\gamma^5 s\right)\left(\bar{\mu}\gamma^5\mu\right) \qquad (3.40)\end{aligned}$$

$$\mathcal{O}_{NU}^{\phi'} = \frac{\lambda''_s}{\Lambda^2}\sin\theta'_{bL}\frac{m_\mu}{\sqrt{2}V}(\bar{b}P_R s)(\bar{\mu}\mu)+\frac{\lambda''_b}{\Lambda^2}\sin\theta'_{sL}\frac{m_\mu}{\sqrt{2}V}(\bar{b}P_L s)(\bar{\mu}\mu), \qquad (3.41)$$

where $\theta_{(s,b)L}$ are the left-handed $(s,b)-\chi'_a$ mixing angles, $\theta'_{(s,b)(L,R)}$ are the left-/right-handed $(s,b)-\chi''_a$ mixing angles, and where we take $\Lambda\sim\mathcal{O}(2)$ GeV.

We expand the above operators using the following basis

$$\frac{\alpha_{em}G_F}{\sqrt{2}\pi}V_{tb}V_{ts}^*\sum_{i,\ell}C_i^{bs\ell\ell}\mathcal{O}_i^{bs\ell\ell}, \qquad (3.42)$$

where different operators are defined as,

$$
\begin{aligned}
\mathcal{O}_9^{bs\ell\ell} &= (\bar{s}\gamma^\mu P_L b)(\bar{\ell}\gamma_\mu \ell), & \mathcal{O}_9^{'bs\ell\ell} &= (\bar{s}\gamma^\mu P_R b)(\bar{\ell}\gamma_\mu \ell), \\
\mathcal{O}_{10}^{bs\ell\ell} &= (\bar{s}\gamma^\mu P_L b)(\bar{\ell}\gamma_\mu \gamma^5 \ell), & \mathcal{O}_{10}^{'bs\ell\ell} &= (\bar{s}\gamma^\mu P_R b)(\bar{\ell}\gamma_\mu \gamma^5 \ell), \\
\mathcal{O}_S^{bs\ell\ell} &= m_b(\bar{s}P_R b)(\bar{\ell}\ell), & \mathcal{O}_S^{'bs\ell\ell} &= m_b(\bar{s}P_L b)(\bar{\ell}\ell), \\
\mathcal{O}_P^{bs\ell\ell} &= m_b(\bar{s}P_R b)(\bar{\ell}\gamma^5 \ell), & \mathcal{O}_P^{'bs\ell\ell} &= m_b(\bar{s}P_L b)(\bar{\ell}\gamma^5 \ell).
\end{aligned} \tag{3.43}
$$

Defining $C_i^U = C_i^{bsee}$ and $C_i^{NU} = C_i^{bs\mu\mu} - C_i^U$, we find

$$
\begin{aligned}
\Delta C_9^U &= (-146)(\sin\theta_{sL}\sin\theta_{bL} + \sin\theta'_{sL}\sin\theta'_{bL}), \\
\Delta C_{10}^U &= (1.8\times 10^3)(\sin\theta_{sL}\sin\theta_{bL} + \sin\theta'_{sL}\sin\theta'_{bL}), \\
\Delta C_9^{NU} &= \Delta C_{10}^{NU} = (1.9\times 10^8)\sin\theta'_{sL}\sin\theta'_{bL}\left(\frac{m_{A'}}{\sqrt{2}V}\right)^2, \\
\Delta C_9^{'NU} &= \Delta C_{10}^{'NU} = (1.9\times 10^8)\sin\theta'_{sR}\sin\theta'_{bR}\left(\frac{m_{A'}}{\sqrt{2}V}\right)^2, \\
\Delta C_P^{NU} &= -\Delta C_P^{'NU} = -(2.0\times 10^5\ \text{GeV}^{-1})\left(\frac{V}{10\ \text{GeV}}\right)^{-2} \\
&\quad \times (\sin\theta'_{sR}\sin\theta'_{bR} - (m_s/m_b)\sin\theta'_{sL}\sin\theta'_{bL}), \\
\Delta C_S^{NU} &= (2.7\times 10^7\ \text{GeV}^{-1})\lambda''_b \sin\theta'_{sL}\frac{m_\mu}{m_b}\left(\frac{V}{10\ \text{GeV}}\right)^{-1}, \\
\Delta C_S^{'NU} &= (2.7\times 10^7\ \text{GeV}^{-1})\lambda''_s \sin\theta'_{bL}\frac{m_\mu}{m_b}\left(\frac{V}{10\ \text{GeV}}\right)^{-1}.
\end{aligned} \tag{3.44}
$$

Since $\sin^2\theta_W \sim 0.23$, the universal lepton vector coupling is negligible.

Note that the coefficients can be controlled by independently-tunable couplings and mixing angles. Also, we have freedom in the quark couplings, although the vector couplings to muons are only right-handed.

3.5.3 Benchmark Scenarios

It is usually very difficult to explain the $R_{K^{(*)}}$ and $B_s \to \mu^+\mu^-$ simultaneously with a vector mediator while respecting all current experimental constraints. The allowed parameter space by beam dump/fixed target experiments are tightly constrained by bounds from neutrino trident production at CCFR [8, 290] and $Br(B \to K^*\nu\nu)$ [291]. Due to the lack of the left handed neutrino couplings in our model, these bounds can not be applicable to our model. But the chiral nature of the couplings give rise to another tight constraints in our model: $C_9^{(\prime)NU} = C_{10}^{(\prime)NU}$, and this constraint makes it difficult to explain the R_K and R_{K^*}, and $Br(B_S \to \mu^+\mu^-)$ measurements simultaneously. The R_K and R_{K^*} measurements prefers a negative $C_9^{bs\mu\mu}$, or a positive $C_{10}^{bs\mu\mu}$ while the smaller decay rate of $B_s \to \mu^+\mu^-$ favors a positive $C_{10}^{bs\mu\mu}$, or a negative $C_{10}^{\prime bs\mu\mu}$. If we want to explain R_K and R_{K^*} with a positive $C_{10}^{bs\mu\mu}$, which is favored by $B_s \to \mu^+\mu^-$, that implies a negative $C_9^{bs\mu\mu}$. Also, we have the relationship, $C_9^{NU} = C_{10}^{NU}$, a negative $C_9^{bs\mu\mu}$ and a positive $C_{10}^{bs\mu\mu}$ imply a negative non-universal part and a positive universal part. Therefore a positive C_{10}^{bsee} will leave the R_K and R_K^* unexplained. We rely on the following scenario to solve this puzzle,

- In the first scenario, we consider non-zero scalar and pseudoscalar couplings and use them to explain $Br(B_S \to \mu^+\mu^-)$, while the other operators take care of $R_{K^{(*)}}$.

- In the second scenario, we consider non-zero primed operators, which only contain the non-universal part. Therefore the contributions are generated from both left-handed and right-handed quark couplings.

Based on the above setup, we consider four different benchmark scenarios. For all of them we calculate the flavor observables such as R_K and R_{K^*}, and $Br(B_S \to \mu^+\mu^-)$ using flavio [292]. In order to understand how well those three measurements can be described and how significant the deviation is from the SM, we also calculate the SM pull, defined as $\sqrt{\Delta\chi^2}$. Note that, we only consider the clean observables from LHCb results to calculate the SM pull.

Benchmark	BMA	BMB	BMC	BMD
C_{10}^{U}	4.85	-5.86	2.7	-5.67
$C_{9,10}^{NU}$	-0.30	3.65	-0.8	4.55
$\lvert C_s - C_s' \rvert$ GeV^{-1}	0.033	0.024	0.011	-
$\lvert C_p - C_p' \rvert$ GeV^{-1}	-	0.030	0.043	-
$C_{9,10}^{\prime NU}$	-	-	-	-1.28
R_K	0.82	0.87	0.86	0.87
$R_K^*[1.1, 6]$	0.83	0.78	0.97	0.89
$Br(B_s \to \mu^+\mu^-)$	3.36×10^{-9}	3.05×10^{-9}	2.67×10^{-9}	3.34×10^{-9}
SM pull	4.4σ	4.6σ	3.8σ	4.2σ

Table 3.5: We summarize the four benchmark scenarios described in the text. The first five rows present the values of the coefficients C_{10}^{U}, $C_{9,10}^{NU}$, $|C_s - C_s'|$ (in units of gev^{-1}), $|C_p - C_p'|$ (in units of gev^{-1}), and $C_{9,10}^{\prime NU}$. Rows 6-8 present predictions for R_K, R_{K^*} (in the $q^2 \in [1.1, 6]$gev^2 bin), and $Br(B_s \to \mu^+\mu^-)$. Row 9 presents the SM pull of each benchmark point.

Out of the four benchmark scenarios, the first three correspond to the scenario described above, where the scalar and pseudo-scalar operators were used to explain the $Br(B_s \to \mu^+\mu^-)$ while the others operators were used to fit R_K and R_{K^*}. In particular, BMA has the scalar operators, and while in BMB, and in BMC, we include both scalar and pseudo-scalar operators. For BMA, R_K and $B_s \to \mu^+\mu^-$ agree with the LHCb results within 1σ, and R_{K^*} agree with the LHCb results within 2σ, and the SM pull is 4.4σ. For BMB, all three observables agree with the LHCb measurements within 1σ, with a SM pull of 4.6σ. For the third benchmark, BMC, R_K and $B_s \to \mu^+\mu^-$ agree with the LHCb results within 1σ, while R_{K^*} is SM like. The fourth benchmark, BMD, corresponds to the second scenario. Here, we introduce the primed operators, which includes non-universal part. R_K and $B_s \to \mu^+\mu^-$ agree with the LHCb results within 1σ, and R_{K^*} agree with the LHCb results within 2σ, and the SM pull is 4.7σ

In Table. 3.6, we summarize the predictions for other variables along with the experimental

value and the SM predictions, related to $b \to s\ell^+\ell^-$ for our model. Note that, these observables have large theoretical uncertainties related to hadronic form factors.

Observable	Measured Value	SM	BMA	BMB	BMC	BMD
$Br(B^+ \to K^{*+}\mu^+\mu^-)(10^{-8})$ [15.0, 19.0]	$15.8^{+3.2}_{-2.9} \pm 1.1$ [293]	26.8±3.6	7.80	82.9	10.4	92.4
$Br(B^0 \to K^0\mu^+\mu^-)$ (10^{-8}) [15.0,22.0]	6.7±1.1±0.4 [293]	9.8±1.0	3.31	30.4	4.15	29.4
$Br(B^+ \to K^+\mu^+\mu^-)(10^{-8})$ [15.0,22.0]	$8.5 \pm 0.3 \pm 0.4$ [293]	10.7 ± 1.2	3.59	33.0	4.5	32.0
$\frac{dB(B_S\to\phi\mu^+\mu^-)}{dq^2}$ (10^{-8} GeV^{-2}) [1.0,6.0]	$2.57^{+0.33}_{-0.31} \pm 0.08 \pm 0.19$ [294]	4.81 ± 0.56	1.60	16.8	2.28	18.7
$\frac{dB(\Lambda_b^0\to\Lambda\mu^+\mu^-)}{dq^2}$ (10^{-7} GeV^{-2}) [15,20]	$1.18^{+0.09}_{-0.08} \pm 0.03 \pm 0.27$ [295]	0.71 ± 0.08	2.19	2.28	0.29	2.48

Table 3.6: Predictions for observables for the four benchmark scenarios summarized in the Table. 3.5, along with the Standard Model prediction and the measured value with uncertainties. The uncertainties, from left to right, are statistical, systematic and due to the normalisation mode (for the last two only). Rows 1-3 consider $Br(B^+ \to K^{*+}\mu^+\mu^-)(q^2 \in [15, 19]\text{gev}^2)$, $Br(B^0 \to K^0\mu^+\mu^-)(q^2 \in [15, 19]\text{gev}^2)$, and $Br(B^+ \to K^+\mu^+\mu^-)(q^2 \in [15, 22]\text{gev}^2)$, respectively, all in units of 10^{-8}. Row 4 considers $dBr(B_S \to \phi\mu^+\mu^-)/dq^2$, in units of 10^{-8}gev^{-2}, averaged over $q^2 \in [1, 6]\text{gev}^2$, while row 5 considers $dBr(\Lambda_b^0 \to \Lambda\mu^+\mu^-)/dq^2$, in units of 10^{-7}gev^{-2}, averaged over $q^2 \in [15, 20]\text{gev}^2$.

3.6 Conclusions

In this chapter, we have considered the scenario where only the right-handed light SM fermions are charged under a new gauge group, $U(1)_{T3R}$. This scenario is of particular interest because it can tie the symmetry breaking scale of $U(1)_{T3R}$ to that of the light SM fermions and the new dark sector physics. Sub-GeV particles arise naturally from the scenario including dark matter, sterile neutrinos, dark photon, and dark Higgs. Besides that, this model can address the hierarchy problem in the light fermion sector of the SM.

We find that the parameter space of the model is tightly constrained by various laboratory-based experiments and cosmological/astrophysical observables. But there is enough open parameter space is available, part of which can be probed in the upcoming/future experiments. We show,

for example, on possibility in Fig. 3.15. Still, there is a part of the parameter space which these upcoming/future experiments can not probe. The parameter space is also consistent with the currently available data from the dark matter direct detection experiments. Another interesting feature of the model is that it can produce the thermal relic density of dark matter by evading Planck bounds consistently. Moreover, this model has the potential to explain some of the recent flavor anomalies such as $R_{K^{(*)}}$.

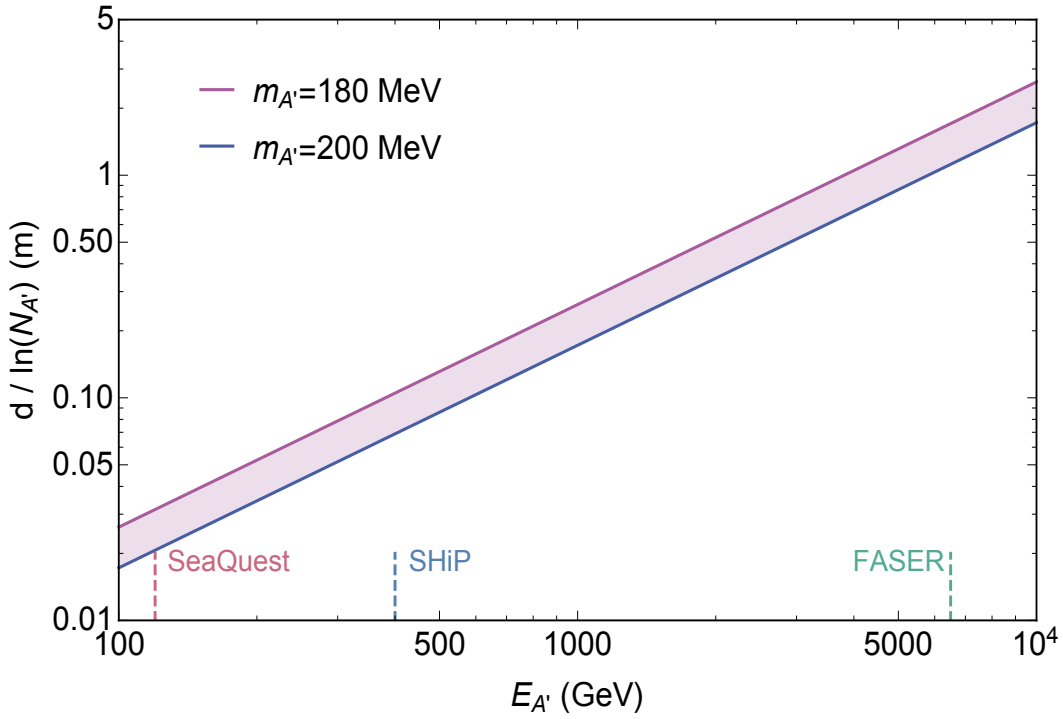

Figure 3.15: We show the estimation of maximum $d/\ln(N_{A'})$ necessary for an experiment to be able to probe our model for $m_{A'} \in [180 - 200]$ MeV, as a function of the maximum A' energy produced by the experiment. d is the distance of the detector from the beam dump, and $N_{A'}$ is the number of A' at energy $E_{A'}$ produced in a beam aimed at the detector. The maximum A' energies for the experiments like FASER, SHiP and SeaQuest are also shown.

4. A THREE-LOOP NEUTRINO MASS MODEL*

Tiny neutrino masses can be obtained at tree level using Weinberg's dimension-5 operator [296],

$$\mathcal{L}_5 = f_{ijmn}\bar{l}^C_{i\alpha L} l_{j\beta L}\phi^{(m)}_\gamma \phi^{(n)}_\delta \epsilon_{\alpha\gamma}\epsilon_{\beta\delta} + f'_{ijmn}\bar{l}^C_{i\alpha L} l_{j\beta L}\phi^{(m)}_\gamma \phi^{(n)}_\delta \epsilon_{\alpha\beta}\epsilon_{\gamma\delta} \ , \tag{4.1}$$

But to realize them in the context of a model one needs a very high scale particle, usually at the Grand Unified Theory scale which is inaccessible at LHC. Therefore to obtain the neutrino mass using a testable new physics scale, one needs a new suppression mechanism such as the radiatively generated neutrino mass. At the n-loop order, a dimension d diagram estimates the neutrino mass as

$$m_\nu \sim c \times \left(\frac{1}{16\pi^2}\right)^n \times \frac{\langle v_0^{(m)}\rangle^{2k}}{M^{2k-1}} \ , \tag{4.2}$$

where c is a dimensionless quantity contains all the coupling constants and other mass ratios, and the mass dimension of the corresponding effective operator is $2k+3$. For example, we consider the dimension-5 Weinberg operator with $n=3$ and $k=1$ in this paper.

We build a model by extending the SM by the gauge group $SU(2)_N$, which arises from the decomposition of E_6 GUT. We also impose a discrete Z_2 symmetry such that only one particle is odd under it and can be a viable dark matter candidate. The matter content of the model and the Z_2 symmetry prevent the Majorana neutrino mass from being generated below the three-loop level. One can realize the dimension-5 effective Majorana neutrino mass operator at the three-loop level in the model. The three-loop suppression factor pushes the new scale to TeV. The new flavor structure involving the vector-like leptons can explain both muon and electron anomalous magnetic moment simultaneously mediated by scalar mediators. The new particles of the model satisfy all the current constraints from LHC and can be tested in future collider experiments.

*this chapter is reprinted from " **Three-loop neutrino masses via new massive gauge bosons from E_6 GUT**" by B. Dutta, S. Ghosh, I. Gogoladze and T. Li, Phys. Rev. D **98**, no. 5, 055028 (2018) and "$(g-2)_{\mu,e}$ **and the ANITA anomalous events in a three-loop neutrino mass model**" by M. Abdullah, B. Dutta, S. Ghosh and T. Li, Phys. Rev. D **100**, no. 11, 115006 (2019) published by the American Physical Society under the terms of the Creative Commons Attribution 4.0 International license.

The rest of this chapter is organized as: In Sec. 4.1, we describe the gauge symmetry, particle content, and the Higgs potential of our model. In Sec. 4.2, we derive all the necessary physical scalars and fermions. The gauge boson masses and interactions are discussed in Sec. 4.3. In Sec. 4.4, the theoretical framework and numerical analysis of the neutrino mass and mixing are described. The anomalous magnetic moment of both muon and electron are explained in Sec. 4.5. We conclude in Sec. 4.6.

4.1 Model Building

In this section, we discuss the gauge symmetry and the field content of our model. The low energy gauge symmetry of our model is $SU(3)_C \times SU(2)_L \times SU(2)_N \times U(1)_Y$. Note that, $SU(2)_N$ has no component to the electric charge operator in our model, so the charge operator is defined as $Q = T_{3L} + Y$. This symmetry structure can arise from the E_6 GUT. One possible maximal subgroup of E_6 is $SU(6) \times SU(2)_N$ while the $SU(6)$ group has a maximal subgroup $SU(5) \times U(1)'$. We assume that $U(1)'$ gauge symmetry is broken at a very high scale, possibly around the GUT scale.On the other hand, $SU(5)$ group contains the SM gauge symmetry. Hence we get our symmetry structure. We assume that the $SU(2)_L$ doublet assignments are vertical and the $SU(2)_N$ doublets are horizontal. The fermionic field content is given as,

$$Q_i \sim \begin{pmatrix} u_i \\ d_i \end{pmatrix} \sim (3,2,1,\frac{1}{6}), \quad U_i^c \sim (\bar{3},1,1,-\frac{2}{3}), \quad D_i^c \sim \begin{pmatrix} d'^c_i & d^c_i \end{pmatrix} \sim (\bar{3},1,2,\frac{1}{3}) \,,$$

$$D_i \sim (3,1,1,-\frac{1}{3}), \quad L_i \sim \begin{pmatrix} E_i^0 & \nu_i \\ E_i^- & e_i^- \end{pmatrix} \sim (1,2,2,-\frac{1}{2}), \quad E_i^c \sim (1,1,1,1) \,,$$

$$L_i{}' \sim \begin{pmatrix} E_i^+ \\ \bar{E}_i^{\,0} \end{pmatrix} \sim (1,2,1,\frac{1}{2}), \quad N_i^c \sim \begin{pmatrix} n^c_{1i} & n^c_{2i} \end{pmatrix} \sim (1,1,2,0) \,,$$

$$F_i \sim \begin{pmatrix} F_{3i} & F_{1i} \\ F_{2i} & -F_{3i} \end{pmatrix} \sim (1,1,3,-1), \quad F_i{}^c \sim \begin{pmatrix} F^c_{3i} & F^c_{1i} \\ F^c_{2i} & -F^c_{3i} \end{pmatrix} \sim (1,1,3,1) \,,$$

where $i = 1, 2, 3$ are the family index. We can get Q_i, U_i^c, D_i^c, D_i, L_i, E_i^c, L_i', and N_i^c from the fundamental representation of E_6 i.e. **27** , while the vector-like fermions F_i and F_i^c come from the **351** and $\overline{\mathbf{351}}$ representations of E_6, respectively. By construction, this scenario is free of all gauge and gravitational anomalies.

The scalar sector of the model contains four scalar fields and given as,

$$H_d \sim \begin{pmatrix} {\phi_1}^0 & {\phi_3}^0 \\ {\phi_1}^- & {\phi_3}^- \end{pmatrix} \sim (1, 2, 2, -\frac{1}{2}), \quad H_u \sim \begin{pmatrix} {\phi_2}^+ \\ {\phi_2}^0 \end{pmatrix} \sim (1, 2, 1, \frac{1}{2}) \,,$$

$$S^0 \sim \begin{pmatrix} S_1^0 & S_2^0 \end{pmatrix} \sim (1, 1, 2, 0), \quad T \sim \begin{pmatrix} {T_1}^{++} & {T_2}^{++} \\ {T_1}^+ & {T_2}^+ \end{pmatrix} \sim (1, 2, 2, \frac{3}{2}) \,.$$

One **27** representation of E_6 can give H_d, H_u, and S^0 and we get the bi-doublet scalar field T from one **650** representation. S^0 acquires a VEV and breaks $SU(2)_N$ gauge symmetry while the electroweak gauge symmetry is broken by the VEVs of H_d and H_u.

The most general renormalizable scalar potential is given by,

$$\begin{aligned} V_{potential} \;=\; & m_1^2 H_{d\alpha\beta}^\dagger H_{d\beta\alpha} + m_2^2 H_{u\alpha}^\dagger H_{u\alpha} + m_s^2 S_\alpha^0 {S^0}^\dagger_\alpha + m_T^2 T_{\alpha\beta}^\dagger T_{\beta\alpha} + \frac{\lambda_2}{2} H_{u\alpha}^\dagger H_{u\alpha} H_{u\beta}^\dagger H_{u\beta} \\ & + \frac{\lambda_1}{2} H_{d\alpha\beta}^\dagger H_{d\beta\alpha} H_{d\gamma\delta}^\dagger H_{d\delta\gamma} + \frac{\lambda_3}{2} H_{d\alpha\beta}^\dagger H_{d\beta\gamma} H_{d\gamma\delta}^\dagger H_{d\delta\alpha} + \frac{\lambda_s}{2} S_\alpha^0 {S^0}^\dagger_\alpha S_\beta^0 {S^0}^\dagger_\beta \\ & + \frac{\lambda_6}{2} T_{\alpha\beta}^\dagger T_{\beta\alpha} T_{\gamma\delta}^\dagger T_{\delta\gamma} + \frac{\lambda_7}{2} T_{\alpha\beta}^\dagger T_{\beta\gamma} T_{\gamma\delta}^\dagger T_{\delta\alpha} + \lambda_4 H_{u\gamma}^\dagger H_{u\gamma} H_{d\alpha\beta}^\dagger H_{d\beta\alpha} \\ & + \lambda_5 H_{u\alpha}^\dagger H_{d\alpha\beta} H_{d\beta\gamma}^\dagger H_{u\gamma} + \lambda_8 H_{u\alpha}^\dagger H_{u\alpha} S_\beta^0 {S^0}^\dagger_\beta + \lambda_9 S_\gamma^0 {S^0}^\dagger_\gamma H_{d\alpha\beta}^\dagger H_{d\beta\alpha} \\ & + \lambda_{10} S_\alpha^0 H_{d\alpha\beta}^\dagger H_{d\beta\gamma} {S^0}^\dagger_\gamma + \lambda_{11} S_\gamma^0 {S^0}^\dagger_\gamma T_{\alpha\beta}^\dagger T_{\beta\alpha} + \lambda_{12} S_\alpha^0 T_{\alpha\beta}^\dagger T_{\beta\gamma} {S^0}^\dagger_\gamma + \lambda_{13} H_{u\gamma}^\dagger H_{u\gamma} T_{\alpha\beta}^\dagger T_{\beta\alpha} \\ & + \lambda_{14} H_{u\alpha}^\dagger T_{\alpha\beta} T_{\beta\gamma}^\dagger H_{u\gamma} + \lambda_{15} H_{d\alpha\beta}^\dagger H_{d\beta\alpha} T_{\gamma\delta}^\dagger T_{\delta\gamma} + \lambda_{16} H_{d\alpha\beta}^\dagger H_{d\beta\gamma} T_{\gamma\delta}^\dagger T_{\delta\alpha} \\ & + \lambda_{17} H_{d\alpha\beta}^\dagger T_{\beta\alpha} T_{\gamma\delta}^\dagger H_{d\delta\gamma} + \lambda' [H_{u\alpha} H_{d\beta\gamma} S_\delta^0 \epsilon_{\alpha\beta} \epsilon_{\gamma\delta} + H.c] \\ & + \lambda [T_{\alpha\rho} H_{d\beta\sigma} H_{d\gamma\mu} H_{d\delta\nu} \epsilon_{\alpha\beta} \epsilon_{\rho\sigma} \epsilon_{\gamma\delta} \epsilon_{\mu\nu} + T_{\alpha\rho} H_{d\beta\sigma} H_{d\gamma\mu} H_{d\delta\nu} \epsilon_{\alpha\beta} \epsilon_{\rho\mu} \epsilon_{\gamma\delta} \epsilon_{\sigma\nu} + H.c] \,, \end{aligned} \quad (4.3)$$

where α, β, γ, δ, ρ, σ, μ and ν are the $SU(2)$ indices and $\epsilon_{\alpha\beta}$ is the totally antisymmetric $SU(2)$ tensor with $\epsilon_{12} = +1$. We also assume that all the parameters are real.

The minimization conditions for Eq. 4.3 are given as,

$$m_1^2 + \frac{1}{2}(\lambda_1 + \lambda_3)v_1^2 + \frac{1}{2}\lambda_4 v_2^2 + \frac{1}{2}\lambda_9 v_s^2 - \frac{1}{\sqrt{2}}\lambda' \frac{v_2 v_s}{v_1} = 0 \,, \tag{4.4}$$

$$m_2^2 + \frac{1}{2}\lambda_4 v_1^2 + \frac{1}{2}\lambda_2 v_2^2 + \frac{1}{2}\lambda_8 v_s^2 - \frac{1}{\sqrt{2}}\lambda' \frac{v_1 v_s}{v_2} = 0 \,, \tag{4.5}$$

$$m_s^2 + \frac{1}{2}\lambda_9 v_1^2 + \frac{1}{2}\lambda_8 v_2^2 + \frac{1}{2}\lambda_s v_s^2 - \frac{1}{\sqrt{2}}\lambda' \frac{v_1 v_2}{v_s} = 0 \,. \tag{4.6}$$

We write the most general Lagrangian for the Yukawa sector and the mass terms for the vector-like fermions as,

$$\begin{aligned} -\mathcal{L}_{Yukawa} \;=\; & y_{1ij} L_{i\alpha\beta} T_{\gamma\beta} F_{j\delta\delta} \epsilon_{\alpha\gamma} \epsilon_{\beta\delta} \epsilon_{\beta\delta} + y_{2ij} L_{i\alpha\beta} H_{d\gamma\beta} F^c_{j\delta\delta} \epsilon_{\alpha\gamma} \epsilon_{\beta\delta} \epsilon_{\beta\delta} + y_{3ij} Q_{i\alpha} H_{d\beta\gamma} D^c_{j\delta} \epsilon_{\alpha\beta} \epsilon_{\gamma\delta} \\ & + y_{4ij} Q_{i\alpha} H_{u\beta} U^c_j \epsilon_{\alpha\beta} + y_{5ij} D^c_{i\alpha} S^0{}_\beta D_j \epsilon_{\alpha\beta} + y_{6ij} L_{i\alpha\gamma} L'{}_{j\beta} S^0{}_\delta \epsilon_{\alpha\beta} \epsilon_{\gamma\delta} \\ & + y_{7ij} L'_{i\alpha} H_{d\beta\gamma} N^c{}_{j\delta} \epsilon_{\alpha\beta} \epsilon_{\gamma\delta} + y_{8ij} L_{i\alpha\gamma} H_{d\beta\delta} E^c_j \epsilon_{\alpha\beta} \epsilon_{\gamma\delta} + y_{9ij} L_{i\alpha\gamma} H_{u\beta} N^c_{j\delta} \epsilon_{\alpha\beta} \epsilon_{\gamma\delta} \\ & + \frac{1}{2} M_{ij} F_i F^c_j + \mu_{ij} F_i E^c_j + m_{Nij} N^c_i N^c_j \,, \end{aligned} \tag{4.7}$$

where i and j are the family indices; α, β, γ and δ are $SU(2)$ indices; and $\epsilon_{\alpha\beta}$ is the totally antisymmetric $SU(2)$ tensor with $\epsilon_{12} = +1$. For simplicity, we make the following assumptions: $M_{ij} = M_i \delta_{ij}$, and $\mu_{ij} = 0$. We also impose a discrete Z_2 symmetry. Under this discrete symmetry, only N^c_i are odd while all other particles are even. In such a scenario, the terms in Eq. 4.7 proportional to the couplings y_{7ij} and y_{9ij} are forbidden. The physical states of N^c_i are denoted as $n_1, n_2, and n_3$ and the lightest component is thus stable and can be a viable dark matter candidate in our model. Note that, there are no low-energy neutrino mass terms at tree level.

We rewrite the Yukawa Lagrangian using the explicit form of the fermionic and the scalar fields

as follows,

$$
\begin{aligned}
-\mathcal{L}_Y &= y_{1ij}(-E_i^0 T_1^+ + \nu_i T_2^+ + E_i^- {T_1}^{++} - e_i^- {T_2}^{++}) F_{3j} \\
&+ y_{2ij}(-E_i^0 \phi_1^- + \nu_i \phi_3^- + E_i^- \phi_1^0 - e_i^- \phi_3^0) F_{3j}^c \\
&+ y_{3ij}[(u_i \phi_1^- - d_i \phi_1^0) d_j^c - (u_i \phi_3^- - d_i \phi_3^0) {d'}_j^c] + y_{4ij}(u_i \phi_2^0 - d_i \phi_2^+) U_j^c \\
&+ y_{5ij}({d'}_i^c S_2^0 - d_i^c S_1^0) D_j + y_{6ij}[(E_i^0 \bar{E}_j^0 - E_i^- E_j^+) S_2^0 - (\nu_i \bar{E}_j^0 - e_i^- E_j^+) S_1^0] \\
&+ y_{8ij}(E_i^0 \phi_3^- - \nu_i \phi_1^- - E_i^- \phi_3^0 + e_i^- \phi_1^0) E_j^c + \frac{1}{2} M_i F_i F_i^c + m_{Nij} N_i^c N_j^c \,. \qquad (4.8)
\end{aligned}
$$

We consider that only three scalar fields get vev: $\langle \phi_1^0 \rangle = \frac{v_1}{\sqrt{2}}$, $\langle \phi_2^0 \rangle = \frac{v_2}{\sqrt{2}}$, and $\langle S_2^0 \rangle = \frac{v_s}{\sqrt{2}}$. Note that, such vev assignment mean that, H_d controls the mass of down-type quarks and the charged leptons, while H_u gives mass to the up-type quarks. Vector-like particles get mass from S^0 field.

4.2 Physical Scalars and Fermions

We calculate the mass terms for all the necessary physical scalars and fermions in this section. After the spontaneous symmetry breaking, H_d, H_u and S^0 obtains vevs and we can write them as

$$
H_d \sim \begin{pmatrix} \frac{1}{\sqrt{2}}(v_1 + \rho_1 + i\eta_1) & \frac{1}{\sqrt{2}}(\rho_3 + i\eta_3) \\ {\phi_1}^- & {\phi_3}^- \end{pmatrix} , \qquad (4.9)
$$

$$
H_u \sim \begin{pmatrix} {\phi_2}^+ \\ \frac{1}{\sqrt{2}}(v_2 + \rho_2 + i\eta_2) \end{pmatrix} , \quad S^0 \sim \begin{pmatrix} \frac{1}{\sqrt{2}}(\rho_{1s} + i\eta_{1s}) & \frac{1}{\sqrt{2}}(v_s + \rho_{2s} + i\eta_{2s}) \end{pmatrix} . \qquad (4.10)
$$

Using Eq. 4.9 and 4.10 in Eq. 4.3, we can get the mass terms of the various physical scalars.

We start with the single charged scalar mass squared terms,

$$
\begin{aligned}
V^{\pm}_{mass} &= \left(\frac{\lambda_5 v_1 v_2}{2} + \frac{\lambda' v_s}{\sqrt{2}}\right)\begin{pmatrix}\phi_1^- & \phi_2^-\end{pmatrix}\begin{pmatrix}\frac{v_2}{v_1} & 1\\ 1 & \frac{v_1}{v_2}\end{pmatrix}\begin{pmatrix}\phi_1^+\\ \phi_2^+\end{pmatrix} \\
&+ \begin{pmatrix}\phi_3^- & T_2^-\end{pmatrix}\begin{pmatrix}{m'_{\pm}}^2 & 6\lambda v_1^2\\ 6\lambda v_1^2 & {m''_{\pm}}^2\end{pmatrix}\begin{pmatrix}\phi_3^+\\ T_2^+\end{pmatrix} \\
&+ \left[m_T^2 + \frac{(\lambda_{15}+\lambda_{16})v_1^2}{2} + \frac{(\lambda_{13}+\lambda_{14})v_2^2}{2} + \frac{\lambda_{11}v_s^2}{2}\right] T_1^- T_1^+ \,. \qquad (4.11)
\end{aligned}
$$

where,

$$
{m'_{\pm}}^2 = -\frac{\lambda_3 v_1^2}{2} + \frac{\lambda_5 v_2^2}{2} + \frac{\lambda_{10} v_s^2}{2} + \frac{\lambda' v_2 v_s}{\sqrt{2} v_1} \qquad (4.12)
$$

and

$$
{m''_{\pm}}^2 = m_T^2 + \frac{\lambda_{15} v_1^2}{2} + \frac{(\lambda_{13}+\lambda_{14})v_2^2}{2} + \frac{(\lambda_{11}+\lambda_{12})v_s^2}{2} \qquad (4.13)
$$

The charged states $\phi_1^{\pm}$ and $\phi_2^{\pm}$ mix and give four charged scalars $h_1^{\pm}$ and $h_2^{\pm}$ with mass squared $m_{h_1}^2 = 0$ and $m_{h_2}^2 = \frac{v_1^2+v_2^2}{v_1 v_2}\left(\frac{\lambda_5 v_1 v_2}{2} + \frac{\lambda' v_s}{\sqrt{2}}\right)$ respectively. The two massless states corresponding to two charged Goldstone modes, and the other two states $h_2^{\pm}$ are two single charged physical scalars. They can be expressed as,

$$
h_1^{\pm} = \cos\beta\ \phi_1^{\pm} + \sin\beta\ \phi_2^{\pm}\ , \qquad (4.14)
$$

$$
h_2^{\pm} = -\sin\beta\ \phi_1^{\pm} + \cos\beta\ \phi_2^{\pm}\ , \qquad (4.15)
$$

where the mixing angle is given by, $\tan\beta = \frac{v_2}{v_1}$. Similarly, we get four more charged physical scalars $H_1^{\pm}$ and $H_2^{\pm}$ from the mixing of $\phi_3^{\pm}$ and $T_2^{\pm}$ as follows,

$$
H_1^{\pm} = \cos\theta\ \phi_3^{\pm} + \sin\theta\ T_2^{\pm}\ , \qquad (4.16)
$$

$$
H_2^{\pm} = -\sin\theta\ \phi_3^{\pm} + \cos\theta\ T_2^{\pm}\ , \qquad (4.17)
$$

The corresponding mass squared are,

$$m^2_{H_1^\pm} = \frac{1}{2}(m_2^2 + m_3^2) + \frac{1}{2}\sqrt{(m_2^2 - m_3^2)^2 + 144\lambda^2 v_1^4} \tag{4.18}$$

and

$$m^2_{H_2^\pm} = \frac{1}{2}(m_2^2 + m_3^2) - \frac{1}{2}\sqrt{(m_2^2 - m_3^2)^2 + 144\lambda^2 v_1^4}\,, \tag{4.19}$$

respectively. The mixing angle is defined as $\tan 2\theta = \frac{12\lambda v_1^2}{m_2^2 - m_3^2}$. The definition of the parameters m_2^2 and m_3^2 are

$$m_2^2 = m_T^2 + \frac{\lambda_{15} v_1^2}{2} + \frac{(\lambda_{13} + \lambda_{14}) v_2^2}{2} + \frac{(\lambda_{11} + \lambda_{12}) v_s^2}{2}\,, \tag{4.20}$$

and

$$m_3^2 = -\frac{\lambda_3 v_1^2}{2} + \frac{\lambda_5 v_2^2}{2} + \frac{\lambda_{10} v_s^2}{2} + \frac{\lambda' v_2 v_s}{\sqrt{2} v_1}\,. \tag{4.21}$$

We get two more physical scalar states, $T_1^\pm$, which are singly charged, with mass squared given by,

$$m^2_{T_1^\pm} = m_T^2 + \frac{(\lambda_{15} + \lambda_{16}) v_1^2}{2} + \frac{(\lambda_{13} + \lambda_{14}) v_2^2}{2} + \frac{\lambda_{11} v_s^2}{2}\,. \tag{4.22}$$

We get four doubly charged physical scalars $T_1^{\pm\pm}$ and $T_2^{\pm\pm}$ from the following term,

$$V^{\pm\pm}_{mass} = \begin{pmatrix} T_1^{--} & T_2^{--} \end{pmatrix} \begin{pmatrix} m^2_{T_1^{\pm\pm}} & 0 \\ 0 & m^2_{T_2^{\pm\pm}} \end{pmatrix} \begin{pmatrix} T_1^{++} \\ T_2^{++} \end{pmatrix}\,. \tag{4.23}$$

Note that, the matrix is already diagonalized. We have defined the following terms,

$$m^2_{T_1^{\pm\pm}} = m_T^2 + \frac{(\lambda_{15} + \lambda_{16} + \lambda_{17}) v_1^2}{2} + \frac{\lambda_{13} v_2^2}{2} + \frac{\lambda_{11} v_s^2}{2}\,, \tag{4.24}$$

and

$$m^2_{T_2^{\pm\pm}} = m_T^2 + \frac{\lambda_{15} v_1^2}{2} + \frac{\lambda_{13} v_2^2}{2} + \frac{(\lambda_{11} + \lambda_{12}) v_s^2}{2}\,, \tag{4.25}$$

respectively.

There are 5 neutral CP-even states and 5 neutral CP-odd states. The mass terms for CP-even states can be written as,

$$
\begin{aligned}
V^{\rho}_{mass} &= (\rho_1 \;\; \rho_2 \;\; \rho_{2s}) \begin{pmatrix} \frac{(\lambda_1+\lambda_3)v_1^2}{2} + \frac{\lambda' v_2 v_s}{2\sqrt{2}v_1} & \frac{\lambda_4 v_1 v_2}{2} - \frac{\lambda' v_s}{2\sqrt{2}} & \frac{\lambda_9 v_1 v_s}{2} - \frac{\lambda' v_2}{2\sqrt{2}} \\ \frac{\lambda_4 v_1 v_2}{2} - \frac{\lambda' v_s}{2\sqrt{2}} & \frac{\lambda_2 v_2^2}{2} + \frac{\lambda' v_1 v_s}{2\sqrt{2}v_2} & \frac{\lambda_8 v_2 v_s}{2} - \frac{\lambda' v_1}{2\sqrt{2}} \\ \frac{\lambda_9 v_1 v_s}{2} - \frac{\lambda' v_2}{2\sqrt{2}} & \frac{\lambda_8 v_2 v_s}{2} - \frac{\lambda' v_1}{2\sqrt{2}} & \frac{\lambda_s v_s^2}{2} + \frac{\lambda' v_1 v_2}{2\sqrt{2}v_s} \end{pmatrix} \begin{pmatrix} \rho_1 \\ \rho_2 \\ \rho_{2s} \end{pmatrix} \\
&\quad + \left(\frac{\lambda_{10} v_1 v_s}{4} + \frac{\lambda' v_2}{2\sqrt{2}} \right) (\rho_3 \;\; \rho_{1s}) \begin{pmatrix} \frac{v_s}{v_1} & 1 \\ 1 & \frac{v_1}{v_s} \end{pmatrix} \begin{pmatrix} \rho_3 \\ \rho_{1s} \end{pmatrix} . \qquad (4.26)
\end{aligned}
$$

and the for the CP-odd states,

$$
\begin{aligned}
V^{\eta}_{mass} &= \frac{\lambda'}{2\sqrt{2}} (\eta_1 \;\; \eta_2 \;\; \eta_{2s}) \begin{pmatrix} \frac{v_2 v_s}{v_1} & v_s & v_2 \\ v_s & \frac{v_1 v_s}{v_2} & v_1 \\ v_2 & v_1 & \frac{v_1 v_2}{v_s} \end{pmatrix} \begin{pmatrix} \eta_1 \\ \eta_2 \\ \eta_{2s} \end{pmatrix} \\
&\quad + \left(\frac{\lambda_{10} v_1 v_s}{4} + \frac{\lambda' v_2}{2\sqrt{2}} \right) (\eta_3 \;\; \eta_{1s}) \begin{pmatrix} \frac{v_s}{v_1} & -1 \\ -1 & \frac{v_1}{v_s} \end{pmatrix} \begin{pmatrix} \eta_3 \\ \eta_{1s} \end{pmatrix} , \qquad (4.27)
\end{aligned}
$$

We get three neutral physical scalars, s_1, s_2 and s_{2s} with masses m_{s_1}, m_{s_2}, and $m_{s_{2s}}$, respectively, from the mixing of ρ_1, ρ_2 and ρ_{2s}. The mixing is given by, $\rho = R^{-1}s$, where the mixing matrix can be parametrized with three angle θ_1, θ_2 and θ_3 as follows

$$
R^{-1} = \begin{pmatrix} c_{\theta_1}c_{\theta_3} - c_{\theta_2}s_{\theta_1}s_{\theta_3} & -c_{\theta_1}s_{\theta_3} - c_{\theta_2}c_{\theta_3}s_{\theta_1} & s_{\theta_1}s_{\theta_2} \\ c_{\theta_3}s_{\theta_1} + c_{\theta_1}c_{\theta_2}s_{\theta_3} & c_{\theta_1}c_{\theta_2}c_{\theta_3} - s_{\theta_1}s_{\theta_3} & -c_{\theta_1}s_{\theta_2} \\ s_{\theta_2}s_{\theta_3} & c_{\theta_3}s_{\theta_2} & c_{\theta_2} \end{pmatrix} \equiv \begin{pmatrix} c_{11} & c_{12} & c_{13} \\ c_{21} & c_{22} & c_{23} \\ c_{31} & c_{32} & c_{33} \end{pmatrix} , \qquad (4.28)
$$

where $c_{\theta_i} = \cos\theta_i$ and $s_{\theta_i} = \sin\theta_i$ ($i = 1, 2, 3$). We identify the s_1 as the SM physical Higgs field, $s_1 = h$ with mass m_h. The mixing of the three CP-odd states η_1, η_2, and η_{2s} can be parametrized in a similar way, $\eta = {R'}^{-1}s'$, using three angles θ'_1, θ'_2 and θ'_3. Here, we get one physical neutral pseudoscalar s'_1 with mass $m_{s'_1}$ along with two neutral pseudoscalars Goldstone mode(s''_0 and s'''_0).

The interaction states can be expressed in terms of the mass states as, $\eta_1 = c'_{13}s'_1$, $\eta_2 = c'_{23}s'_1$, and $\eta_{2s} = c'_{33}s'_1$.

We get two more states from the mixing of ρ_3 and ρ_{1s}, one neutral scalar Goldstone mode, s_0 and one neutral physical scalar, s_3 with mass m_{s_3}. The mixing can be parametrized in terms of only one angle, ψ as follows,

$$R_{2\times 2}(\psi) = \begin{pmatrix} \cos\psi & \sin\psi \\ -\sin\psi & \cos\psi \end{pmatrix} . \tag{4.29}$$

Similar mixing and parametrzitation (using angle ψ') occurs for the two CP-odd states η_3 and η_{1s}, where we get one neutral pseudoscalar Goldstone mode, s'_0 and another physical neutral pseudoscalar, s'_3 with mass m_{s_3}. The interaction states can be expressed in terms of the physical states as, $\rho_3 = -\sin\psi s_3$ and $\rho_{1s} = \cos\psi s_3$; $\eta_3 = -\sin\psi' s'_3$ and $\eta_{1s} = \cos\psi' s'_3$.

Therefore we start with 24 scalar degrees of freedom but end up with 18 physical scalars. The rest 6 degrees of freedom, which corresponds to the massless Goldstone mode, are eaten to give mass to the gauge bosons. Hence there are 6 massive gauge bosons and one massless gauge bosons.

In the fermionic sector, the vector-like leptons E_i^- and F_{3i} mix and give two charged physical vector-like leptons as follows,

$$\begin{aligned} f_{1i}^+ &= \cos\theta_f E_i^+ - \sin\theta_f F_{3i}^c \\ f_{2i}^+ &= \sin\theta_f E_i^+ + \cos\theta_f F_{3i}^c \end{aligned} \tag{4.30}$$

respectively with masses $m_{f_{1i}}$ and $m_{f_{2i}}$. The mixing angle, θ_f, can be determined by diagonalizing the mass matrix. All the important physical scalar fields and fermionic fields are summarized in Table. 4.1

Particle type	Particles	Mass parameters	Mass values	Possible final states at LHC
Charged scalars	$h_1^{\pm},\ h_2^{\pm}$	$m_{h_1},\ m_{h_2}$	$m_{h_{1,2}} \sim \mathcal{O}(500)$ GeV	$h_{1,2}^{\pm} \to u_i\bar{d}_j + E_i^0 + E_j^0$, $u_i\bar{d}_j$
	$H_1^{\pm},\ H_2^{\pm}$	$m_{H_1},\ m_{H_2}$	$m_{H_1} \sim \mathcal{O}(500)$ GeV $m_{H_1} \sim \mathcal{O}(5)$ TeV	$H_{1,2}^{\pm} \to u_i\bar{d}_j + \nu_i + E_j^0$, $d_i\bar{d}_j + e_j^- + E_i^0$
Neutral scalars	$h,\ s_2$ $s_{2s},\ s_3$	$m_h,\ m_{s_2}$ $m_{s_{2s}},\ m_{s_3}$	$m_h = 125$ GeV $m_s \sim \mathcal{O}(500)$ GeV	$s_2, s_{2_s} \to e_i^+e_i^-$, $d_i\bar{d}_i$
Neutral pseudoscalar	s_1', s_3'	$m_{s_1'},\ m_{s_3'}$	$m_{s'} \sim \mathcal{O}(500)$ GeV	$s_1', s_3' \to e_i^+e_i^-$, $d_i\bar{d}_i$
Charged vector-like leptons	$f_1^{\pm},\ f_2^{\pm}$	$m_{f_1},\ m_{f_2}$	$m_f \sim \mathcal{O}(100)$ GeV	$f_{1,2i} \to u_i\bar{d}_j + E_i^0$ $d_i\bar{d}_j + e_i^+ + \bar{E}_i^0 + \bar{\nu}_i$
Neutral vector-like leptons	$\bar{E}^0,\ E^0$	$m_{\bar{E}^0},\ m_{E^0}$	$m_{\bar{E}^0} > m_{E^0}$ $\sim \mathcal{O}(100)$GeV	$\bar{E}_i^0 \to e_i^+e_i^- + E_i^0$ $E_i^0 \to \nu_i + n_{1i}\bar{n}_{2j}$
New gauge bosons	$X_1^{\mu},\ X_2^{\mu},\ X_3^{\mu}$	$m_{X_1},\ m_{X_2},\ m_{X_3}$	$m_X \geq 3.6$ TeV	$X_3^{\mu} \to e_i^+e_i^-, d_i\bar{d}_i$ $X_{1,2}^{\mu} \to u_i\bar{d}_j + d_i\bar{u}_j$ $+ \bar{\nu}_i + \bar{E}_i^0$
Charged vector-like quark	D	m_D	$m_D \sim \mathcal{O}(1)$ TeV	$D_i \to e_i^+e_i^- + d_i$ $+\nu_i + E_i$, $d_i\bar{d}_i + d_i + e_i^+e_i^-$

Table 4.1: Summary of the physical scalars, fermions, and the gauge bosons required for the calculations. Here n_1 and n_2 are the viable dark matter candidates in our model . The E^0 decays only to neutral fields leading to a missing energy signal at the LHC.

4.3 Gauge Bosons

In this section, we explore the gauge sector of the model, the gauge boson masses and their interactions with the other particls. First, we define the covariant derivative as,

$$D_\mu I = \partial_\mu I + i\frac{g}{2}\tau_a W_{\mu a} + i\frac{g_2'}{2}\tau_a W'_{\mu a} + ig'YB_\mu I\ , \tag{4.31}$$

where g, g_2' and g' are the coupling constant of $SU(2)_L$, $SU(2)_N$, and $U(1)_Y$ groups respectively. W_μ, W'_μ, and B_μ are the gauge bosons of the $SU(2)_L$, $SU(2)_N$, and $U(1)_Y$ groups respectively.

The gauge boson masses can obtained from the following Lagrangian,

$$\begin{aligned}\mathcal{L}_{gauge-scalar} &= (D_\mu H_u)^\dagger_\alpha (D^\mu H_u)_\alpha + \left(D_\mu H_d^T\right)^\dagger_{\alpha\beta}\left(D^\mu H_d^T\right)_{\beta\alpha} + \left(D_\mu S^{0T}\right)^\dagger_\alpha \left(D^\mu S^{0T}\right)_\alpha \\ &\quad + \left(D_\mu T^T\right)^\dagger_{\alpha\beta}\left(D^\mu T^T\right)_{\beta\alpha} \ , \end{aligned} \tag{4.32}$$

where α and β are the $SU(2)$ indices.

4.3.1 Gauge Boson Masses

In this subsection we calculate the expressions for the gauge boson masses. The massless gauge bosons will become massive after the spontaneous symmetry breaking. The part of Eq. 4.32 that gives gauge boson masses is,

$$\begin{aligned}-\mathcal{L}^{mass}_{gauge} &= \frac{1}{4}g^2(v_1^2+v_2^2)W^-_\mu W^{+\mu} + \frac{1}{4}{g'_2}^2(v_1^2+v_s^2)X_{2\mu}X_1^\mu \\ &+ \frac{1}{8}\left(B_\mu\ W_{3\mu}\ W'_{3\mu}\right)\begin{pmatrix} {g'}^2(v_1^2+v_2^2) & -gg'(v_1^2+v_2^2) & -g'g'_2v_1^2 \\ -gg'(v_1^2+v_2^2) & g^2(v_1^2+v_2^2) & gg'_2v_1^2 \\ -g'g'_2v_1^2 & gg'_2v_1^2 & {g'_2}^2(v_1^2+v_s^2)\end{pmatrix}\begin{pmatrix} B^\mu \\ W_3{}^\mu \\ W_3'^\mu\end{pmatrix}\end{aligned} \tag{4.33}$$

where we have used the definitions, $\sqrt{2}W^\pm_\mu = W_{1\mu} \mp iW_{2\mu}$ and $\sqrt{2}X_{1,2\mu} = W'_{1\mu} \mp iW'_{2\mu}$. The B_μ, $W_{3\mu}$ and $W'_{3\mu}$ fields will mix among themselves and give rise to three physical gauge bosons, which can be written as follows,

$$A_\mu = \sin\theta_W\ W_{3\mu} + \cos\theta_W\ B_\mu \tag{4.34}$$

$$Z_\mu = \cos\theta_N\cos\theta_W\ W_{3\mu} - \cos\theta_N\sin\theta_W\ B_\mu + \sin\theta_N\ W'_{3\mu} \tag{4.35}$$

$$X_{3\mu} = -\sin\theta_N\cos\theta_W\ W_{3\mu} + \sin\theta_N\sin\theta_W\ B_\mu + \cos\theta_N\ W'_{3\mu}\ , \tag{4.36}$$

where the mixing angles are defined as, $\tan\theta_W = \frac{g'}{g}$ and $\tan 2\theta_N = \frac{b}{a_-}$ with the following definitions,

$$b \equiv \frac{1}{8}g'_2\sqrt{g^2+{g'}^2}v_1^2\ , \tag{4.37}$$

$$a_{\pm} \equiv \frac{1}{16}\left[g_2'^2(v_1^2+v_s^2) \pm (g^2+g'^2)(v_1^2+v_2^2)\right] \ . \tag{4.38}$$

There are four more charged physical gauge bosons, $W_\mu^\pm$ and $X_{1,2\mu}$. Therefore, we summarize all the mass squared terms for all six gauge bosons as follows,

$$m_{W^\pm}^2 = \frac{1}{4}g^2(v_1^2+v_2^2) \ , \tag{4.39}$$

$$m_{X_{1,2}}^2 = \frac{1}{4}g_2'^2(v_1^2+v_s^2) \ , \tag{4.40}$$

$$m_A^2 = 0 \ , \tag{4.41}$$

$$m_Z^2 = a_+ - \sqrt{a_-^2+b^2} \ , \tag{4.42}$$

$$m_{X_3}^2 = a_+ + \sqrt{a_-^2+b^2} \ . \tag{4.43}$$

4.3.2 Gauge Boson Interactions

Part of Eq. 4.32, that gives the interactions between the gauge bosons and the physical scalars is given by,

$$\begin{aligned}
\mathcal{L}_{gs}^{int} \ = \ & \frac{1}{2}g_2'^2 X_{2\mu}X_1^\mu\phi_3^+\phi_3^- + \frac{1}{2}g_2'^2 X_{2\mu}X_1^\mu T_2^+T_2^- + \frac{i}{\sqrt{2}}g_2' X_{1\mu}\left(\partial^\mu\phi_1^+\right)\phi_3^- \\
& -\frac{i}{\sqrt{2}}g_2' X_{1\mu}\phi_1^+\left(\partial^\mu\phi_3^-\right) + \frac{i}{\sqrt{2}}g_2' X_{2\mu}\left(\partial^\mu\phi_3^+\right)\phi_1^- - \frac{i}{\sqrt{2}}g_2' X_{2\mu}\phi_3^+\left(\partial^\mu\phi_1^-\right) \\
& +\frac{i}{\sqrt{2}}g_2' X_{1\mu}\left(\partial^\mu T_1^-\right)T_2^+ - \frac{i}{\sqrt{2}}g_2' X_{1\mu}T_1^-\left(\partial^\mu T_2^+\right) + \frac{i}{\sqrt{2}}g_2' X_{2\mu}T_1^+\left(\partial^\mu T_2^-\right) \\
& -\frac{i}{\sqrt{2}}g_2' X_{2\mu}\left(\partial^\mu T_1^+\right)T_2^- + \ldots \ .
\end{aligned} \tag{4.44}$$

In terms of the physical scalar states Eq. 4.44 can be rewritten as,

$$\begin{aligned}\mathcal{L}_{gs}^{int} &= \frac{1}{2}g_2'^2 X_{2\mu}X_1^\mu\left[H_1^+H_1^- + H_2^+H_2^-\right] + \frac{i}{\sqrt{2}}g_2' X_{2\mu}\cos\theta\sin\beta\left[H_1^+(\partial^\mu h_2^-) - (\partial^\mu H_1^+)h_2^-\right] \\ &+\frac{i}{\sqrt{2}}g_2' X_{2\mu}\sin\theta\cos\beta\left[(\partial^\mu H_2^+)h_2^- - H_2^+(\partial^\mu h_2^-)\right] \\ &+\frac{i}{\sqrt{2}}g_2' X_{2\mu}\sin\theta\left[T_1^+(\partial^\mu H_1^-) - (\partial^\mu T_1^+)H_1^-\right] \\ &+\frac{i}{\sqrt{2}}g_2' X_{2\mu}\cos\theta\left[T_1^+(\partial^\mu H_2^-) - (\partial^\mu T_1^+)H_2^-\right] + h.c + \dots . \end{aligned} \tag{4.45}$$

We can derive the necessary Feynman rules from Eq. 4.45. Next, we consider the kinetic energy term of the leptons, L_i and calculate it's interactions with the gauge bosons. Similar calculations can be done for all other fermions.The kinetic term can be written as,

$$\begin{aligned}\mathcal{L}_{kinetic}^{L} &= \left(\bar{L}_i\right)_{\alpha\beta} i\gamma^\mu\left(\partial_\mu I L_i\right)_{\beta\alpha} + \left(\bar{L}_i\right)_{\alpha\beta} i\gamma^\mu\left(\frac{1}{2}ig\tau_a W_{\mu a}L_i\right)_{\beta\alpha} \\ &+\left(\bar{L}_i^T\right)_{\alpha\beta} i\gamma^\mu\left(\frac{1}{2}ig_2'\tau_a W'_{\mu a}L_i^T\right)_{\beta\alpha} - \left(\bar{L}_i\right)_{\alpha\beta} i\gamma^\mu\left(\frac{1}{2}ig' B_\mu I L_i\right)_{\beta\alpha} , \end{aligned} \tag{4.46}$$

where i is the family index; α and β are $SU(2)$ index; and a = 1,2,3. Few important interaction terms we get from Eq. 4.46 are,

$$\mathcal{L}_{kinetic}^{L} = -\frac{1}{\sqrt{2}}g_2' X_{2\mu}\bar{\nu}_i\gamma^\mu E_i^0 - y_{1ij}E_i^0 T_1^+ F_{3j} + y_{2ij}\sin\phi\; E_i^0 h_2^- F_{3j}^c + H.c + \dots . \tag{4.47}$$

4.4 Neutrino Masses

Here we discuss the neutrino mass generation mechanism in our model and the related numerical calculations. The discrete Z_2 symmetry and the particle content of the model ensure that the tree level Lagrangian does not contain neutrino mass terms. So we must rely on the radiatively generated neutrino mass terms. It is also evident that the mass term can not be generated below three-loop level. The dimension-5 effective Majorana neutrino mass operator $L_iL_jH_d^*H_d^*/\mathcal{M}$, where $\mathcal{M}$ is some effective mass scale, in the interaction basis can be generated from the Fig. 4.1.

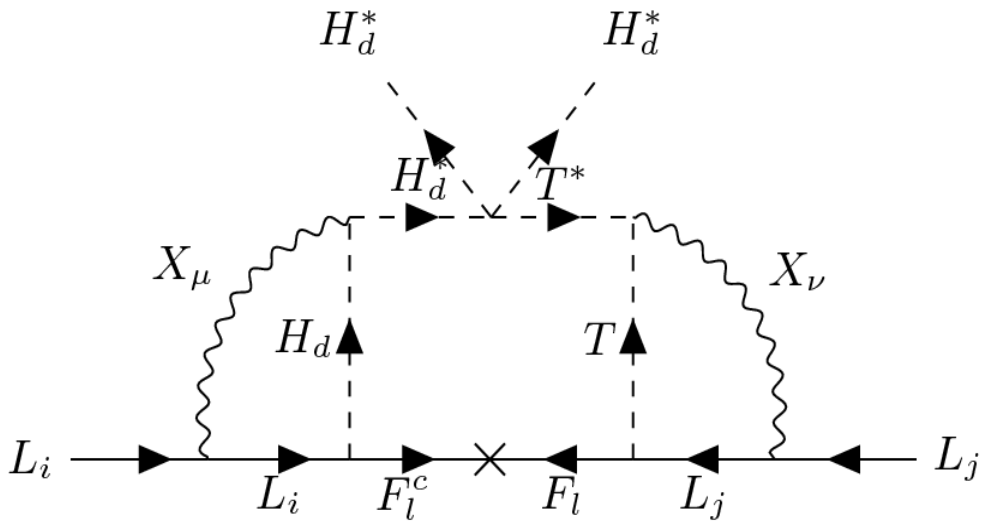

Figure 4.1: The three-loop diagram in the interaction basis that gives rise to the Majorana mass term in our model.

4.4.1 Theoretical Calculations

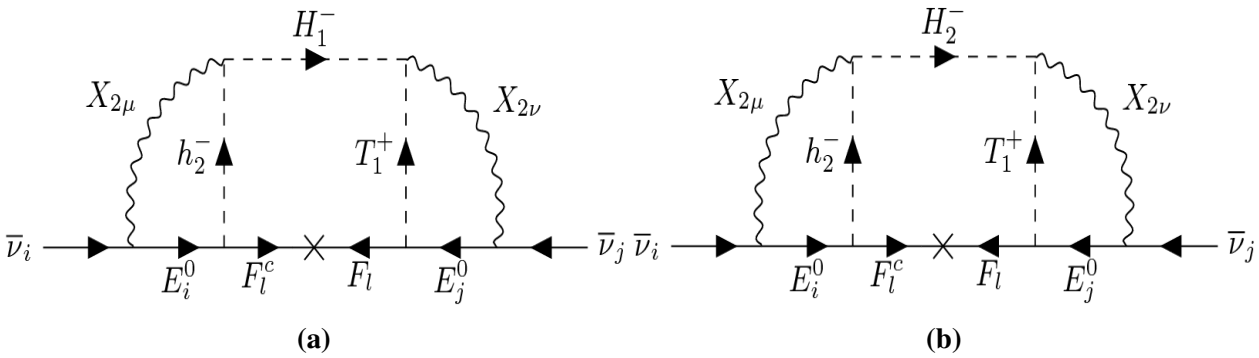

Figure 4.2: The three loop Feynman diagrams in the mass basis responsible for the Majorana neutrino masses. We have two more similar diagrams for the X_1 gauge boson.

The new gauge bosons, X_1 and X_2, associated with the new gauge group $SU(2)_N$ play important role to generate and controll the neutrino masses. The three-loop diagrams in the mass basis are shown in Fig. 4.2, which gives the Majorana mass matrix elements, in unitary gauge, as

follows,

$$(M_\nu)_{ji} = \frac{1}{4} {g'_2}^4 y_{1jl} y_{2li} \sin 2\theta \, \sin^2\beta \times I_{3loop} \, , \tag{4.48}$$

where i, j , l = 1,2,3. The three-loop integral factor, I_{3loop} is given as follows,

$$\begin{aligned} I_{3loop} &= \frac{1}{(16\pi^2)^3 \left(m_X^2 - m_{0j}^2\right) \left(m_X^2 - m_{0i}^2\right) m_X^2} \int_0^\infty dr \frac{r^2}{r + M_l^2} \left[\frac{1}{r + m_{H_1}^2} + \frac{1}{r + m_{H_2}^2} \right] \\ &\times (4 M_l m_{oj} m_{0i} \{ f_h(r, m_X^2, m_{0i}^2, m_{h_2}^2) g_{2T}(r, m_X^2, m_{0j}^2, m_{T_1}^2) \\ &+ f_T(r, m_X^2, m_{0j}^2, m_{T_1}^2) g_{2h}(r, m_X^2, m_{0i}^2, m_{h_2}^2) \\ &- m_X^2 f_h(r, m_X^2, m_{0i}^2, m_{h_2}^2) f_T(r, m_X^2, m_{0j}^2, m_{T_1}^2) \} \\ &+ 2 m_{0j} f_T(r, m_X^2, m_{0j}^2, m_{T_1}^2) \{ g_{4h}(r, m_X^2, m_{0i}^2, m_{h_2}^2) - m_X^2 g_{2h}(r, m_X^2, m_{0i}^2, m_{h_2}^2) \} \\ &- 2 m_{0i} f_h(r, m_X^2, m_{0i}^2, m_{h_2}^2) \{ g_{4T}(r, m_X^2, m_{0j}^2, m_{T_1}^2) \\ &- m_X^2 g_{2T}(r, m_X^2, m_{0j}^2, m_{T_1}^2) \}) \, . \end{aligned} \tag{4.49}$$

The definitions of the various functions are,

$$f_h(r, m_X^2, m_{0i}^2, m_{h_2}^2) = \int_0^1 dx \ln \frac{x(1-x)r + (1-x)m_X^2 + x m_{h_2}^2}{x(1-x)r + (1-x)m_{0i}^2 + x m_{h_2}^2} \, , \tag{4.50}$$

$$f_T(r, m_X^2, m_{0j}^2, m_{T_1}^2) = \int_0^1 dx \ln \frac{x(1-x)r + (1-x)m_X^2 + x m_{T_1}^2}{x(1-x)r + (1-x)m_{0j}^2 + x m_{T_1}^2} \, , \tag{4.51}$$

$$\begin{aligned} g_{2h}(r, m_X^2, m_{0i}^2, m_{h_2}^2) &= m_X^2 \int_0^1 dx \ln \frac{x(1-x)r + (1-x)m_X^2 + x m_{h_2}^2}{m_X^2} \\ &- m_{0i}^2 \int_0^1 dx \ln \frac{x(1-x)r + (1-x)m_{0i}^2 + x m_{h_2}^2}{m_X^2} \, , \end{aligned} \tag{4.52}$$

$$\begin{aligned} g_{2T}(r, m_X^2, m_{0j}^2, m_{T_1}^2) &= m_X^2 \int_0^1 dx \ln \frac{x(1-x)r + (1-x)m_X^2 + x m_{T_1}^2}{m_X^2} \\ &- m_{0j}^2 \int_0^1 dx \ln \frac{x(1-x)r + (1-x)m_{0j}^2 + x m_{T_1}^2}{m_X^2} \, , \end{aligned} \tag{4.53}$$

$$g_{4h}(r, m_X^2, m_{0i}^2, m_{h_2}^2) = m_X^4 \int_0^1 dx \ln \frac{x(1-x)r + (1-x)m_X^2 + xm_{h_2}^2}{m_X^2} - m_{0i}^4 \int_0^1 dx \ln \frac{x(1-x)r + (1-x)m_{0i}^2 + xm_{h_2}^2}{m_X^2}, \quad (4.54)$$

$$g_{4T}(r, m_X^2, m_{0j}^2, m_{T_1}^2) = m_X^4 \int_0^1 dx \ln \frac{x(1-x)r + (1-x)m_X^2 + xm_{T_1}^2}{m_X^2} - m_{0j}^4 \int_0^1 dx \ln \frac{x(1-x)r + (1-x)m_{0j}^2 + xm_{T_1}^2}{m_X^2}. \quad (4.55)$$

Note that, the mass matrix element gets suppressed from the loop factor $\frac{g_2'^4}{(16\pi^2)^3} \sim 10^{-11}$, which plays important role to determine the scale of the new physics scale. Here it can pushes the new physics scale to TeV. In the following subsection we show the numerical calculations which fit the oscillation data in our model.

4.4.2 Numerical Analysis

Here, we want to show that the analytical expression of the neutrino mass matrix can fit the data from the neutrino oscillation experiments. For our calculations, we only consider the normal hierarchy scenarios but similar calculations can be done for the inverted hierarchy scenarios as well. For normal hierarchy, the best fit of the neutrino oscillation data at 3σ level are [297],

$$\begin{aligned}
&\sin^2\theta_{12} = 0.271 - 0.345; \quad \sin^2\theta_{23} = 0.385 - 0.635; \quad \sin^2\theta_{13} = 0.01934 - 0.02392; \\
&\delta_{CP} = 0^\circ - 360^\circ; \\
&\Delta m_{21}^2 = 7.03 \times 10^{-5}\text{eV} - 8.09 \times 10^{-5}\text{eV}; \\
&\Delta m_{31}^2 = 2.407 \times 10^{-3}\text{eV} - 2.643 \times 10^{-3}\text{eV}
\end{aligned} \quad (4.56)$$

We consider the diagonal neutrino mass matrix in mass basis as $M_{d\nu} = \text{diag}(m_1, m_2, m_3)$,

where

$$m_1 \simeq 0 \text{ eV}; m_2 \simeq 8.66 \times 10^{-3} \text{ eV}; m_3 \simeq 4.98 \times 10^{-2} \text{ eV} . \tag{4.57}$$

The Majorana mass matrix is then defined as, $M_\nu = U^{-1} M_{d\nu} U$, where U is the PMNS matrix. We obtain,

$$M_\nu = \begin{pmatrix} 6.35989 \times 10^{-12} & 1.18618 \times 10^{-11} & 1.32647 \times 10^{-11} \\ 1.18618 \times 10^{-11} & 2.3611 \times 10^{-11} & 2.59738 \times 10^{-11} \\ 1.32647 \times 10^{-11} & 2.59738 \times 10^{-11} & 2.86893 \times 10^{-11} \end{pmatrix} \text{ GeV} . \tag{4.58}$$

We present one benchmark scenario which can reproduce the matrix obtained in Eq. 4.58. The parameter point is,

$$\begin{aligned} m_{H_1} &= 5 \text{ TeV}, m_{H_2} = 500 \text{ GeV}, \;\; m_X = 5 \text{ TeV}, \;\; m_{h_2} = 268 \text{ GeV}, \\ m_{T_1} &= 500 \text{ GeV} , \;\; \tan\beta = 50, \;\; v_1/\sqrt{2} = 7 \text{ GeV}, \;\; \theta = 0.005^\circ, \\ m_f &= (110, 120, 130) \text{ GeV}, \;\; m_{E^0} = (105, 110, 115) \text{ GeV} . \end{aligned} \tag{4.59}$$

Note that, we need $y_1 \times y_2$ to be of the order of 0.1 to 0.01 to satisfy the data. Also, the renormalization group evolution suggest that the gauge coupling g_2' is of similar strength to the SM couplings, and we take it to be 0.35.

4.5 The Muon and Elctron Anomalous Magnetic Moment

4.5.1 Background

There is a 3.7σ tension between the theoretical predictions [100, 101, 102, 103] and the experimental results [36, 37] of the anomalous magnetic moment of the muon, given as,

$$\Delta a_\mu = a_\mu^{exp} - a_\mu^{th} = (2.74 \pm .73) \times 10^{-9}. \tag{4.60}$$

And a 2.4σ tension between the experiment [39, 38] and theory [113] values of the anomalous

magnetic moment of electron given by,

$$\Delta a_e = a_e^{exp} - a_e^{th} = (-8.7 \pm 3.6) \times 10^{-13}. \tag{4.61}$$

Note that, the simplest BSM solution where a new mediator couples to both electrons and muons, are expected to give Δa_e and Δa_μ of the same sign, since the new physics couplings would appear twice in each diagram. On the other hand, if one assumes coupling universality then we expect the corrections to scale with the lepton mass, that is $\Delta a_e / \Delta a_\mu \sim m_e^2/m_\mu^2 \sim 2.25 \times 10^{-5}$. As neither of those is true, a more complex solution is required. Here we utilize the diversity of the Yukawa couplings of our model in particular the chiral (different for left-handed and right-handed components) and flavor non-universal (different for each lepton) nature. The chirality of these interactions ensures that certain couplings appear only once in a given diagram, allowing for corrections to a_e and a_μ in opposite directions, while the non-universality allows for modifying each independently of the other.

4.5.2 Calculations and Results

The relevant Yukawa sector Lagrangian is given as,

$$\begin{aligned} -\mathcal{L} \;=\; & \bar{e_i}[C_{S1} + C_{P1}\gamma_5] f_{1i} s_3 + \bar{e_i}[C_{S2} + C_{P2}\gamma_5] f_{2i} s_3 + \bar{e_i}[C_{S3} + C_{P3}\gamma_5] f_{1i} s_3' \\ & + \bar{e_i}[C_{S4} + C_{P4}\gamma_5] f_{2i} s_3' + \bar{e_i}[C_{S5} + C_{P5}\gamma_5] e_i s_2 + \bar{e_i}[C_{S6} + C_{P6}\gamma_5] e_i s_{2s} \\ & + \bar{e_i}[C_{S7} + C_{P7}\gamma_5] e_i s_1' + \bar{e_i}[C_{S8} + C_{P8}\gamma_5] E_i^0 H_1^- + \bar{e_i}[C_{S9} + C_{P9}\gamma_5] E_i^0 H_2^- \\ & + \bar{e_i}[C_{S10} + C_{P10}\gamma_5] \nu_i h_1^- + \bar{e_i}[C_{S11} + C_{P11}\gamma_5] \nu_i h_2^- + \text{H.C.}\,, \end{aligned} \tag{4.62}$$

where the various couplings are defined as follows,

$$C_{S1} = \frac{1}{2\sqrt{2}} (y_{8i} \sin\psi \cos\theta_f - y_{2i} \sin\psi \sin\theta_f + y_{6i} \cos\psi \cos\theta_f), \tag{4.63}$$

$$C_{P1} = \frac{1}{2\sqrt{2}} (y_{8i} \sin\psi \cos\theta_f - y_{2i} \sin\psi \sin\theta_f + y_{6i} \cos\psi \cos\theta_f), \tag{4.64}$$

$$C_{S2} = \frac{1}{2\sqrt{2}}(y_{8i}\sin\psi\cos\theta_f - y_{2i}\sin\psi\sin\theta_f + y_{6i}\cos\psi\cos\theta_f), \tag{4.65}$$

$$C_{P2} = \frac{1}{2\sqrt{2}}(y_{8i}\sin\psi\cos\theta_f - y_{2i}\sin\psi\sin\theta_f + y_{6i}\cos\psi\cos\theta_f), \tag{4.66}$$

$$C_{S3} = \frac{1}{2\sqrt{2}}(y_{8i}\sin\psi\cos\theta_f - y_{2i}\sin\psi\sin\theta_f + y_{6i}\cos\psi\cos\theta_f), \tag{4.67}$$

$$C_{P3} = \frac{1}{2\sqrt{2}}(y_{8i}\sin\psi\cos\theta_f - y_{2i}\sin\psi\sin\theta_f + y_{6i}\cos\psi\cos\theta_f), \tag{4.68}$$

$$C_{S4} = \frac{1}{2\sqrt{2}}(y_{8i}\sin\psi\cos\theta_f - y_{2i}\sin\psi\sin\theta_f + y_{6i}\cos\psi\cos\theta_f), \tag{4.69}$$

$$C_{P4} = \frac{1}{2\sqrt{2}}(y_{8i}\sin\psi\cos\theta_f - y_{2i}\sin\psi\sin\theta_f + y_{6i}\cos\psi\cos\theta_f), \tag{4.70}$$

$$C_{S5} = \frac{1}{2\sqrt{2}}y_{8i}c_{12} = -C_{P5};\ C_{S6} = \frac{1}{2\sqrt{2}}y_{8i}c_{13} = -C_{P6}, \tag{4.71}$$

$$C_{S7} = \frac{i}{2\sqrt{2}}y_{8i}c'_{13} = -C_{P7};\ C_{S8} = \frac{1}{2}y_{8i}\cos\theta = -C_{P8}, \tag{4.72}$$

$$C_{S9} = -\frac{1}{2}y_{8i}\sin\theta = -C_{P9};\ C_{S10} = -\frac{1}{2}y_{8i}\cos\beta = -C_{P10}, \tag{4.73}$$

$$C_{S11} = \frac{1}{2}y_{8i}\sin\beta = -C_{P11}\ . \tag{4.74}$$

where the couplings C_{S1}-C_{P11} are linear combinations of three Yukawa couplings y_2, y_6, and y_8. This will give rise to products of two different Yukawa couplings in various diagrams. Note that we have exactly 11 one-loop Feynman diagrams generating from Eq. 4.62. We show them in Fig. 4.3

We broadly categorize the Feynman diagrams of Fig. 4.3 into two category: ones with a neutral scalar inside the loop and ones with a charged scalar. Each of them can be written in the general form

$$-\mathcal{L} = \bar{e_i}[C_S + C_P\gamma_5]f_i s\ , \tag{4.75}$$

where f denotes the fermion and S the scalar that run in the loop.

The contribution from the first type of diagrams with a neutral scalar can be written as [131]

$$\Delta a_{ei}^{1}(C_S, C_P, m_{fi}, m_s) = \frac{-q_{f_i} m_{ei}^2}{8\pi^2} \int_0^1 dx \frac{\left[C_S^2 \left(x^2 - x^3 + \frac{m_{fi}}{m_{ei}} x^2\right) + C_P^2 \left(m_{fi} \to -m_{fi}\right)\right]}{m_{ei}^2 x^2 + (m_{fi}^2 - m_{ei}^2)x + m_s^2(1-x)}, \tag{4.76}$$

and the contribution of the second type of diagrams with charged scalar can be written as

$$\Delta a_{ei}^{2}(C_S, C_P, m_{fi}, m_s) = \frac{-q_h m_{ei}^2}{8\pi^2} \int_0^1 dx \frac{\left[C_S^2 \left(x^2 - x^3 + \frac{m_{fi}}{m_{ei}} (x^2 - x)\right) + C_P^2 \left(m_{fi} \to -m_{fi}\right)\right]}{m_{ei}^2 x^2 + (m_s^2 - m_{ei}^2)x + m_{fi}^2(1-x)} \tag{4.77}$$

In the following we discuss how the various diagrams contribute to Δa_{ei}.

- Fig. 4.3a shows four diagrams where we have the vector-like leptons $f_{1,2}$ and the new neutral scalar particles s_3 and s_3' inside the loop. Their contributions to Δa_{ei} is given by Eq. 4.76. Here we get quadratic terms in the Yukawa couplings ($y_{2i}^2,\ y_{6i}^2$ and y_{8i}^2) as well as cross terms ($y_{2i} \times y_{8i}$, $y_{2i} \times y_{6i}$ and $y_{6i} \times y_{8i}$). The quadratic terms are all proportional to m_{ei}^2 and the cross terms are proportional to $m_{fi} \times m_{ei}$. With a fermion mass $m_{fi} \sim 100$ GeV, the cross terms can give contributions that are both large and of opposite signs for the muon and electron cases.

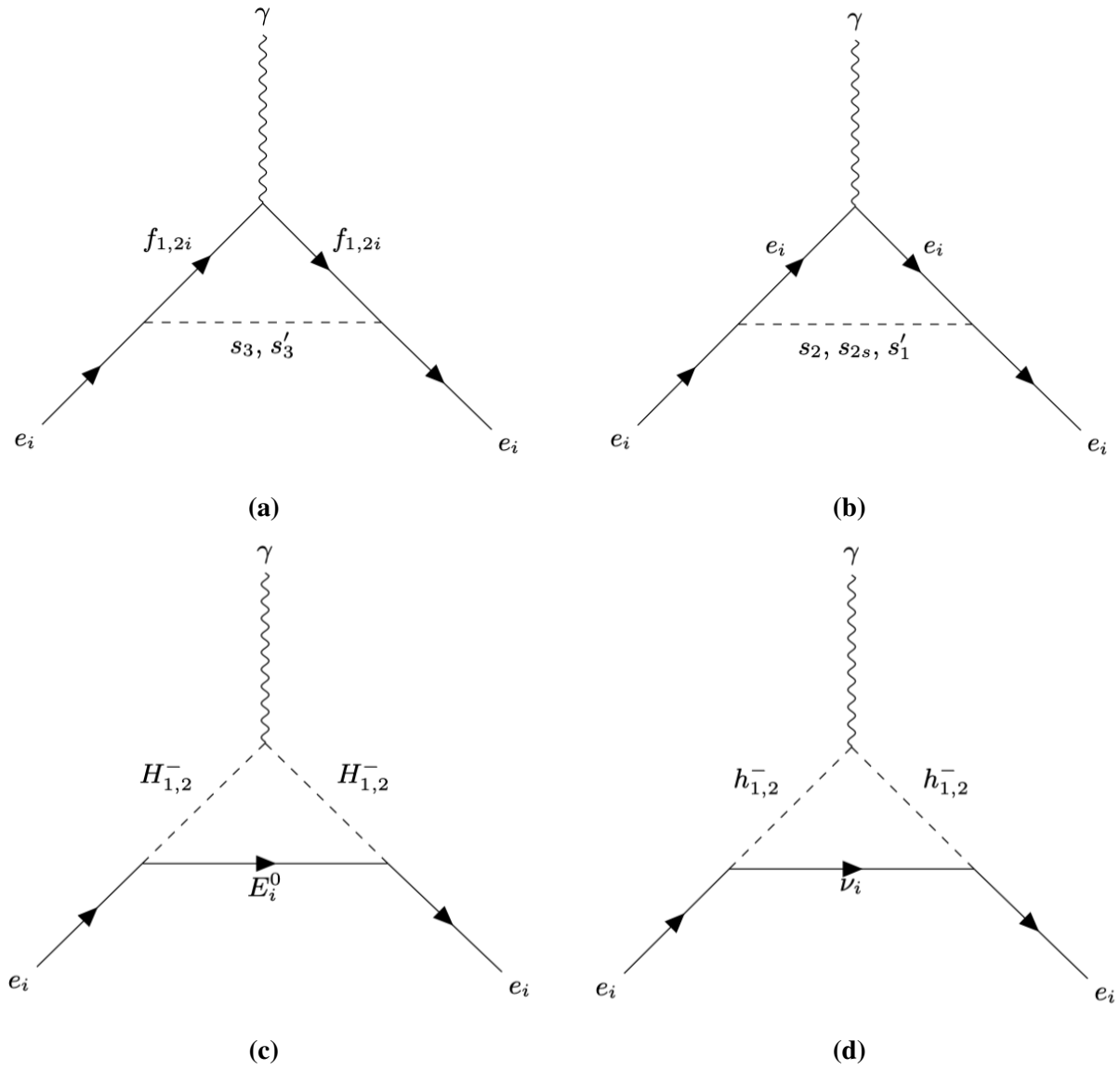

Figure 4.3: The one loop Feynman diagrams in the mass basis which contributes to the anomalous magnetic moments of the muon and electrons.

- The next three diagrams shown in Fig. 4.3b with the new neutral scalars $s_2,\ s_{2s}$ and s_1' inside the loop along with the SM muons and electrons are proportional to the SM Yukawa couplings, y_{8i}^2, and hence suppressed by m_{ei}^2. Therefore, their contribution to Δa_{ei} is small compared to the contributions of the first four diagrams. Therefore the masses of the scalars involved are thus far not fixed.

- Fig. 4.3c and 4.3d give four more diagrams with charged scalars ($H_{1,2}^{\pm}$ and $h_{1,2}^{\pm}$) and neutral fermions such as E_i^0 and ν_i inside the loop. Their contributions to Δa_{ei} are also suppressed compared to the diagrams with cross terms as they are also proportional to y_{8i}^2. Moreover, as these particles also enter into the three-loop diagrams (Fig. 4.2) needed for neutrino mass generation, their masses are already fixed in our model, and so they do not play important roles in the Δa_{ei} calculations.

- In addition to these 11 scalar loop diagrams we do get contributions from the one loop diagrams with gauge bosons associated with the new gauge group $SU(2)_N$. The lower limit on the new gauge boson masses is given by $\sim$ 3.6 TeV [298, 299, 300] assuming the gauge coupling g_2' to be 0.35. These contributions to Δa_{ei} are also suppressed by the square of lepton masses and their contributions can be neglected.

For completeness we consider the contributions from all the 11 Feynman diagrams to Δa_{ei} and can be expressed in a simple form as follows,

$$\begin{aligned}
\Delta a_{ei} \;=\; & \Delta a^1_{ei}(C_{S1}, C_{P1}, m_{f_{1i}}, m_{s_3}) + \Delta a^1_{ei}(C_{S2}, C_{P2}, m_{f_{2i}}, m_{s_3}) + \Delta a^1_{ei}(C_{S3}, C_{P3}, m_{f_{1i}}, m_{s_3'}) \\
& + \Delta a^1_{ei}(C_{S4}, C_{P4}, m_{f_{2i}}, m_{s_3'}) + \Delta a^1_{ei}(C_{S5}, m_{ei}, m_{s_2}) + \Delta a^1_{ei}(C_{S6}, m_{ei}, m_{s_{2s}}) \\
& + \Delta a^1_{ei}(C_{S7}, m_{ei}, m_{s_1'}) + \Delta a^2_{ei}(C_{S8}, C_{P8}, m_{E_i^0}, m_{H_1}) + \Delta a^2_{ei}(C_{S9}, C_{P9}, m_{E_i^0}, m_{H_2}) \\
& + \Delta a^2_{ei}(C_{S10}, C_{P10}, m_{\nu i}, m_{h1}) + \Delta a^2_{ei}(C_{S11}, C_{P11}, m_{\nu i}, m_{h2})\ . \qquad (4.78)
\end{aligned}$$

To find a viable parameter space, we start by setting the dimensionless parameters that are not yet set by the neutrino mass and then vary the mass parameters. The y_8's are fixed by the SM

charged lepton masses, $m_{ei} = y_{8i}v_1/\sqrt{2}$, and we set them to be $y_{8e} = -7 \times 10^{-5}$, $y_{8\mu} = 0.015$ and $y_{8\tau} = 0.25$. Other important coupling constants are: $y_{2e} = 0.80$, $y_{6e} = 2.50$, $y_{2\mu} = 0.50$ and $y_{6\mu} = 0.25$. We choose the mixing angles ψ, ψ' θ_f, $\theta_{1,2,3}$ and $\theta'_{1,2,3}$ to be 45° for simplicity. We now vary the masses of the fermions and the scalars, $f_{1,2}$, s_3 and s'_3, that play important role in the Δa_i calculations and show such five benchmark in Table. 4.2.

Benchmark Point	m_{f1} (GeV)	m_{f2} (GeV)	m_{s3} (GeV)	$m_{s'_3}$ (GeV)
BP1	120	121	350	1985
BP2	120	135	350	1121
BP3	120	102	350	1578
BP4	120	118	350	570
BP5	120	145	350	2150

Table 4.2: Five Benchmark points are shown which can account for Δa_{ei} as well as be consistent with neutrino mass calculations.

We perform a random scan over some of the parameters going into the $g-2$ calculation to check how well the model can fits the results. We limit the scan to a subset of four parameters and fix the other parameters. For example, the diagrams in Fig. 4.3 shows that the dependence on m_{f_1} and m_{s_3} is similar to that on m_{f_2} and $m_{s'_3}$ respectively, therefore, we fix the former and scan over the latter. Similarly we fix $y_{2e,\mu}$ and vary $y_{6e,\mu}$. The ranges of the parameters used in the scan is shown in Table. 4.3

We sample 100,000 points at random from the range of the parameters shown in Table 4.3 with the fixed parameters as y_{2e} = 0.9, $y_{2\mu}$ = 0.5,m_{f_1}= 120 GeV and m_{s_3} = 350 GeV. In Fig. 4.4 we show the results of the scan as a scatter plot in the $\Delta a_\mu - \Delta a_e$ plane along with the 1 σ bands and find that about 2800 points fell into the intersection of the two bands. We also find that while a wide range of Δa_μ can be achieved, the values of Δa_e mostly lie on the upper end of the band.

Parameter	Range
y_{6e}	0.6-3.0
$y_{6\mu}$	0.001-2.0
m_{f_2}	100-150 GeV
$m_{s_3'}$	300-2500 GeV

Table 4.3: The scan range, are shown for the parameters, used to generate Fig. 4.4. The fixed parameters are: $y_{2e} = 0.9$, $y_{2\mu} = 0.5$, $m_{f_1} = 120$ GeV and $m_{s_3} = 350$ GeV.

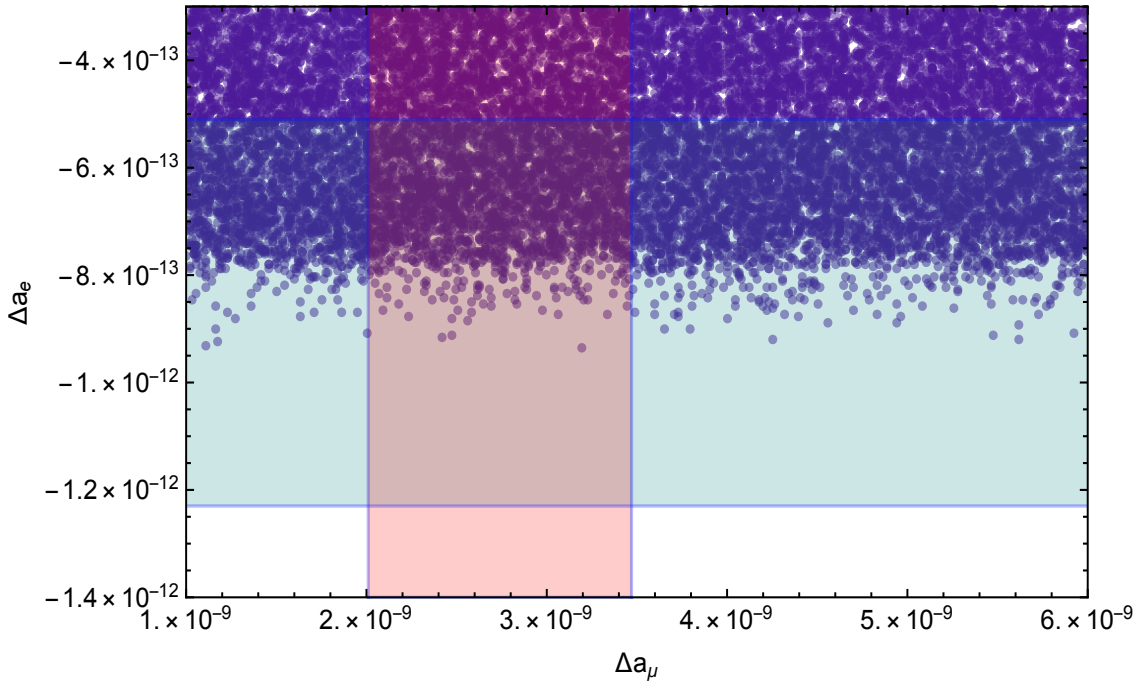

Figure 4.4: A scatter plot in the $\Delta a_\mu - \Delta a_e$ plane: we show about 16,800 points from a scan 100,000 parameter points randomly selected from the range shown in Table. 4.3. The bands represents the 1σ deviation. 2,773 points fall into the interaction of the two bands.

4.6 Conclusions

In this chapter, we build a new physics model with energy scale at TeV, thus can be probed by the current and proposed collider experiments. In addition to the theoretical appeal of fitting into a unification scenario, the model has the potential to generate correct neutrino mass and mixings radiatively at the three-loop level. The model can also explain the observed values of the anomalous magnetic moment of muon and electron. The interesting flavor structure of the model, which also allowed the neutrino fit, plays a crucial role to calculate the contributions to the anomalous magnetic moments.

To explain all the above observables, we introduce a bunch of new particles in the range of 100 GeV to 1 TeV. All of these particles are allowed by the current LHC constraints. One reason they have not been ruled out by LHC is that there is mass degeneracy between the particles and one of their decay products. This can be a good motivation for LHC to close the mass gap by getting more data.

5. SUMMARY AND CONCLUSIONS

The main motivation of this thesis is to understand a problem of neutrino mass and its mixings and the observation of the astronomical dark matter. These are the most interesting and compelling puzzles of the SM. Though the SM is a highly successful theoretical model of elementary particle physics to explain various experimental data at $\mathcal{O}$(100 GeV), with solid experimental evidence, it cannot accommodate the neutrino mass and the origin of the dark matter. Therefore any new physics model that is an extension of the SM should incorporate them. Besides them, a few more puzzles are coming from the experimental data.

In this thesis, we tried to link these experimental puzzles to a complete model of (a) neutrino mass and its mixings and (b) nature of the dark matter.. For that purpose, we have proposed three different models by extending the SM. The first model is a low energy model with a light scalar of mass $\sim \mathcal{O}(100)$ MeV. This model can produce correct neutrino mass using the type-I seesaw mechanism and can give correct dark matter relic density using the Shi-Fuller mechanism. The light scalar plays a crucial role to explain the anomalous magnetic moment of electron and muon, excess events observed by the MiniBooNE experiment, and KOTO excess events simultaneously. The main idea behind the second model was to get a sub-GeV dark matter model. We utilize the gauge group $U(1)_{T3R}$ to connect the new dark sector physics to the light flavor sector of SM and obtain the sub-GeV particles with a symmetry breaking scale of 10 GeV. The model has interesting direct detection prospects and can obtain correct thermal relic density by evading Planck bounds. The parameter space is tightly constrained, but open parameter space is available and has the potential to explain the recently confirmed flavor anomalies in the B-meson decay processes. The third model was proposed to generate neutrino mass radiatively at the three-loop level to bring down the new physics scale associated with to TeV scale. Therefore this model can be probed at the current/upcoming collider experiments. The interesting flavor structure of this model has the potential to explain the anomalous magnetic moment of both muon and electron.

All of these models can be further probed at the upcoming/future experiments or with more

data from the current experiments. I hope that this thesis will help us to understand SM and its extensions more robustly.

REFERENCES

[1] Bhaskar Dutta, Sumit Ghosh, and Jason Kumar. Contributions to ΔN_{eff} from the dark photon of $U(1)_{T3R}$. *Phys. Rev. D*, 102(1):015013, 2020.

[2] Roni Harnik, Joachim Kopp, and Pedro A.N. Machado. Exploring nu Signals in Dark Matter Detectors. *JCAP*, 07:026, 2012.

[3] Javier Redondo. Helioscope Bounds on Hidden Sector Photons. *JCAP*, 07:008, 2008.

[4] Robert Bollig, William DeRocco, Peter W. Graham, and Hans-Thomas Janka. Muons in supernovae: implications for the axion-muon coupling. 5 2020.

[5] Djuna Croon, Gilly Elor, Rebecca K. Leane, and Samuel D. McDermott. Supernova Muons: New Constraints on Z' Bosons, Axions, and ALPs. 6 2020.

[6] Bernard Aubert et al. Search for Dimuon Decays of a Light Scalar Boson in Radiative Transitions Upsilon —> gamma A0. *Phys. Rev. Lett.*, 103:081803, 2009.

[7] J.P. Lees et al. Search for a Dark Photon in e^+e^- Collisions at BaBar. *Phys. Rev. Lett.*, 113(20):201801, 2014.

[8] Martin Bauer, Patrick Foldenauer, and Joerg Jaeckel. Hunting All the Hidden Photons. *JHEP*, 18:094, 2020.

[9] E.M. Riordan et al. A Search for Short Lived Axions in an Electron Beam Dump Experiment. *Phys. Rev. Lett.*, 59:755, 1987.

[10] J.D. Bjorken, S. Ecklund, W.R. Nelson, A. Abashian, C. Church, B. Lu, L.W. Mo, T.A. Nunamaker, and P. Rassmann. Search for Neutral Metastable Penetrating Particles Produced in the SLAC Beam Dump. *Phys. Rev. D*, 38:3375, 1988.

[11] James D. Bjorken, Rouven Essig, Philip Schuster, and Natalia Toro. New Fixed-Target Experiments to Search for Dark Gauge Forces. *Phys. Rev. D*, 80:075018, 2009.

[12] M. Davier and H. Nguyen Ngoc. An Unambiguous Search for a Light Higgs Boson. *Phys. Lett. B*, 229:150–155, 1989.

[13] S.N. Gninenko, N.V. Krasnikov, and V.A. Matveev. Muon g-2 and searches for a new leptophobic sub-GeV dark boson in a missing-energy experiment at CERN. *Phys. Rev. D*, 91:095015, 2015.

[14] Michael Bordag, U. Mohideen, and V.M. Mostepanenko. New developments in the Casimir effect. *Phys. Rept.*, 353:1–205, 2001.

[15] Akitaka Ariga et al. FASER: ForwArd Search ExpeRiment at the LHC. 1 2019.

[16] Asher Berlin, Stefania Gori, Philip Schuster, and Natalia Toro. Dark Sectors at the Fermilab SeaQuest Experiment. *Phys. Rev. D*, 98(3):035011, 2018.

[17] D. Akimov et al. Observation of Coherent Elastic Neutrino-Nucleus Scattering. *Science*, 357(6356):1123–1126, 2017.

[18] D. Akimov et al. COHERENT Collaboration data release from the first observation of coherent elastic neutrino-nucleus scattering. 4 2018.

[19] D. Akimov et al. COHERENT 2018 at the Spallation Neutron Source. 3 2018.

[20] D. Akimov et al. Sensitivity of the COHERENT Experiment to Accelerator-Produced Dark Matter. 11 2019.

[21] D. Akimov et al. First Detection of Coherent Elastic Neutrino-Nucleus Scattering on Argon. 3 2020.

[22] C. Amsler et al. Search for a new light gauge boson in decays of pi0 and eta. *Phys. Lett. B*, 333:271–276, 1994.

[23] Claude Amsler et al. Search for a new light gauge boson in pi0, eta and eta-prime decays. *Z. Phys. C*, 70:219–226, 1996.

[24] Chien-Yi Chen, Maxim Pospelov, and Yi-Ming Zhong. Muon Beam Experiments to Probe the Dark Sector. *Phys. Rev. D*, 95(11):115005, 2017.

[25] S.N. Gninenko, D.V. Kirpichnikov, M.M. Kirsanov, and N.V. Krasnikov. Combined search for light dark matter with electron and muon beams at NA64. *Phys. Lett. B*, 796:117–122, 2019.

[26] Yonatan Kahn, Gordan Krnjaic, Nhan Tran, and Andrew Whitbeck. M^3: a new muon missing momentum experiment to probe $(g-2)_\mu$ and dark matter at Fermilab. *JHEP*, 09:153, 2018.

[27] Asher Berlin, Nikita Blinov, Gordan Krnjaic, Philip Schuster, and Natalia Toro. Dark Matter, Millicharges, Axion and Scalar Particles, Gauge Bosons, and Other New Physics with LDMX. *Phys. Rev. D*, 99(7):075001, 2019.

[28] Gerard Jungman, Marc Kamionkowski, and Kim Griest. Supersymmetric dark matter. *Phys. Rept.*, 267:195–373, 1996.

[29] Douglas Clowe, Marusa Bradac, Anthony H. Gonzalez, Maxim Markevitch, Scott W. Randall, Christine Jones, and Dennis Zaritsky. A direct empirical proof of the existence of dark matter. *Astrophys. J. Lett.*, 648:L109–L113, 2006.

[30] P.A. Zyla et al. Review of Particle Physics. *PTEP*, 2020(8):083C01, 2020.

[31] Nathalie Palanque-Delabrouille et al. The one-dimensional Ly-alpha forest power spectrum from BOSS. *Astron. Astrophys.*, 559:A85, 2013.

[32] N. Aghanim et al. Planck 2018 results. VI. Cosmological parameters. 2018.

[33] Y. Fukuda et al. Evidence for oscillation of atmospheric neutrinos. *Phys. Rev. Lett.*, 81:1562–1567, 1998.

[34] Q. R. Ahmad et al. Direct evidence for neutrino flavor transformation from neutral current interactions in the Sudbury Neutrino Observatory. *Phys. Rev. Lett.*, 89:011301, 2002.

[35] P.F. de Salas, D.V. Forero, C.A. Ternes, M. Tortola, and J.W.F. Valle. Status of neutrino oscillations 2018: 3σ hint for normal mass ordering and improved CP sensitivity. *Phys. Lett. B*, 782:633–640, 2018.

[36] G. W. Bennett et al. Final Report of the Muon E821 Anomalous Magnetic Moment Measurement at BNL. *Phys. Rev.*, D73:072003, 2006.

[37] M. Tanabashi et al. Review of Particle Physics. *Phys. Rev.*, D98(3):030001, 2018.

[38] D. Hanneke, S. Fogwell Hoogerheide, and G. Gabrielse. Cavity Control of a Single-Electron Quantum Cyclotron: Measuring the Electron Magnetic Moment. *Phys. Rev.*, A83:052122, 2011.

[39] D. Hanneke, S. Fogwell, and G. Gabrielse. New Measurement of the Electron Magnetic Moment and the Fine Structure Constant. *Phys. Rev. Lett.*, 100:120801, 2008.

[40] S. Shinohara. *Search for the rare decay $K_L \to \pi^0\bar{\nu}\nu$ at JPARC KOTO experiment*, September 2019. KAON2019, Perugia, Italy.

[41] C. Lin. *Recent Result on the Measurement of $K_L \to \pi^0\nu\bar{\nu}$ at the J-PARC KOTO Experiment*, September 2019. J-PARC Symposium.

[42] Andrzej J. Buras, Dario Buttazzo, Jennifer Girrbach-Noe, and Robert Knegjens. $K^+ \to \pi^+\nu\overline{\nu}$ and $K_L \to \pi^0\nu\overline{\nu}$ in the Standard Model: status and perspectives. *JHEP*, 11:033, 2015.

[43] A.A. Aguilar-Arevalo et al. Significant Excess of ElectronLike Events in the MiniBooNE Short-Baseline Neutrino Experiment. *Phys. Rev. Lett.*, 121(22):221801, 2018.

[44] A.A. Aguilar-Arevalo et al. Updated MiniBooNE Neutrino Oscillation Results with Increased Data and New Background Studies. 6 2020.

[45] Peter W. Higgs. Broken Symmetries and the Masses of Gauge Bosons. *Phys. Rev. Lett.*, 13:508–509, 1964.

[46] Peter W. Higgs. Spontaneous Symmetry Breakdown without Massless Bosons. *Phys. Rev.*, 145:1156–1163, 1966.

[47] F. Englert and R. Brout. Broken Symmetry and the Mass of Gauge Vector Mesons. *Phys. Rev. Lett.*, 13:321–323, 1964.

[48] G.S. Guralnik, C.R. Hagen, and T.W.B. Kibble. Global Conservation Laws and Massless Particles. *Phys. Rev. Lett.*, 13:585–587, 1964.

[49] T.W.B. Kibble. Symmetry breaking in nonAbelian gauge theories. *Phys. Rev.*, 155:1554–1561, 1967.

[50] T.D. Lee. A Theory of Spontaneous T Violation. *Phys. Rev. D*, 8:1226–1239, 1973.

[51] G.C. Branco, P.M. Ferreira, L. Lavoura, M.N. Rebelo, Marc Sher, and Joao P. Silva. Theory and phenomenology of two-Higgs-doublet models. *Phys. Rept.*, 516:1–102, 2012.

[52] Xiao-Gang He, Tong Li, Xue-Qian Li, Jusak Tandean, and Ho-Chin Tsai. Constraints on Scalar Dark Matter from Direct Experimental Searches. *Phys. Rev. D*, 79:023521, 2009.

[53] B. Grzadkowski and P. Osland. Tempered Two-Higgs-Doublet Model. *Phys. Rev. D*, 82:125026, 2010.

[54] Heather E. Logan. Dark matter annihilation through a lepton-specific Higgs boson. *Phys. Rev. D*, 83:035022, 2011.

[55] M.S. Boucenna and S. Profumo. Direct and Indirect Singlet Scalar Dark Matter Detection in the Lepton-Specific two-Higgs-doublet Model. *Phys. Rev. D*, 84:055011, 2011.

[56] Xiao-Gang He, Bo Ren, and Jusak Tandean. Hints of Standard Model Higgs Boson at the LHC and Light Dark Matter Searches. *Phys. Rev. D*, 85:093019, 2012.

[57] Yang Bai, Vernon Barger, Lisa L. Everett, and Gabe Shaughnessy. Two-Higgs-doublet-portal dark-matter model: LHC data and Fermi-LAT 135 GeV line. *Phys. Rev. D*, 88:015008, 2013.

[58] Xiao-Gang He and Jusak Tandean. Low-Mass Dark-Matter Hint from CDMS II, Higgs Boson at the LHC, and Darkon Models. *Phys. Rev. D*, 88:013020, 2013.

[59] Yi Cai and Tong Li. Singlet dark matter in a type II two Higgs doublet model. *Phys. Rev. D*, 88(11):115004, 2013.

[60] Jun Guo and Zhaofeng Kang. Higgs Naturalness and Dark Matter Stability by Scale Invariance. *Nucl. Phys. B*, 898:415–430, 2015.

[61] Lei Wang and Xiao-Fang Han. A simplified 2HDM with a scalar dark matter and the galactic center gamma-ray excess. *Phys. Lett. B*, 739:416–420, 2014.

[62] Aleksandra Drozd, Bohdan Grzadkowski, John F. Gunion, and Yun Jiang. Extending two-Higgs-doublet models by a singlet scalar field - the Case for Dark Matter. *JHEP*, 11:105, 2014.

[63] Robyn Campbell, Stephen Godfrey, Heather E. Logan, Andrea D. Peterson, and Alexandre Poulin. Implications of the observation of dark matter self-interactions for singlet scalar dark matter. *Phys. Rev. D*, 92(5):055031, 2015. [Erratum: Phys.Rev.D 101, 039905 (2020)].

[64] Aleksandra Drozd, Bohdan Grzadkowski, John F. Gunion, and Yun Jiang. Isospin-violating dark-matter-nucleon scattering via two-Higgs-doublet-model portals. *JCAP*, 10:040, 2016.

[65] Stefan von Buddenbrock, Nabarun Chakrabarty, Alan S. Cornell, Deepak Kar, Mukesh Kumar, Tanumoy Mandal, Bruce Mellado, Biswarup Mukhopadhyaya, Robert G. Reed, and Xifeng Ruan. Phenomenological signatures of additional scalar bosons at the LHC. *Eur. Phys. J. C*, 76(10):580, 2016.

[66] Margarete Muhlleitner, Marco O. P. Sampaio, Rui Santos, and Jonas Wittbrodt. The N2HDM under Theoretical and Experimental Scrutiny. *JHEP*, 03:094, 2017.

[67] Xuewen Liu, Ligong Bian, Xue-Qian Li, and Jing Shu. Type-III two Higgs doublet model plus a pseudoscalar confronted with $h \to \mu\tau$, muon $g-2$ and dark matter. *Nucl. Phys. B*, 909:507–524, 2016.

[68] Howard Georgi and Dimitri V. Nanopoulos. Suppression of Flavor Changing Effects From Neutral Spinless Meson Exchange in Gauge Theories. *Phys. Lett. B*, 82:95–96, 1979.

[69] F.J. Botella and Joao P. Silva. Jarlskog - like invariants for theories with scalars and fermions. *Phys. Rev. D*, 51:3870–3875, 1995.

[70] L. Lavoura and Joao P. Silva. Fundamental CP violating quantities in a SU(2) x U(1) model with many Higgs doublets. *Phys. Rev. D*, 50:4619–4624, 1994.

[71] John F. Donoghue and Ling Fong Li. Properties of Charged Higgs Bosons. *Phys. Rev. D*, 19:945, 1979.

[72] L. Lavoura. Signatures of discrete symmetries in the scalar sector. *Phys. Rev. D*, 50:7089–7092, 1994.

[73] Peter Minkowski. $\mu \to e\gamma$ at a Rate of One Out of 10^9 Muon Decays? *Phys. Lett. B*, 67:421–428, 1977.

[74] Tsutomu Yanagida. Horizontal gauge symmetry and masses of neutrinos. *Conf. Proc. C*, 7902131:95–99, 1979.

[75] Murray Gell-Mann, Pierre Ramond, and Richard Slansky. Complex Spinors and Unified Theories. *Conf. Proc. C*, 790927:315–321, 1979.

[76] Rabindra N. Mohapatra and Goran Senjanovic. Neutrino Mass and Spontaneous Parity Nonconservation. *Phys. Rev. Lett.*, 44:912, 1980.

[77] Kazuyuki Kanaya. Neutrino Mixing in the Minimal SO(10) Model. *Progress of Theoretical Physics*, 64(6):2278–2281, 12 1980.

[78] J. Schechter and J.W.F. Valle. Neutrino Decay and Spontaneous Violation of Lepton Number. *Phys. Rev. D*, 25:774, 1982.

[79] G.C. Branco, J.T. Penedo, Pedro M.F. Pereira, M.N. Rebelo, and J.I. Silva-Marcos. Type-I Seesaw with eV-Scale Neutrinos. *JHEP*, 07:164, 2020.

[80] Palash B. Pal and Lincoln Wolfenstein. Radiative Decays of Massive Neutrinos. *Phys. Rev. D*, 25:766, 1982.

[81] Vernon D. Barger, R.J.N. Phillips, and Subir Sarkar. Remarks on the KARMEN anomaly. *Phys. Lett. B*, 352:365–371, 1995. [Erratum: Phys.Lett.B 356, 617–617 (1995)].

[82] Scott Dodelson and Lawrence M. Widrow. Sterile-neutrinos as dark matter. *Phys. Rev. Lett.*, 72:17–20, 1994.

[83] Alexander Kusenko. Sterile neutrinos: The Dark side of the light fermions. *Phys. Rept.*, 481:1–28, 2009.

[84] A. Boyarsky, M. Drewes, T. Lasserre, S. Mertens, and O. Ruchayskiy. Sterile Neutrino Dark Matter. *Prog. Part. Nucl. Phys.*, 104:1–45, 2019.

[85] Xiang-Dong Shi and George M. Fuller. A New dark matter candidate: Nonthermal sterile neutrinos. *Phys. Rev. Lett.*, 82:2832–2835, 1999.

[86] S.P. Mikheyev and A.Yu. Smirnov. Resonance Amplification of Oscillations in Matter and Spectroscopy of Solar Neutrinos. *Sov. J. Nucl. Phys.*, 42:913–917, 1985.

[87] L. Wolfenstein. Neutrino Oscillations in Matter. *Phys. Rev. D*, 17:2369–2374, 1978.

[88] Esra Bulbul, Maxim Markevitch, Adam Foster, Randall K. Smith, Michael Loewenstein, and Scott W. Randall. Detection of An Unidentified Emission Line in the Stacked X-ray spectrum of Galaxy Clusters. *Astrophys. J.*, 789:13, 2014.

[89] Alexey Boyarsky, Jeroen Franse, Dmytro Iakubovskyi, and Oleg Ruchayskiy. Checking the Dark Matter Origin of a 3.53 keV Line with the Milky Way Center. *Phys. Rev. Lett.*, 115:161301, 2015.

[90] Alexey Boyarsky, Oleg Ruchayskiy, Dmytro Iakubovskyi, and Jeroen Franse. Unidentified Line in X-Ray Spectra of the Andromeda Galaxy and Perseus Galaxy Cluster. *Phys. Rev. Lett.*, 113:251301, 2014.

[91] Vardan Khachatryan et al. Searches for invisible decays of the Higgs boson in pp collisions at $\sqrt{s}$ = 7, 8, and 13 TeV. *JHEP*, 02:135, 2017.

[92] Morad Aaboud et al. Combination of searches for invisible Higgs boson decays with the ATLAS experiment. *Phys. Rev. Lett.*, 122(23):231801, 2019.

[93] Babette Döbrich, Joerg Jaeckel, Felix Kahlhoefer, Andreas Ringwald, and Kai Schmidt-Hoberg. ALPtraum: ALP production in proton beam dump experiments. *JHEP*, 02:018, 2016.

[94] Matthew J. Dolan, Torben Ferber, Christopher Hearty, Felix Kahlhoefer, and Kai Schmidt-Hoberg. Revised constraints and Belle II sensitivity for visible and invisible axion-like particles. *JHEP*, 12:094, 2017.

[95] Brian Batell, Nicholas Lange, David McKeen, Maxim Pospelov, and Adam Ritz. Muon anomalous magnetic moment through the leptonic Higgs portal. *Phys. Rev. D*, 95(7):075003, 2017.

[96] A. Aguilar-Arevalo et al. Evidence for neutrino oscillations from the observation of $\bar{\nu}_e$ appearance in a $\bar{\nu}_\mu$ beam. *Phys. Rev. D*, 64:112007, 2001.

[97] Saeid Foroughi-Abari and Adam Ritz. LSND Constraints on the Higgs Portal. *Phys. Rev. D*, 102(3):035015, 2020.

[98] Roel Aaij et al. Search for hidden-sector bosons in $B^0 \to K^{*0}\mu^+\mu^-$ decays. *Phys. Rev. Lett.*, 115(16):161802, 2015.

[99] Brian Batell, Ayres Freitas, Ahmed Ismail, and David Mckeen. Flavor-specific scalar mediators. *Phys. Rev. D*, 98(5):055026, 2018.

[100] Michel Davier, Andreas Hoecker, Bogdan Malaescu, and Zhiqing Zhang. Reevaluation of the hadronic vacuum polarisation contributions to the Standard Model predictions of the muon $g-2$ and $\alpha(m_Z^2)$ using newest hadronic cross-section data. *Eur. Phys. J.*, C77(12):827, 2017.

[101] T. Blum, P. A. Boyle, V. Gülpers, T. Izubuchi, L. Jin, C. Jung, A. Jüttner, C. Lehner, A. Portelli, and J. T. Tsang. Calculation of the hadronic vacuum polarization contribution to the muon anomalous magnetic moment. *Phys. Rev. Lett.*, 121(2):022003, 2018.

[102] Alexander Keshavarzi, Daisuke Nomura, and Thomas Teubner. Muon $g-2$ and $\alpha(M_Z^2)$: a new data-based analysis. *Phys. Rev.*, D97(11):114025, 2018.

[103] M. Davier, A. Hoecker, B. Malaescu, and Z. Zhang. A new evaluation of the hadronic vacuum polarisation contributions to the muon anomalous magnetic moment and to $\boldsymbol{\alpha(m_Z^2)}$. *Eur. Phys. J. C*, 80(3):241, 2020. [Erratum: Eur.Phys.J.C 80, 410 (2020)].

[104] Christopher Aubin, Thomas Blum, Cheng Tu, Maarten Golterman, Chulwoo Jung, and Santiago Peris. Light quark vacuum polarization at the physical point and contribution to the muon $g-2$. *Phys. Rev. D*, 101(1):014503, 2020.

[105] T. Blum, P.A. Boyle, T. Izubuchi, L. Jin, A. Jüttner, C. Lehner, K. Maltman, M. Marinkovic, A. Portelli, and M. Spraggs. Calculation of the hadronic vacuum polarization disconnected contribution to the muon anomalous magnetic moment. *Phys. Rev. Lett.*, 116(23):232002, 2016.

[106] Christoph Lehner et al. Opportunities for Lattice QCD in Quark and Lepton Flavor Physics. *Eur. Phys. J. A*, 55(11):195, 2019.

[107] C.T.H. Davies et al. Hadronic-vacuum-polarization contribution to the muon's anomalous magnetic moment from four-flavor lattice QCD. *Phys. Rev. D*, 101(3):034512, 2020.

[108] Sz. Borsanyi et al. Leading-order hadronic vacuum polarization contribution to the muon magnetic momentfrom lattice QCD. 2 2020.

[109] Thomas Blum, Norman Christ, Masashi Hayakawa, Taku Izubuchi, Luchang Jin, Chulwoo Jung, and Christoph Lehner. Hadronic Light-by-Light Scattering Contribution to the Muon Anomalous Magnetic Moment from Lattice QCD. *Phys. Rev. Lett.*, 124(13):132002, 2020.

[110] J. Grange et al. Muon (g-2) Technical Design Report. 2015.

[111] A.T. Fienberg. The Status and Prospects of the Muon $g-2$ Experiment at Fermilab. In *54th Rencontres de Moriond on QCD and High Energy Interactions*, pages 163–166, 5 2019.

[112] Naohito Saito. A novel precision measurement of muon g-2 and EDM at J-PARC. *AIP Conf. Proc.*, 1467:45–56, 2012.

[113] Tatsumi Aoyama, Toichiro Kinoshita, and Makiko Nio. Revised and Improved Value of the QED Tenth-Order Electron Anomalous Magnetic Moment. *Phys. Rev.*, D97(3):036001, 2018.

[114] Hooman Davoudiasl and William J. Marciano. Tale of two anomalies. *Phys. Rev.*, D98(7):075011, 2018.

[115] Andreas Crivellin, Martin Hoferichter, and Philipp Schmidt-Wellenburg. Combined explanations of $(g-2)_{\mu,e}$ and implications for a large muon EDM. *Phys. Rev.*, D98(11):113002, 2018.

[116] Jia Liu, Carlos E. M. Wagner, and Xiao-Ping Wang. A light complex scalar for the electron and muon anomalous magnetic moments. *JHEP*, 03:008, 2019.

[117] Bhaskar Dutta and Yukihiro Mimura. Electron $g-2$ with flavor violation in MSSM. *Phys. Lett.*, B790:563–567, 2019.

[118] Xiao-Fang Han, Tianjun Li, Lei Wang, and Yang Zhang. Simple interpretations of lepton anomalies in the lepton-specific inert two-Higgs-doublet model. *Phys. Rev.*, D99(9):095034, 2019.

[119] A. Crivellin and M. Hoferichter. Combined explanations of $(g-2)_\mu$, $(g-2)_e$ and implications for a large muon EDM. In *33rd Rencontres de Physique de La Vallée d'Aoste (LaThuile 2019) La Thuile, Aosta, Italy, March 10-16, 2019*, 2019.

[120] Motoi Endo and Wen Yin. Explaining electron and muon $g-2$ anomaly in SUSY without lepton-flavor mixings. *JHEP*, 08:122, 2019.

[121] Mohammad Abdullah, Bhaskar Dutta, Sumit Ghosh, and Tianjun Li. $(g-2)_{\mu,e}$ and the ANITA anomalous events in a three-loop neutrino mass model. *Phys. Rev. D*, 100(11):115006, 2019.

[122] Gudrun Hiller, Clara Hormigos-Feliu, Daniel F. Litim, and Tom Steudtner. Anomalous magnetic moments from asymptotic safety. 10 2019.

[123] Naoyuki Haba, Yasuhiro Shimizu, and Toshifumi Yamada. Muon and Electron $g-2$ and the Origin of Fermion Mass Hierarchy. 2 2020.

[124] Junichiro Kawamura, Shohei Okawa, and Yuji Omura. Current status and muon $g-2$ explanation of lepton portal dark matter. *JHEP*, 08:042, 2020.

[125] Innes Bigaran and Raymond R. Volkas. Getting chirality right: top-philic scalar leptoquark solution to the $(g-2)_{e,\mu}$ puzzle. 3 2020.

[126] Sudip Jana, Vishnu P. K., and Shaikh Saad. Resolving electron and muon $g-2$ within the 2HDM. *Phys. Rev. D*, 101(11):115037, 2020.

[127] Lorenzo Calibbi, M.L. López-Ibáñez, Aurora Melis, and Oscar Vives. Muon and electron $g-2$ and lepton masses in flavor models. *JHEP*, 06:087, 2020.

[128] Chuan-Hung Chen and Takaaki Nomura. Electron and muon $g-2$, radiative neutrino mass, and $\ell' \to \ell\gamma$ in a $U(1)_{e-\mu}$ model. 3 2020.

[129] Jin-Lei Yang, Tai-Fu Feng, and Hai-Bin Zhang. Electron and muon $(g-2)$ in the B-LSSM. *J. Phys. G*, 47(5):055004, 2020.

[130] C. Hati, J. Kriewald, J. Orloff, and A.M. Teixeira. Anomalies in ^{8}Be nuclear transitions and $(g-2)_{e,\mu}$: towards a minimal combined explanation. 4 2020.

[131] Jacques P. Leveille. The Second Order Weak Correction to (G-2) of the Muon in Arbitrary Gauge Models. *Nucl. Phys.*, B137:63–76, 1978.

[132] A.M. Baldini et al. Search for the lepton flavour violating decay $\mu^+ \to \mathrm{e}^+\gamma$ with the full dataset of the MEG experiment. *Eur. Phys. J. C*, 76(8):434, 2016.

[133] Bernard Aubert et al. Searches for Lepton Flavor Violation in the Decays tau+- —> e+- gamma and tau+- —> mu+- gamma. *Phys. Rev. Lett.*, 104:021802, 2010.

[134] Morimitsu Tanimoto and Kei Yamamoto. Probing SUSY with 10 TeV stop mass in rare decays and CP violation of kaon. *PTEP*, 2016(12):123B02, 2016.

[135] Andreas Crivellin, Giancarlo D'Ambrosio, Teppei Kitahara, and Ulrich Nierste. $k \to \pi\nu\overline{\nu}$ in the mssm in light of the $\epsilon_K^{'}/\epsilon_K$ anomaly. *Phys. Rev. D*, 96:015023, Jul 2017.

[136] Marzia Bordone, Dario Buttazzo, Gino Isidori, and Joachim Monnard. Probing Lepton Flavour Universality with $K \to \pi\nu\bar{\nu}$ decays. *Eur. Phys. J. C*, 77(9):618, 2017.

[137] Motoi Endo, Toru Goto, Teppei Kitahara, Satoshi Mishima, Daiki Ueda, and Kei Yamamoto. Gluino-mediated electroweak penguin with flavor-violating trilinear couplings. *JHEP*, 04:019, 2018.

[138] Xiao-Gang He, German Valencia, and Keith Wong. Constraints on new physics from $K \to \pi\nu\bar{\nu}$. *Eur. Phys. J. C*, 78(6):472, 2018.

[139] Chuan-Hung Chen and Takaaki Nomura. $Re(\epsilon_K^{'}/\epsilon_K)$ and $K \to \pi\nu\bar{\nu}$ in a two-Higgs doublet model. *JHEP*, 08:145, 2018.

[140] S. Fajfer, N. Košnik, and L. Vale Silva. Footprints of leptoquarks: from $R_{K^{(*)}}$ to $K \to \pi\nu\bar{\nu}$. *Eur. Phys. J. C*, 78(4):275, 2018.

[141] Laurence S. Littenberg. Cp-violating decay $K_L^0 \to \pi^0\nu\nu^{-}$. *Phys. Rev. D*, 39:3322–3324, Jun 1989.

[142] Vincenzo Cirigliano, Gerhard Ecker, Helmut Neufeld, Antonio Pich, and Jorge Portoles. Kaon Decays in the Standard Model. *Rev. Mod. Phys.*, 84:399, 2012.

[143] J. Comfort et al. *Proposal for $K_L \to \pi^0\bar{\nu}\nu$ experiment at J-Parc*, 2019.

[144] Taku Yamanaka. The J-PARC KOTO experiment. *PTEP*, 2012:02B006, 2012.

[145] Shoji Nagamiya. Introduction to J-PARC. *PTEP*, 2012:02B001, 2012.

[146] Eduardo Cortina Gil et al. The Beam and detector of the NA62 experiment at CERN. *JINST*, 12(05):P05025, 2017.

[147] J.K. Ahn et al. Search for the $K_L \to \pi^0\nu\overline{\nu}$ and $K_L \to \pi^0 X^0$ decays at the J-PARC KOTO experiment. *Phys. Rev. Lett.*, 122(2):021802, 2019.

[148] G. Ruggiero. *New Result on $K^+ \to \pi^+ \bar{\nu}\nu$ from the NA62 Experiment*, September 2019. KAON2019, Perugia, Italy.

[149] Yuval Grossman and Yosef Nir. K(L) —> pi0 neutrino anti-neutrino beyond the standard model. *Phys. Lett. B*, 398:163–168, 1997.

[150] A.V. Artamonov et al. Study of the decay $K^+ \to \pi^+ \nu\bar{\nu}$ in the momentum region $140 < P_\pi < 199$ MeV/c. *Phys. Rev. D*, 79:092004, 2009.

[151] Eduardo Cortina Gil et al. First search for $K^+ \to \pi^+ \nu\bar{\nu}$ using the decay-in-flight technique. *Phys. Lett. B*, 791:156–166, 2019.

[152] Kaori Fuyuto, Wei-Shu Hou, and Masaya Kohda. Loophole in $K \to \pi\nu\bar{\nu}$ Search and New Weak Leptonic Forces. *Phys. Rev. Lett.*, 114:171802, 2015.

[153] Bruce McWilliams and Oruganti U. Shanker. The General $K0$ to Anti-$k0$ and $D0$ to Anti-$d0$ Transition Amplitude in the MIT Bag Model. *Phys. Rev. D*, 22:2853, 1980.

[154] Enrico Bertuzzo, Sudip Jana, Pedro A.N. Machado, and Renata Zukanovich Funchal. Neutrino Masses and Mixings Dynamically Generated by a Light Dark Sector. *Phys. Lett. B*, 791:210–214, 2019.

[155] Enrico Bertuzzo, Sudip Jana, Pedro A. N. Machado, and Renata Zukanovich Funchal. Dark Neutrino Portal to Explain MiniBooNE excess. *Phys. Rev. Lett.*, 121(24):241801, 2018.

[156] Peter Ballett, Silvia Pascoli, and Mark Ross-Lonergan. U(1)' mediated decays of heavy sterile neutrinos in MiniBooNE. *Phys. Rev. D*, 99:071701, 2019.

[157] Peter Ballett, Matheus Hostert, and Silvia Pascoli. Neutrino Masses from a Dark Neutrino Sector below the Electroweak Scale. *Phys. Rev. D*, 99(9):091701, 2019.

[158] Peter Ballett, Matheus Hostert, and Silvia Pascoli. Dark Neutrinos and a Three Portal Connection to the Standard Model. *Phys. Rev. D*, 101(11):115025, 2020.

[159] Waleed Abdallah, Raj Gandhi, and Samiran Roy. Understanding the MiniBooNE and the muon $g-2$ anomalies with a light Z' and a second Higgs doublet. 6 2020.

[160] Alakabha Datta, Saeed Kamali, and Danny Marfatia. Dark sector origin of the KOTO and MiniBooNE anomalies. *Phys. Lett. B*, 807:135579, 2020.

[161] M. Martini, M. Ericson, and G. Chanfray. Neutrino energy reconstruction problems and neutrino oscillations. *Phys. Rev. D*, 85:093012, 2012.

[162] Carlos A. Argüelles, Matheus Hostert, and Yu-Dai Tsai. Testing New Physics Explanations of the MiniBooNE Anomaly at Neutrino Scattering Experiments. *Phys. Rev. Lett.*, 123(26):261801, 2019.

[163] A.A. Aguilar-Arevalo et al. The MiniBooNE Detector. *Nucl. Instrum. Meth. A*, 599:28–46, 2009.

[164] Richard H. Helm. Inelastic and Elastic Scattering of 187-Mev Electrons from Selected Even-Even Nuclei. *Phys. Rev.*, 104:1466–1475, 1956.

[165] J. Engel. Nuclear form-factors for the scattering of weakly interacting massive particles. *Phys. Lett. B*, 264:114–119, 1991.

[166] Toby Falk, Andrew Ferstl, and Keith A. Olive. Variations of the neutralino elastic cross-section with CP violating phases. *Astropart. Phys.*, 13:301–316, 2000.

[167] J.M. Alarcon, J. Martin Camalich, and J.A. Oller. The chiral representation of the πN scattering amplitude and the pion-nucleon sigma term. *Phys. Rev. D*, 85:051503, 2012.

[168] J.M. Alarcon, L.S. Geng, J. Martin Camalich, and J.A. Oller. The strangeness content of the nucleon from effective field theory and phenomenology. *Phys. Lett. B*, 730:342–346, 2014.

[169] Andreas Crivellin, Martin Hoferichter, and Massimiliano Procura. Accurate evaluation of hadronic uncertainties in spin-independent WIMP-nucleon scattering: Disentangling two- and three-flavor effects. *Phys. Rev. D*, 89:054021, 2014.

[170] Martin Hoferichter, J. Ruiz de Elvira, Bastian Kubis, and Ulf-G. Meißner. High-Precision Determination of the Pion-Nucleon σ Term from Roy-Steiner Equations. *Phys. Rev. Lett.*, 115:092301, 2015.

[171] Parikshit Junnarkar and Andre Walker-Loud. Scalar strange content of the nucleon from lattice QCD. *Phys. Rev. D*, 87:114510, 2013.

[172] T. Layda. New results from the CHARM-II experiment. In *26th Rencontres de Moriond: Electroweak Interactions and Unified Theories*, pages 79–86, 1991.

[173] K. De Winter et al. A Detector for the Study of Neutrino - Electron Scattering. *Nucl. Instrum. Meth. A*, 278:670, 1989.

[174] D. Geiregat et al. Calibration and performance of the CHARM-II detector. *Nucl. Instrum. Meth. A*, 325:92–108, 1993.

[175] P. Vilain et al. Precision measurement of electroweak parameters from the scattering of muon-neutrinos on electrons. *Phys. Lett. B*, 335:246–252, 1994.

[176] Vedran Brdar, Oliver Fischer, and Alexei Yu. Smirnov. Model Independent Bounds on the Non-Oscillatory Explanations of the MiniBooNE Excess. 7 2020.

[177] K. Abe et al. The T2K Experiment. *Nucl. Instrum. Meth. A*, 659:106–135, 2011.

[178] Yury Kudenko. The Near neutrino detector for the T2K experiment. *Nucl. Instrum. Meth. A*, 598:289–295, 2009.

[179] S. Assylbekov et al. The T2K ND280 Off-Axis Pi-Zero Detector. *Nucl. Instrum. Meth. A*, 686:48–63, 2012.

[180] P.A. Amaudruz et al. The T2K Fine-Grained Detectors. *Nucl. Instrum. Meth. A*, 696:1–31, 2012.

[181] K. Abe et al. T2K neutrino flux prediction. *Phys. Rev. D*, 87(1):012001, 2013. [Addendum: Phys.Rev.D 87, 019902 (2013)].

[182] K. Abe et al. Search for heavy neutrinos with the T2K near detector ND280. *Phys. Rev. D*, 100(5):052006, 2019.

[183] J. Wolcott et al. Evidence for Neutral-Current Diffractive π^0 Production from Hydrogen in Neutrino Interactions on Hydrocarbon. *Phys. Rev. Lett.*, 117(11):111801, 2016.

[184] J. Park et al. Measurement of Neutrino Flux from Neutrino-Electron Elastic Scattering. *Phys. Rev. D*, 93(11):112007, 2016.

[185] J. Wolcott et al. Measurement of electron neutrino quasielastic and quasielasticlike scattering on hydrocarbon at $\langle E_\nu \rangle$ = 3.6 GeV. *Phys. Rev. Lett.*, 116(8):081802, 2016.

[186] E. Valencia et al. Constraint of the MINERνA medium energy neutrino flux using neutrino-electron elastic scattering. *Phys. Rev. D*, 100(9):092001, 2019.

[187] Yonit Hochberg, Eric Kuflik, Hitoshi Murayama, Tomer Volansky, and Jay G. Wacker. Model for Thermal Relic Dark Matter of Strongly Interacting Massive Particles. *Phys. Rev. Lett.*, 115(2):021301, 2015.

[188] Eric Kuflik, Maxim Perelstein, Nicolas Rey-Le Lorier, and Yu-Dai Tsai. Elastically Decoupling Dark Matter. *Phys. Rev. Lett.*, 116(22):221302, 2016.

[189] B. Abi et al. Measurement of the Positive Muon Anomalous Magnetic Moment to 0.46 ppm. *Phys. Rev. Lett.*, 126(14):141801, 2021.

[190] Roel Aaij et al. Test of lepton universality in beauty-quark decays. 3 2021.

[191] Jogesh C. Pati and Abdus Salam. Lepton Number as the Fourth Color. *Phys. Rev.*, D10:275–289, 1974. [Erratum: Phys. Rev.D11,703(1975)].

[192] R. N. Mohapatra and Jogesh C. Pati. A Natural Left-Right Symmetry. *Phys. Rev.*, D11:2558, 1975.

[193] G. Senjanovic and Rabindra N. Mohapatra. Exact Left-Right Symmetry and Spontaneous Violation of Parity. *Phys. Rev.*, D12:1502, 1975.

[194] Ross Diener, Stephen Godfrey, and Ismail Turan. Constraining Extra Neutral Gauge Bosons with Atomic Parity Violation Measurements. *Phys. Rev. D*, 86:115017, 2012.

[195] L.D. Landau. On the angular momentum of a system of two photons. *Dokl. Akad. Nauk SSSR*, 60(2):207–209, 1948.

[196] Chen-Ning Yang. Selection Rules for the Dematerialization of a Particle Into Two Photons. *Phys. Rev.*, 77:242–245, 1950.

[197] Robert Foot. New Physics From Electric Charge Quantization? *Mod. Phys. Lett.*, A6:527–530, 1991.

[198] X. G. He, Girish C. Joshi, H. Lew, and R. R. Volkas. NEW Z-prime PHENOMENOLOGY. *Phys. Rev.*, D43:22–24, 1991.

[199] Xiao-Gang He, Girish C. Joshi, H. Lew, and R. R. Volkas. Simplest Z-prime model. *Phys. Rev.*, D44:2118–2132, 1991.

[200] Debasish Borah, Lopamudra Mukherjee, and Soumitra Nandi. Low Scale $U(1)_X$ Gauge Symmetry as an Origin of Dark Matter, Neutrino Mass and Flavour Anomalies. 7 2020.

[201] Davi B. Costa. Simple anomaly-free $U(1)$ extensions of the Standard Model. 7 2020.

[202] Z. G. Berezhiani. The Weak Mixing Angles in Gauge Models with Horizontal Symmetry: A New Approach to Quark and Lepton Masses. *Phys. Lett. B*, 129:99–102, 1983.

[203] Darwin Chang and Rabindra N. Mohapatra. Small and Calculable Dirac Neutrino Mass. *Phys. Rev. Lett.*, 58:1600, 1987.

[204] Aharon Davidson and Kameshwar C. Wali. Universal Seesaw Mechanism? *Phys. Rev. Lett.*, 59:393, 1987.

[205] A. De Pace, H. Muther, and A. Faessler. Attraction in the Skyrme Model NN Central Interaction. *Phys. Lett. B*, 188:307–310, 1987.

[206] S. Rajpoot. See-saw masses for quarks and leptons in an ambidextrous electroweak interaction model. *Mod. Phys. Lett. A*, 2(5):307–315, 1987. [Erratum: Mod.Phys.Lett.A 2, 541 (1987)].

[207] K. S. Babu and Rabindra N. Mohapatra. CP Violation in Seesaw Models of Quark Masses. *Phys. Rev. Lett.*, 62:1079, 1989.

[208] K. S. Babu and Rabindra N. Mohapatra. A Solution to the Strong CP Problem Without an Axion. *Phys. Rev. D*, 41:1286, 1990.

[209] K. S. Babu, Bhaskar Dutta, and Rabindra N. Mohapatra. A theory of R(D*, D) anomaly with right-handed currents. *JHEP*, 01:168, 2019.

[210] Tatsumi Aoyama, Masashi Hayakawa, Toichiro Kinoshita, and Makiko Nio. Complete Tenth-Order QED Contribution to the Muon $g-2$. *Phys. Rev. Lett.*, 109:111808, 2012.

[211] Tatsumi Aoyama, Toichiro Kinoshita, and Makiko Nio. Theory of the Anomalous Magnetic Moment of the Electron. *Atoms*, 7(1):28, 2019.

[212] Andrzej Czarnecki, William J. Marciano, and Arkady Vainshtein. Refinements in electroweak contributions to the muon anomalous magnetic moment. *Phys. Rev.*, D67:073006, 2003. [Erratum: Phys. Rev. **D73**, 119901 (2006)].

[213] C. Gnendiger, D. Stöckinger, and H. Stöckinger-Kim. The electroweak contributions to $(g-2)_\mu$ after the Higgs boson mass measurement. *Phys. Rev.*, D88:053005, 2013.

[214] Gilberto Colangelo, Martin Hoferichter, and Peter Stoffer. Two-pion contribution to hadronic vacuum polarization. *JHEP*, 02:006, 2019.

[215] Martin Hoferichter, Bai-Long Hoid, and Bastian Kubis. Three-pion contribution to hadronic vacuum polarization. *JHEP*, 08:137, 2019.

[216] Alexander Keshavarzi, Daisuke Nomura, and Thomas Teubner. The $g-2$ of charged leptons, $\alpha(M_Z^2)$ and the hyperfine splitting of muonium. *Phys. Rev.*, D101:014029, 2020.

[217] Alexander Kurz, Tao Liu, Peter Marquard, and Matthias Steinhauser. Hadronic contribution to the muon anomalous magnetic moment to next-to-next-to-leading order. *Phys. Lett.*, B734:144–147, 2014.

[218] Kirill Melnikov and Arkady Vainshtein. Hadronic light-by-light scattering contribution to the muon anomalous magnetic moment revisited. *Phys. Rev.*, D70:113006, 2004.

[219] Pere Masjuan and Pablo Sánchez-Puertas. Pseudoscalar-pole contribution to the $(g_\mu - 2)$: a rational approach. *Phys. Rev.*, D95(5):054026, 2017.

[220] Gilberto Colangelo, Martin Hoferichter, Massimiliano Procura, and Peter Stoffer. Dispersion relation for hadronic light-by-light scattering: two-pion contributions. *JHEP*, 04:161, 2017.

[221] Martin Hoferichter, Bai-Long Hoid, Bastian Kubis, Stefan Leupold, and Sebastian P. Schneider. Dispersion relation for hadronic light-by-light scattering: pion pole. *JHEP*, 10:141, 2018.

[222] Antoine Gérardin, Harvey B. Meyer, and Andreas Nyffeler. Lattice calculation of the pion transition form factor with $N_f = 2 + 1$ Wilson quarks. *Phys. Rev.*, D100(3):034520, 2019.

[223] Johan Bijnens, Nils Hermansson-Truedsson, and Antonio Rodríguez-Sánchez. Short-distance constraints for the HLbL contribution to the muon anomalous magnetic moment. *Phys. Lett.*, B798:134994, 2019.

[224] Gilberto Colangelo, Franziska Hagelstein, Martin Hoferichter, Laetitia Laub, and Peter Stoffer. Longitudinal short-distance constraints for the hadronic light-by-light contribution to $(g-2)_\mu$ with large-N_c Regge models. *JHEP*, 03:101, 2020.

[225] Gilberto Colangelo, Martin Hoferichter, Andreas Nyffeler, Massimo Passera, and Peter Stoffer. Remarks on higher-order hadronic corrections to the muon $g - 2$. *Phys. Lett.*, B735:90–91, 2014.

[226] Francisco Campanario, Henryk Czyż, Janusz Gluza, Tomasz Jeliński, Germán Rodrigo, Szymon Tracz, and Dmitry Zhuridov. Standard model radiative corrections in the pion form factor measurements do not explain the a_μ anomaly. *Phys. Rev. D*, 100(7):076004, 2019.

[227] Herbert K. Dreiner, Jean-François Fortin, Jordi Isern, and Lorenzo Ubaldi. White Dwarfs constrain Dark Forces. *Phys. Rev. D*, 88:043517, 2013.

[228] Ann E. Nelson and Jonathan Walsh. Short Baseline Neutrino Oscillations and a New Light Gauge Boson. *Phys. Rev. D*, 77:033001, 2008.

[229] Baruch Feldman and Ann E. Nelson. New regions for a chameleon to hide. *JHEP*, 08:002, 2006.

[230] A.E. Nelson and J. Walsh. Chameleon vector bosons. *Phys. Rev. D*, 77:095006, 2008.

[231] Jonathan L. Feng, Iftah Galon, Felix Kling, and Sebastian Trojanowski. ForwArd Search ExpeRiment at the LHC. *Phys. Rev. D*, 97(3):035001, 2018.

[232] Akitaka Ariga et al. Letter of Intent for FASER: ForwArd Search ExpeRiment at the LHC. 11 2018.

[233] Akitaka Ariga et al. Technical Proposal for FASER: ForwArd Search ExpeRiment at the LHC. 12 2018.

[234] Akitaka Ariga et al. FASER's physics reach for long-lived particles. *Phys. Rev. D*, 99(9):095011, 2019.

[235] M. Anelli et al. A facility to Search for Hidden Particles (SHiP) at the CERN SPS. 4 2015.

[236] Sergey Alekhin et al. A facility to Search for Hidden Particles at the CERN SPS: the SHiP physics case. *Rept. Prog. Phys.*, 79(12):124201, 2016.

[237] C.A. Aidala et al. The SeaQuest Spectrometer at Fermilab. *Nucl. Instrum. Meth. A*, 930:49–63, 2019.

[238] Bhaskar Dutta, Sumit Ghosh, and Jason Kumar. A sub-GeV dark matter model. *Phys. Rev. D*, 100:075028, 2019.

[239] Torsten Åkesson et al. Light Dark Matter eXperiment (LDMX). 8 2018.

[240] A. A. Aguilar-Arevalo et al. *Fundamental Neutrino Physics at the Lujan Center*, March 2018.

[241] E. Dunton. *Searching for Sterile Neutrinos with Coherent Captain Mills*, November 2019. gnificent CEvNS 201.

[242] M. Harada et al. Proposal: A Search for Sterile Neutrino at J-PARC Materials and Life Science Experimental Facility. 10 2013.

[243] S. Ajimura et al. On-site background measurements for the J-PARC E56 experiment: A search for the sterile neutrino at J-PARC MLF. *PTEP*, 2015(6):063C01, 2015.

[244] M. Harada et al. Status Report for the 20th J-PARC PAC : A Search for Sterile Neutrino at J-PARC MLF (J-PARC E56, JSNS2). 7 2015.

[245] S. Ajimura et al. Technical Design Report (TDR): Searching for a Sterile Neutrino at J-PARC MLF (E56, JSNS2). 5 2017.

[246] Carsten Rott. Status of JSNS^2 - J-PARC Sterile Neutrino Search at J-PARC Spallation Neutron Source. *J. Phys. Conf. Ser.*, 1468(1):012176, 2020.

[247] Daniel Z. Freedman. Coherent Neutrino Nucleus Scattering as a Probe of the Weak Neutral Current. *Phys. Rev. D*, 9:1389–1392, 1974.

[248] V.B. Kopeliovich and L.L. Frankfurt. Isotopic and chiral structure of neutral current. *JETP Lett.*, 19:145–147, 1974.

[249] Bhaskar Dutta, Doojin Kim, Shu Liao, Jong-Chul Park, Seodong Shin, Louis E. Strigari, and Adrian Thompson. Searching for Dark Matter Signals in Timing Spectra at Neutrino Experiments. 6 2020.

[250] Bhaskar Dutta, Doojin Kim, Shu Liao, Jong-Chul Park, Seodong Shin, and Louis E. Strigari. Dark matter signals from timing spectra at neutrino experiments. *Phys. Rev. Lett.*, 124(12):121802, 2020.

[251] Bhaskar Dutta, Rafael F. Lang, Shu Liao, Samiran Sinha, Louis Strigari, and Adrian Thompson. A global analysis strategy to resolve neutrino NSI degeneracies with scattering and oscillation data. 2 2020.

[252] James Strait. DUNE Physics. In *17th International Workshop on Neutrino Factories and Future Neutrino Facilities*, 8 2015.

[253] Alec Habig. An Experimental Program in Neutrinos, Nucleon Decay and Astroparticle Physics Enabled by the Fermilab Long-Baseline Neutrino Facility. *PoS*, EPS-HEP2015:041, 2015.

[254] Babak Abi et al. Deep Underground Neutrino Experiment (DUNE), Far Detector Technical Design Report, Volume I Introduction to DUNE. 2 2020.

[255] Babak Abi et al. Deep Underground Neutrino Experiment (DUNE), Far Detector Technical Design Report, Volume II DUNE Physics. 2 2020.

[256] Babak Abi et al. Deep Underground Neutrino Experiment (DUNE), Far Detector Technical Design Report, Volume III DUNE Far Detector Technical Coordination. 2 2020.

[257] Babak Abi et al. Deep Underground Neutrino Experiment (DUNE), Far Detector Technical Design Report, Volume IV Far Detector Single-phase Technology. 2 2020.

[258] Jost Migenda. The Hyper-Kamiokande Experiment: Overview & Status. In *Prospects in Neutrino Physics*, 4 2017.

[259] Masashi Yokoyama. The Hyper-Kamiokande Experiment. In *Prospects in Neutrino Physics*, 4 2017.

[260] Miao Jiang. Sensitivity of new physics by joint analysis of neutrino oscillation on Hyper-Kamiokande. *J. Phys. Conf. Ser.*, 888(1):012111, 2017.

[261] Christophe Bronner. Physics potential of Hyper-Kamiokande for neutrino oscillation measurements. *PoS*, NuFact2017:053, 2018.

[262] Takatomi Yano. Astroparticle Physics in Hyper-Kamiokande. *J. Phys. Conf. Ser.*, 1468(1):012146, 2020.

[263] Yury Kudenko. Hyper-Kamiokande. In *International Conference on Instrumentation for Colliding Beam Physics*, 5 2020.

[264] A. H. Abdelhameed et al. First results from the CRESST-III low-mass dark matter program. *Phys. Rev. D*, 100(10):102002, 2019.

[265] Rouven Essig, Aaron Manalaysay, Jeremy Mardon, Peter Sorensen, and Tomer Volansky. First Direct Detection Limits on sub-GeV Dark Matter from XENON10. *Phys. Rev. Lett.*, 109:021301, 2012.

[266] R. Agnese et al. First Dark Matter Constraints from a SuperCDMS Single-Charge Sensitive Detector. *Phys. Rev. Lett.*, 121(5):051301, 2018. [Erratum: Phys.Rev.Lett. 122, 069901 (2019)].

[267] Orr Abramoff et al. SENSEI: Direct-Detection Constraints on Sub-GeV Dark Matter from a Shallow Underground Run Using a Prototype Skipper-CCD. *Phys. Rev. Lett.*, 122(16):161801, 2019.

[268] Spencer Chang, Jia Liu, Aaron Pierce, Neal Weiner, and Itay Yavin. CoGeNT Interpretations. *JCAP*, 08:018, 2010.

[269] Jonathan L. Feng, Jason Kumar, Danny Marfatia, and David Sanford. Isospin-Violating Dark Matter. *Phys. Lett. B*, 703:124–127, 2011.

[270] Jonathan L. Feng, Jason Kumar, and David Sanford. Xenophobic Dark Matter. *Phys. Rev. D*, 88(1):015021, 2013.

[271] J. Gasser, H. Leutwyler, and M. E. Sainio. Sigma term update. *Phys. Lett. B*, 253:252–259, 1991.

[272] Yohei Ema, Filippo Sala, and Ryosuke Sato. Light Dark Matter at Neutrino Experiments. *Phys. Rev. Lett.*, 122(18):181802, 2019.

[273] Christopher Cappiello and John F. Beacom. Strong New Limits on Light Dark Matter from Neutrino Experiments. *Phys. Rev. D*, 100(10):103011, 2019.

[274] John D. Barrow. MASSIVE PARTICLES AS A PROBE OF THE EARLY UNIVERSE. *Nucl. Phys. B*, 208:501–508, 1982.

[275] Lawrence J. Hall, Karsten Jedamzik, John March-Russell, and Stephen M. West. Freeze-In Production of FIMP Dark Matter. *JHEP*, 03:080, 2010.

[276] Riccardo Catena, N. Fornengo, A. Masiero, Massimo Pietroni, and Francesca Rosati. Dark matter relic abundance and scalar - tensor dark energy. *Phys. Rev. D*, 70:063519, 2004.

[277] R. Aaij et al. Test of lepton universality with $B^0 \to K^{*0}\ell^+\ell^-$ decays. *JHEP*, 08:055, 2017.

[278] A. Abdesselam et al. Test of lepton flavor universality in $B \to K^*\ell^+\ell^-$ decays at Belle. 4 2019.

[279] Li-Sheng Geng, Benjamín Grinstein, Sebastian Jäger, Shuang-Yi Li, Jorge Martin Camalich, and Rui-Xiang Shi. Implications of new evidence for lepton-universality violation in $b \to s\ell^+\ell^-$ decays. 3 2021.

[280] Gudrun Hiller and Frank Kruger. More model-independent analysis of $b \to s$ processes. *Phys. Rev.*, D69:074020, 2004.

[281] Chris Bouchard, G. Peter Lepage, Christopher Monahan, Heechang Na, and Junko Shigemitsu. Standard Model Predictions for $B \to K\ell^+\ell^-$ with Form Factors from Lattice QCD. *Phys. Rev. Lett.*, 111(16):162002, 2013. [Erratum: Phys. Rev. Lett.112,no.14,149902(2014)].

[282] Roel Aaij et al. Test of lepton universality using $B^+ \to K^+\ell^+\ell^-$ decays. *Phys. Rev. Lett.*, 113:151601, 2014.

[283] Roel Aaij et al. Search for lepton-universality violation in $B^+ \to K^+\ell^+\ell^-$ decays. *Phys. Rev. Lett.*, 122(19):191801, 2019.

[284] Alakabha Datta, Jacky Kumar, Jiajun Liao, and Danny Marfatia. New light mediators for the R_K and R_{K^*} puzzles. *Phys. Rev. D*, 97(11):115038, 2018.

[285] Wolfgang Altmannshofer, Michael J. Baker, Stefania Gori, Roni Harnik, Maxim Pospelov, Emmanuel Stamou, and Andrea Thamm. Light resonances and the low-q^2 bin of R_{K^*}. *JHEP*, 03:188, 2018.

[286] M. Santimaria. New results on theoretically clean observables in rare B-meson decays from LHCb, 3 2021.

[287] Morad Aaboud et al. Study of the rare decays of B_s^0 and B^0 mesons into muon pairs using data collected during 2015 and 2016 with the ATLAS detector. *JHEP*, 04:098, 2019.

[288] Albert M Sirunyan et al. Measurement of properties of $\mathrm{B}_\mathrm{s}^0 \to \mu^+\mu^-$ decays and search for $\mathrm{B}^0 \to \mu^+\mu^-$ with the CMS experiment. *JHEP*, 04:188, 2020.

[289] Wolfgang Altmannshofer and Peter Stangl. New Physics in Rare B Decays after Moriond 2021. 3 2021.

[290] S. R. Mishra et al. Neutrino tridents and W Z interference. *Phys. Rev. Lett.*, 66:3117–3120, 1991.

[291] O. Lutz et al. Search for $B \to h^{(*)}\nu\bar{\nu}$ with the full Belle $\Upsilon(4S)$ data sample. *Phys. Rev. D*, 87(11):111103, 2013.

[292] David M. Straub. flavio: a Python package for flavour and precision phenomenology in the Standard Model and beyond. 10 2018.

[293] R. Aaij et al. Differential branching fractions and isospin asymmetries of $B \to K^{(*)}\mu^+\mu^-$ decays. *JHEP*, 06:133, 2014.

[294] Roel Aaij et al. Angular analysis and differential branching fraction of the decay $B_s^0 \to \phi\mu^+\mu^-$. *JHEP*, 09:179, 2015.

[295] Roel Aaij et al. Differential branching fraction and angular analysis of $\Lambda_b^0 \to \Lambda\mu^+\mu^-$ decays. *JHEP*, 06:115, 2015. [Erratum: JHEP 09, 145 (2018)].

[296] Steven Weinberg. Baryon and Lepton Nonconserving Processes. *Phys. Rev. Lett.*, 43:1566–1570, 1979.

[297] Ivan Esteban, M. C. Gonzalez-Garcia, Michele Maltoni, Ivan Martinez-Soler, and Thomas Schwetz. Updated fit to three neutrino mixing: exploring the accelerator-reactor complementarity. *JHEP*, 01:087, 2017.

[298] Albert M Sirunyan et al. Search for narrow and broad dijet resonances in proton-proton collisions at $\sqrt{s} = 13$ TeV and constraints on dark matter mediators and other new particles. *JHEP*, 08:130, 2018.

[299] Morad Aaboud et al. Search for new phenomena in dijet events using 37 fb^{-1} of pp collision data collected at $\sqrt{s}$ =13 TeV with the ATLAS detector. *Phys. Rev.*, D96(5):052004, 2017.

[300] Bhaskar Dutta, Sumit Ghosh, Ilia Gogoladze, and Tianjun Li. Three-loop neutrino masses via new massive gauge bosons from E_6 GUT. *Phys. Rev. D*, 98(5):055028, 2018.

[301] Katherine Freese, Joshua A. Frieman, and Andrew Gould. Signal Modulation in Cold Dark Matter Detection. *Phys. Rev. D*, 37:3388–3405, 1988.

APPENDIX A

HIGGS BASIS TRANSFORMATION

In this appendix, we briefly discuss the basis transformation strategy we have used in the Sec. 2.1 of Chap. 2. To begin with, we consider two complex scalar doublets $H_{1,2}$ and once singlet scalar H_S. The charges under the SM gauge symmetry are,

$$H_1 \sim (2, 1/2), \quad H_2 \sim (2, 1/2), \quad H_S \sim (1, 0)\ . \tag{A.1}$$

The most general charge conserving vev's can be defined as,

$$\langle H_1 \rangle = \begin{pmatrix} 0 \\ \frac{v_1}{\sqrt{2}} \end{pmatrix},\ \langle H_2 \rangle = \begin{pmatrix} 0 \\ \frac{v_2}{\sqrt{2}} \end{pmatrix},\ \langle H_S \rangle = \frac{v_3}{\sqrt{2}}\ . \tag{A.2}$$

The neutral components of the Higgs fields can be redefined by rotating via a Unitary matrix U in such a way that only one of the scalar doublet will obtain a non-zero vev. The neutral components of the new Higgs fields can be defined as,

$$\phi_a^0 = \sum_b U_{ab} H_b^0\ , \tag{A.3}$$

where $a, b = 1, 2,$ and S. And the Unitary matrix U is defined as,

$$U = \begin{pmatrix} \frac{v_1}{v} & \frac{v_2}{v} & \frac{v_3}{v} \\ -\frac{v_2}{v} & \frac{v_1}{v} & 0 \\ -\frac{v_3}{v} & 0 & \frac{v_1}{v} \end{pmatrix}\ . \tag{A.4}$$

Using Eq. A.4 in Eq. A.3, we get the vev's of the new Higgs fields as,

$$\langle \phi_1^0 \rangle = \begin{pmatrix} 0 \\ \\ \frac{v}{\sqrt{2}} \end{pmatrix}, \ \langle \phi_2^0 \rangle = 0, \ \langle \phi_S^0 \rangle = 0 \ , \tag{A.5}$$

where, we have defined $v = (v_1^2 + v_2^2 + v_3^2)^{1/2}$. Therefore, in this Higgs basis, only one doublet will controll the spontaneous symmetry breaking and the mass generation of various particles in the model.

APPENDIX B

CALCULATION OF LFV PROCESSES

In this appendix, we provide the most general expression for the branching fraction of the lepton flavor violating processes mediated by scalar mediator. The expression for the process $e_i \to e_j\gamma$ shown in Fig. 2.1 mediated by light scalar is given by,

$$\begin{aligned} \text{Br}(e_i \to e_j\gamma) &= \frac{\Gamma(e_i \to e_j\gamma)}{\Gamma(e_i \to e_j\bar{\nu}_j\nu_i)} \\ &= \frac{3\alpha}{8\pi G_F^2 m_{e_i}^2}\left(1-\frac{m_{e_j}^2}{m_{e_i}^2}\right)\left[(y_{eh_1})_{ik}(y_{eh_1})_{kj}\right]^2 \frac{I_1(m_{e_i},m_{e_j},m_{e_k},m_{h_1})}{I_2(m_{e_j}^2/m_{e_i}^2)}\,, \end{aligned} \tag{B.1}$$

here, the lepton e_k runs inside the loop. The function $I_1(m_{e_i}, m_{e_j}, m_{e_k}, m_{h_1})$ comes from the partial decay width $\Gamma(e_i \to e_j\gamma)$ and the function $I_2(m_{e_j}^2/m_{e_i}^2)$ comes from $\Gamma(e_i \to e_j\bar{\nu}_j\nu_i)$.

The functions I_1 and I_2 can be defined as,

$$I_1(m_{e_i},m_{e_j},m_{e_k},m_{h_1}) = \int_0^1 dz \int_0^{1-z} dy \frac{yz(m_{e_j}-m_{e_i}) - (z-1)(zm_{e_i}+m_{e_k})}{z(y+z-1)m_{e_i}^2 - yzm_{e_j}^2 + (1-z)m_{e_k}^2 + zm_{h_1}^2}\,, \tag{B.2}$$

$$I_2\left(\frac{m_{e_j}^2}{m_{e_i}^2}\right) = 1 - 8\frac{m_{e_j}^2}{m_{e_i}^2} + 8\frac{m_{e_j}^6}{m_{e_i}^6} - \frac{m_{e_j}^8}{m_{e_i}^8} + 12\frac{m_{e_j}^4}{m_{e_i}^4}\ln\left(\frac{m_{e_i}^2}{m_{e_j}^2}\right)\,. \tag{B.3}$$

respectively.

APPENDIX C

NUCLEAR FORM FACTOR AND DARK MATTER VELOCITY DISTRIBUTION

We provide the nuclear form factor and the dark matter velocity distribution used for the direct detection rate calculations, in this appendix. Following the references [164, 165], we write the nuclear form factor as,

$$F(E_R) = \frac{3j_1(qR_1)}{qR_1} \exp\left(-q^2 s^2/2\right), \tag{C.1}$$

where the momentum transferred is q is defined as $q = \sqrt{2m_A E_R}$, E_R is the nuclear recoil energy; j_1 is the spherical Bessel function of index 1; $s \simeq 1$ fm is the measure of nuclear skin thickness, and; $R_1 \simeq \sqrt{r^2 - 5s^2}$ with $r = 1.2A^{1/3}$ fm and A is the mass number of the nucleus of the target material.

To get the dark matter velocity distribution in the Earth frame, we start with the Maxwellian dark matter velocity distribution in the galactic rest frame [301],

$$f(v')dv' = \left[\frac{3}{2\pi v_0^2}\right]^{3/2} \exp\left(-\frac{3v'^2}{2v_0^2}\right) 4\pi v'^2 dv', \tag{C.2}$$

where $v_0 = 220$km/sec. One crucial aspect of the dark matter velocity distribution is that it is truncated at the local galactic escape velocity.

We make the following Galilean transformation to get the velocity distribution with respect to the Earth frame,

$$\vec{v'} = \vec{v} + \vec{v}_E, \tag{C.3}$$

where $\vec{v}$ is the dark matter velocity with respect to the Earth frame and $\vec{v_E}$ is the velocity of Earth with respect to the galactic rest frame, equal to 232 km/sec. Therefore in the Earth frame, the dark

matter velocity distribution is given by,

$$f(v)dv = \left[\frac{3}{2\pi v_0^2}\right]^{3/2} \exp\left[-\frac{3}{2v_0^2}(v^2 + v_E^2)\right] \frac{v_0^2}{3vv_E} \sinh\left(\frac{3vv_E}{v_0^2}\right) 4\pi v^2 dv. \tag{C.4}$$